UNIVERSITY OF CALIFORNIA
RIVERSIDE

MoS_2 Based Heterostructures for Enhanced Chemical and Biological Sensing

A Dissertation submitted in partial satisfaction
of the requirements for the degree of

Doctor of Philosophy

in

Chemical and Environmental Engineering

by

Tung Thanh Pham

September 2019

Dissertation Committee:
Dr. Ashok Mulchandani, Chairperson
Dr. Ruoxue Yan
Dr. Kandis Leslie Abdul-Aziz

The Dissertation of Tung Thanh Pham is approved:

Committee Chairperson

University of California, Riverside

ACKNOWLEGMENTS

The text of this dissertation in part is a reprint of the materials as it appears in: "MoS_2-Graphene Heterostructures as efficient organic compounds sensing 2D materials", Carbon 2019; "MoS_2-Based Optoelectronic Gas Sensor with Sub-Part-per-Billion Limit of NO_2 Gas Detection", ACS Nano 2019. The co-author Dr. Ashok Mulchandani listed in all of these publications directed and supervised the research which forms the basis for this dissertation.

DEDICATION

To my parents and my Pham-ily

ABSTRACT OF THE DISSERTATION

MoS_2 Based Heterostructures for Enhanced Chemical and Biological Sensing

by

Tung Thanh Pham

Doctor of Philosophy, Graduate Program in Chemical and Environmental Engineering
University of California, Riverside, September 2019
Professor Ashok Mulchandani, Chairperson

Two-dimensional (2D) nanomaterials, such as graphene, hold great potential for next-generation electronics owing to their unique properties such as high carrier mobility, fast response time and high transparency. However, the absence of an electrical band gap in graphene limits its applications as a field-effect transistor (FET). To overcome this limitation, other 2D nanomaterials such as transitional metal dichalcogenides (TMDs) have been studied and attracted significant research interests. TMDs consist of 2D stacked layers of covalently bonded transition metal and dichalcogenide atoms arranged in a hexagonal lattice where adjacent layers are held together by relatively weak van der Waals forces. MoS_2 is one such example of TMDs that exhibits a direct band gap of 1.8 eV for single-layer MoS_2 and an indirect band gap of 1.2 eV for multiple-layer structure. FETs based on single-layer MoS_2 exhibit an on/off ratio of > 10^8 at room temperature. However, unlike graphene-based FETs which typically exhibit a high mobility of 5,000 - 10,000 $cm^2V^{-1}s^{-1}$, MoS_2-based FETs show a much lower mobility of ~100 -200 $cm^2V^{-1}s^{-1}$.

One possible way of tailoring the electrical properties of a material is by stacking individual layers of different 2D materials to form a vertical heterostructure. In this dissertation, we explored the electrical properties of graphene - MoS_2 hybrid films synthesized by direct growth of single-

layer and multi-layer MoS_2 on graphene using chemical vapor deposition (CVD). By taking advantage of the high charge carrier mobility of graphene and the finite band gap of MoS_2, we fabricated FETs which consist of graphene - MoS_2 hybrid as the conducting channel. We explored the potential of this new hybrid structure for electro-chemical sensing by testing its selectivity and sensitivity for different volatile organic compounds (VOCs). In addition, we studied an optoelectronic sensor using graphene as electrodes and MoS_2 as conducting/sensing channel. The red-light with matching energy to band gap in single-layer MoS_2 increased electron concentration in MoS_2 and hence promoted the current in the sensor. The optoelectronic sensor was used for NO_2 detection. Another heterostructure of MoS_2 and metal oxide was also investigated for DNA sensor. Finally, we studied the potentials of MoS_2 and graphene heterostructure for a potential flexible and on-skin applications for NO_2 and NO detection.

CONTENTS

List of Figures

CHAPTER 1

Introduction: MoS_2 - A 2D Transition Metal Dichalcogenide (TMD)

1.1 Finding of 2D TMD and MoS_2

2D material has become an emerging field of research after graphene was found in 2004 by Novoselov and Geim group from the University of Manchester.[1] Unlike its bulk structure (graphite), graphene shows many outstanding properties including high charge mobility[1], excellent heat conductivity[2], superior mechanical strength[3] etc. due to its confinement in two dimension lattice.

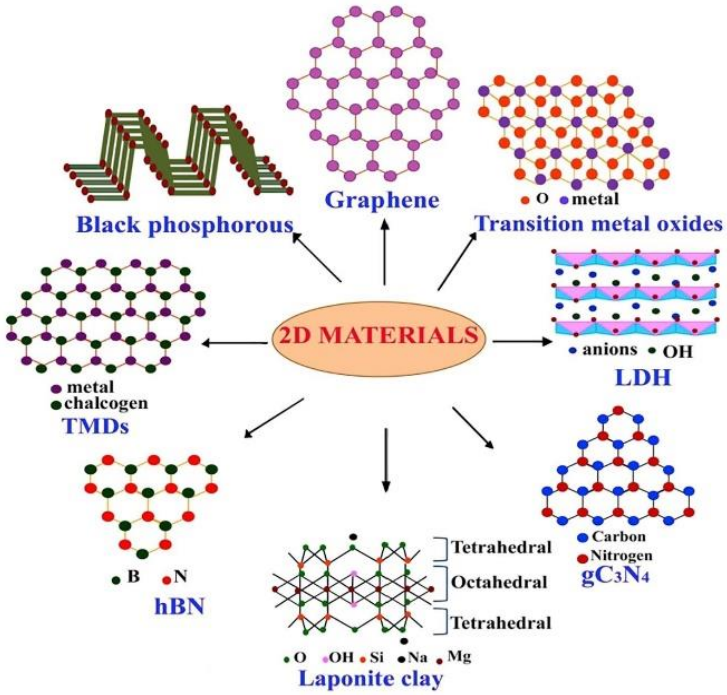

Figure 1.1. Structure of different 2D materials.[9]

These interesting properties create tremendous interest in a broad spectrum of applications ranging from transport[4], medicine[5], electronics[6], energy[7]etc. However, it had not been long until scientists realized graphene suffers from its lack of bandgap which thus limits its applications in logic electronics. A major amount of effort has been spent on bandgap engineering in graphene.

One of the proposed methods successfully introduces a finite 0.4 eV in graphene through a quantum confinement of the charge carrier in pseudo one-dimensional graphene nanoribbon.[8] However, this method requires costly equipment and reduces the charge mobility due to the increase in defect concentration.

As a result, the exploration of other graphene analogous materials has continued, leading to findings of other 2D materials including single element materials such as black phosphorus (BP), silicene, germanene, and compounds such as transition metal chalcogenides/dichalcogenides (TMCs/TMDs), hexagonal boron nitride (hBN) etc. (**Figure 1.1**)[9] Similar to graphene, these materials exhibit distinguishable properties against their bulk structures. For example, molybdenum disulfide (MoS_2) is one of the most widely researched TMDs. This semiconducting material inherits an indirect bandgap of 1.2 eV but transitions to a direct bandgap of 1.9 eV.[10] This renders single-layer (SL) MoS_2 a more suitable material than graphene to fabricate field-effect transistors with on/off ratio exceeding 10^6.[11]

1.2 MoS_2 and sensing applications

Since there is significant increase in public health awareness in recent days, biological and chemical sensors have attracted more attention. This creates an urgent demand of simple operation, rapid detection, high sensitivity, and excellent selectivity for environmental monitoring and medical diagnosis. Metal oxide and conducting polymers have been widely used in sensing applications due to their low cost and ease of fabrication[12–15]. However, metal oxide-based gas sensors often require elevated working temperature due to presence of inactive O^- group at the sensing surface.[16] In fact, metal oxide-based gas sensors usually operate at elevated temperatures higher than 100 ^oC. This not only leads to a high-power consumption, but this also causes electrical drift in sensing signal. On the other hand, conducting polymer-based gas sensors, despite its ability

to operate at room temperature (RT), are susceptible to humidity and result in inevitable continuing degradation in ambient conditions.[17]

Owing an extremely high surface-are-to-volume ratio, 2D materials are considered good candidates for sensing applications with excellent sensitivity. While graphene was the 1st 2D material isolating from its bulk, its semi metallic properties and lack of dangling bonds diminish the device's sensitivity. Therefore, many works have been investigated in order to enhance the sensitivity by introducing additional defects in graphene lattice. The efforts result in a family of graphene derivatives such as graphene oxide, reduced graphene oxide with additional functional groups on their pristine carbon sp^2 surface, such as hydroxyl groups and oxide groups. These

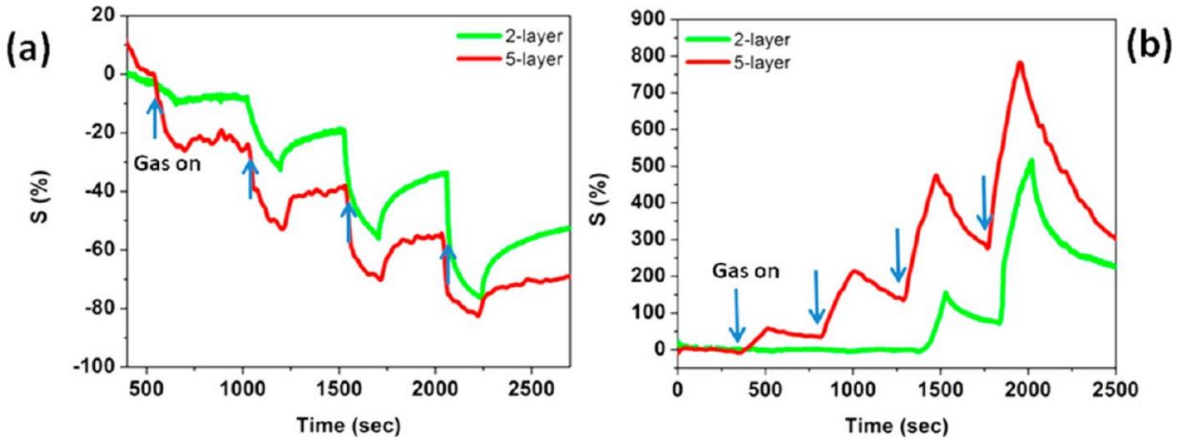

Figure 1.2. Two- and five-layer MoS_2 sensing performance with (a) NH_3 and (b) NO_2 (for 100, 200, 500, 1000 ppm).[18]

functional groups indeed increase the sensitivity; however, these graphene derivatives suffer from reduction of charge carrier due to the increase in number of defects.

TMDs, on the other hand, offer the similar high surface-area-to-volume-ratio like graphene. This morphological property renders TMDs promising candidates for sensing application. In addition, TMDs exhibit a finite bandgap energy which does not exist in intrinsic graphene. One of the most studied TMD materials is molybdenum disulfide (MoS_2) due to its high ambient stability and ease to fabricate in laboratory settings. Similar to graphene, MoS_2 sheets can be isolated from

MoS_2 bulk structure using top down or bottom up methods. Late et al. reported a MoS_2 based gas sensor for NO_2, NH_3, and humidity detection.[18] In this work, a SL and up to 5 layer MoS_2 film was deposited on 300 nm SiO_2/Si substrate via mechanical exfoliation and the lateral size of MoS_2 sheets were about 30 μm.

The isolated MoS_2 showed a profound n-type semiconducting property towards NO_2 and NH_3 gases at different concentrations of 100, 200, 500 and 1000 ppm. NO_2 is well recognized as an electron acceptor while NH_3 acts as an electron donor. As a result, the device experienced an increase and a decrease in resistance to NO_2 and NH_3, respectively based on the charge transfer mechanism (**Figure 1.2**). The group also noticed that thicker MoS_2 film samples had better sensitivity as compared to ones of thinner film. The possible reason is due to the difference in energy band as the number of layers increases. However, it was not discussed further in this work.

Together with chemical sensors, immuno-assay-based sensors use affinity techniques that have found widespread applications in clinical diagnostics and, of late, in environmental monitoring. Quantification in immuno-assay-based sensor is generally achieved by measuring specific label activity, i.e. radioactivity, fluorescence, luminescence (chemi or bio), or enzyme activity. However, labeled immunosensors require lengthy processes involving many incubation steps and the method

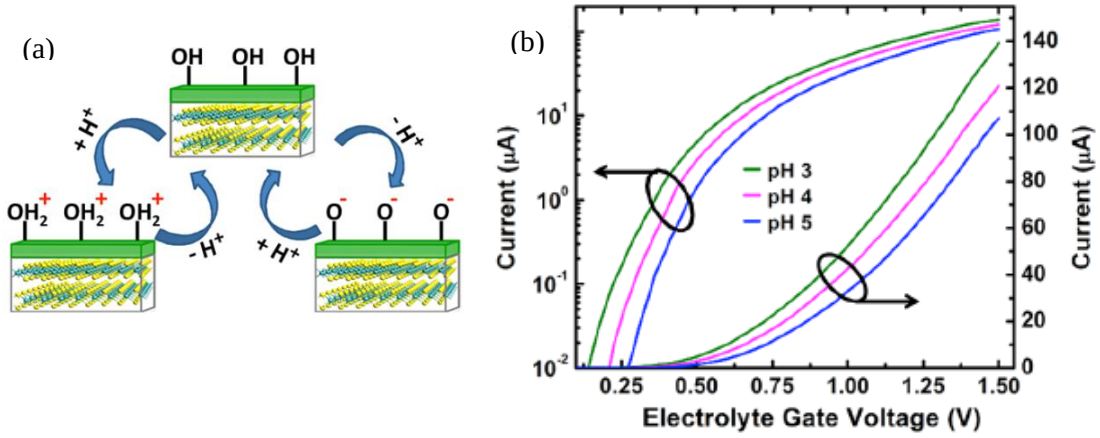

Figure 1.3. MoS_2 FET-based sensor for pH sensing (a) Schematic of the principle of pH sensing (b) Darin current for MoS_2 FET-based sensor at different pH value. [19]

suffers from the lack of an ideal label. Therefore, development of label-free field-effect based (FET) immunosensors has become an emerging field of research as a more advanced alternative. These biosensors measure the modulation of electrical charge carriers across an antibody-modified sensing and conducting channel upon the binding of a charged analyte to the antibody.

As a member of the transition metal dichalcogenide family, MoS_2 is an intrinsically semiconducting material with a direct energy bandgap of 1.9 eV in its single-layer structure. This provides MoS_2 based FETs with high on/off-current ratios and excellent subthreshold swing.[11] These exceptional electrical properties suggests that MoS_2 is a promising candidate for FET-based chemical and biological sensors. In addition, the ultrahigh surface-to-volume ratio allows the materials a Debye length, a measure of the field penetration into the bulk, that is comparable to the size of the nanostructures, and thus, the device sensitivity is significantly improved. In general, the sensing mechanism in FET biosensors includes the induction of a gating effect when a charged biomolecule is captured on the surface of thin film material. This additional effect, in turn, modulates the channel conductance and is transduced into a readable sensing signal. In 2014, Sarkar et al. reported the first MoS_2-based FET biosensor for pH as well as biomolecule detection (**Figure 1.3**).[19]

It demonstrated that the device was more sensitive within the subthreshold region as compared to the saturation and linear regions for pH sensing. It was explained that the drain current was exponentially dependent on the gate potential while it was quadratically and linearly related in the saturation and linear regions, respectively. The atomically thin MoS_2 film and its pristine surface allows excellent subthreshold and, hence, high sensitivity of the device despite the thick 270 nm SiO_2 dielectric layer. The same device also demonstrated a high sensitivity toward a well-known binding between biotin and streptavidin molecules. They achieved a high sensitivity of 196, defined by a percentage change of current before and after the binding event, at 100 femtomolar

concentration, and computationally confirmed that MoS_2 was better sensing material than graphene due to its finite band gap.

1.3 Current challenges and solution

1.3.1 Large-scale production

The weak bond of Van der Waal force between TMDC layers suggests the layers can be isolated via mechanical or chemical exfoliation. The oldest and simplest mechanical exfoliation method is rubbing TMDC bulk against another solid surface. Novoselov et al. reported the delaminated flakes were found SL nanosheets with thickness of 0.7 nm, confirmed by atomic force microscopy (AFM). [20] The more advanced and yet simple mechanical exfoliation involves using scotch-tape cleavage, in which the adhesion between the tape and commercial available crystals of molybdenite sufficiently removes single to few layers of MoS_2 [10,21,22]. These methods result in MoS_2 flakes with a lateral size ranging from few to tens of micrometers, which are not suitable for large-scale production. Despite the simplicity, MoS_2 obtained via this route is inconsistent in shape and size with possible residue from the tape's adhesive.

Liquid phase exfoliation has also been employed to synthesize nanosheets of layered materials. This method relies greatly on a suspension process and direct sonication. The key factor is to prevent re-aggregation of materials after isolation. Therefore, a sufficient surface energy of the chosen solvents is required to overcome the cohesive forces between suspended nanosheets. Cunningham et al. reported a method comprising of 400 minutes long sonication of different TMD materials dispersed in a wide range of organic solvents, yielded nanosheets with lateral dimensions of a few hundred nanometers.[23] This method can be optimized by varying the sonication speed and duration to obtain a larger size of the products. Even though liquid exfoliation has the potential for large-scale production, it is still challenging to reproduce similar sizes and consistent number of layer of MoS_2 flakes.

On the other hand, chemical exfoliation is more advantageous because of its high scalability and sizable products, which is compatible with current existing industrial techniques. This method employs small chemical molecules, so-called intercalants, that intercalate in between material layers to weaken the inter-layer Van der Waal forces and eventually break the bond with the assistance of sonication or thermal shock. Commonly used intercalants, such as n-butyllithium and IBr, are known to further weaken the inter-layer binding due to the charge transfer.[24,25] However, the isolated nanosheets in the solution have a tendency to re-aggregate over time and hence require

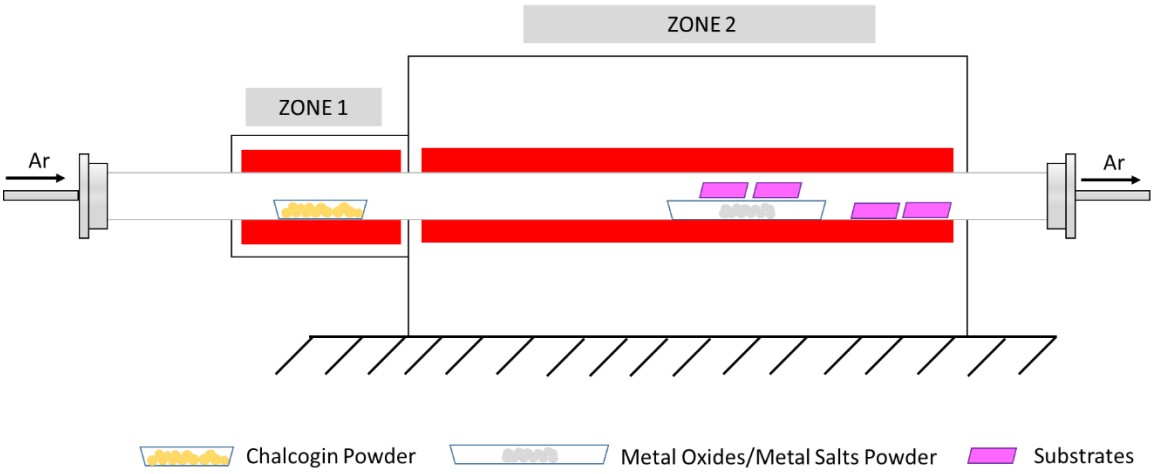

Figure 1.4. Schematic of two-zone furnace for chemical vapor deposition growth of MoS_2.

an additional surface charge or a surfactant to be stabilized. Even though this method is effective, it is known to result in a phase transformation of MoS_2, which will be discussed further in the later section.

While liquid-phase exfoliation and chemical exfoliation provide a potential approach for large-scale production, they pose a challenge due to the lengthy process involving hazardous/explosive chemicals, such as lithium compounds, and it produces relatively small lateral size nanosheets. As a graphene analogue, the chemical vapor deposition method for synthesizing large-area graphene can be applied for TMDs. Lee et al. was the first to synthesize single–layer MoS_2 using CVD

directly on SiO_2/Si substrate.[26] The common set up for CVD growth includes two different heating zones of upstream and downstream in a tube furnace. Chalcogen precursor, such as chalcogen in powder phase, is placed at the upstream location while transition metal, metal oxide or metal salt is fixed at the downstream location where the chalcogenization takes place. Chalcogen element is evaporated under a mild temperature around 150°C-180°C and delivered to the downstream by an inert carrier gas such as nitrogen or argon. In the main zone, the metal precursor is chemically reduced by chalcogen vapor to form TMD in the vapor phase, which then migrates onto the substrate surface located either on top or adjacent to the metal precursor (**Figure 1.4**).

This migration step suggests the substrate surface plays a significant role for CVD growth. Jeon et al. reported a large-area and high quality MoS_2 film up to 2 cm x 2 cm can be achieved on SiO_2 substrate prepared by oxygen plasma treatment.[27] The O_2 plasma treatment provides a higher surface reactivity and better lattice matching for hexagonal MoS_2 growth, which is indicated by the higher binding energies of Si 2p and O 1s peaks. The hydrophilic SiO_2 surface after O_2 plasma treatment further promotes the nucleation and growth of MoS_2. As a result, it was observed that MoS_2 grew in island domains on the untreated SiO_2/Si, whereas full coverage MoS_2 film was seen on the treated substrate. Thicker layers of CVD-grown MoS_2 was also obtained as the time of O_2 plasma treatment was prolonged in this study. Even though SiO_2 is the most common substrate that is used for CVD growth of TMDCs, it yields a random orientation of synthesized domains because of the amorphous nature of the substrate and its relatively high surface roughness. Therefore, higher crystalline substrates such as sapphire, mica, graphene and other 2D insulating substrates are more suitable for CVD growth. Dumcenco et al. used highly polished, EPI-ready grade sapphire substrate to achieve a large-area CVD MoS_2.[28] This growth resulted in single-crystal MoS_2 triangles that merged into a continuous film up of 6 mm x 1 cm area. Also, 97% of observed grain orientation is corresponding to lattice rotation of 0^0 and 60^0 while the remaining is of 30^0. In order to improve the

uniformity of CVD-grown TMDCs on a substrate, another simple and effective strategy is to use seeding promoter. In 2012, Lee et al. reported perylene-3,4,9,10-tetracarboxylic acid tetrapotassium salt (PTAS) is one of potential promoters.[26] PTAS is a good candidate due to its high solubility in water which provides the uniformity on hydrophilic substrate surfaces and also good thermal stability, which is vital during CVD process at relatively high temperature. In presence of the seeding of PTAS, SL- TMD was able to grow directly on different substrates with different morphologies such as Si, aggregates of TiO_2 particles, sapphire, quartz. Similarly, Han et al. reported an advanced CVD synthesis of MoS_2 using lithographical patterning, in which islands of MoO_3 or ammonium haptamolydate (AHM) were deposited at predefined locations on SiO_2/Si substrates and followed by sulfurization.[29] In short, an array of square windows was patterned on a substrate using lithography. Molybdenum precursors, Mo metal or AHM, will be deposited in the

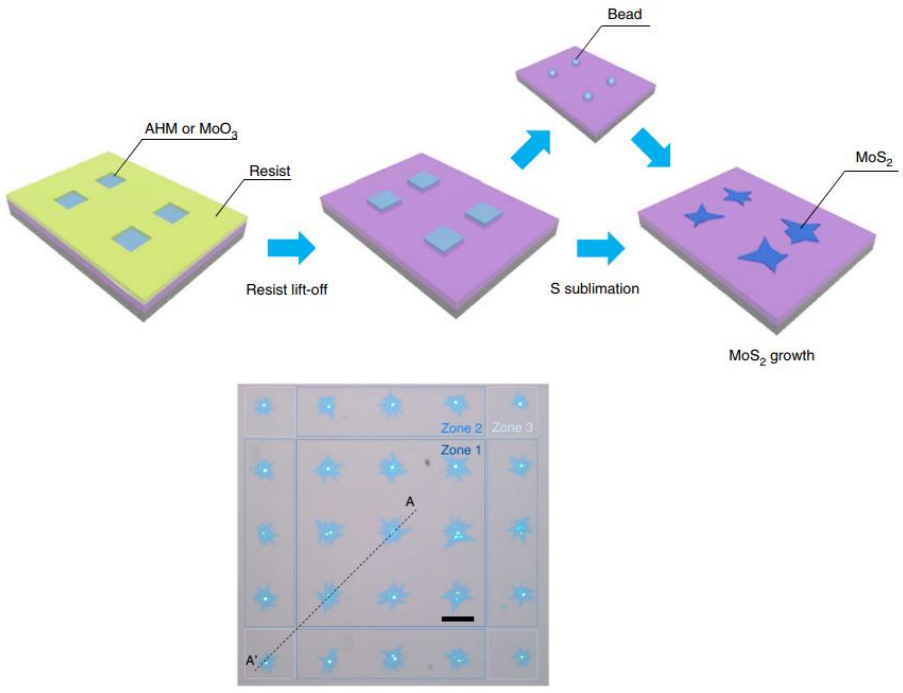

Figure 1.5. Schematic of predefined location of chemical vapor deposition growth of MoS_2 (a) growth procedure (b) Optical images of CVD MoS_2 triangles. [29]

windows using thermal deposition or spin coating, respectively. The subsequent sulfurization step resulted in multiple crystalline domains of MoS_2 in triangular shapes as seen in **Figure 1.5**.

This approach offers high crystallinity of MoS_2, selective location of growth, and elimination of additional etching step to transfer. In addition, it is highly compatible and instantly available for the next lithographical steps of device fabrication.

1.3.2 Low charge mobility

A typical complementary metal oxide semiconductor (CMOS) digital logic device requires a minimum of current on/off ratio in range of 10^4 to 10^7 and a sizable bandgap of 0.4 eV or more[30], which suggests MoS_2 is a great candidate to fabricate a field effect transistor based device. Theoretically, the intrinsic photon-limited charge mobility of MoS_2 is calculated at 410 $cm^2V^{-1}s^{-1}$ at room temperature.[31] However, experimental charge mobility measured at 0.3-5 cm^2V^{-1} s^{-1} hinders MoS_2 in real-life applications. Cheng et al. confirmed that MoS_2's mobility is not governed by the bandgap or the effective mass but is significantly governed by scattering, including defects scattering (more dominant) and scattering from surrounding dielectrics.[32] In fact, sulfur vacancies are predominant in as-grown MoS_2 synthesized by top down (mechanical and chemical exfoliation) and bottom up methods (CVD and thermal annealing).[33,34] Exfoliated MoS_2 requires extensive energy for intercalants to break the van der Waals bonds between MoS_2 sheets. Hence, the mechanical high-power wear and tear during ultrasonication promotes the number of sulfur vacancy defects in the material lattice. On the other hand, as-grown MoS_2 via CVD method experiences the same type of defects due to thermal stresses during the growth process.[33,35] Zhou et al. reported a study on intrinsic structural defects in CVD MoS_2 using direct atomic resolution imaging and first-principle calculations, in which the procedure was done with delicate care to avoid the knock-on damage caused by the beam irradiation.[36] In **Figure 1.6**, six different types of point defects were observed in CVD grown MoS_2, including monosulfur vacancy (V_s) , disulfur

vacancy (V_{s2}), vacancy complex of Mo and nearby three sulfur (Mo_{s2}), vacancy complex of Mo nearby three sulfur pairs (V_{MoS3}), and anti-site defects where a Mo atom substituting a S_2 column (V_{MoS6})or a S_2 column substituting a Mo atom ($S2_{Mo}$).

The structural stability of these point defects was explored through their formation energies using density functional theory (DFT), and sulfur vacancy was observed as the most common defect in MoS_2 lattice due to its lowest formation energy. Furthermore, the presence of sulfur vacancies introduces a deep localized donor state 0.4-0.6 eV[37], which traps electrons and, hence, decreases electron mobility in MoS_2. In addition, charge trapping at the interface of the oxide substrate and the semiconducting channel has been observed previously[38]. Dangling bonds at the surface of SiO_2 form interface states in between SiO_2 and MoS_2. In fact, it was observed that I_{ds} decreased when the gate voltage (V_g) and source-drain bias (V_{ds}) remained constant at 60 V and 1 V, respectively,

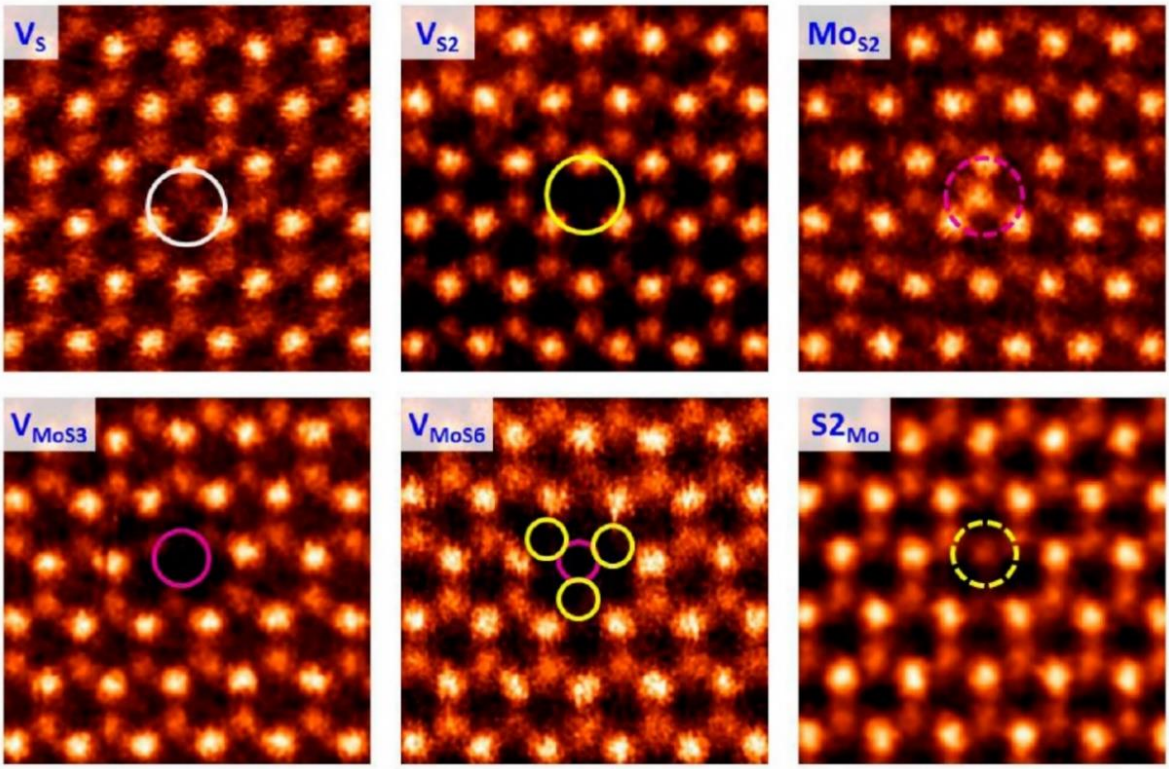

Figure 1.6. Six types of point defects in CVD MoS_2.[36]

because the accumulation of electrons in the traps shielded the MoS_2 channel from the effect of the gate potential (**Figure 1.7**).

In light of finding a solution to mitigate the adverse scattering and trapping effects of defects in MoS_2, many approaches have been investigated including ion implantation, polyethylenimine[39], and self-assembled monolayers[40]. However, the techniques are either not feasible due to the nature of thin film or suffer from poor stability. Chemical treatment, on the other hand, proves to be a more effective approach.[41–43] Sulfur vacancies create unsaturated Mo orbitals which prefer to hybridize other sulfur containing groups to form a stable covalent bond. In fact, molecules with thiol groups (S-H) bind to MoS_2 layer via a strong chemical bonding and, hence, restore the defects

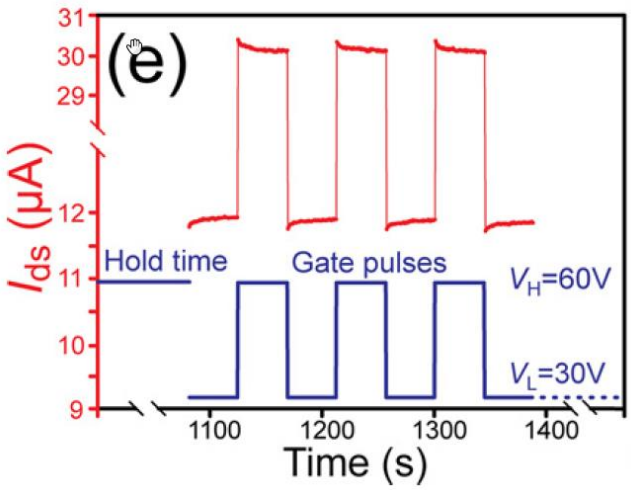

Figure 1.7. Source-drain current at constant V_g= 60 V and V_{ds}= 1V. [38]

in MoS_2 lattice (**Figure 1.8**). Additionally, a pristine MoS_2 surface is free of dangling bonds which makes it challenging to attach another molecule for functionalization; therefore, these thiol compounds sufficiently provide available anchor sites for further surface functionalization. Sim et. al. investigated the physical and electrical properties of MoS_2 upon the adsorption of thiol-based molecules.[44]

Two thiol-terminated molecules of mercaptoethylamine (NH_2-termniated thiol, MEA) and 1H,1H,2H,2H-perfluorodecanethiol (CF_3-terminated thiol, FDT) were used to study the effect of the thiol groups and their terminated functional groups on electrical properties of a MoS_2-based device. The additional peaks in XPS spectra in **Figure 1.8(c), 1.8(d) and 1.8(e)** confirm the strong binding of MEA and FDT molecules on the surface of MoS_2. In addition, these thiol-based molecules, upon binding, triggered charge transfer onto MoS_2. NH_2- group is well known to be an electron donor while F- group is an electron acceptor. In **Figure 1.9**, photoluminescence spectra demonstrated a red shift in MEA-MoS_2 (to the right) and a blue shift in FDT-MoS_2 (to the left) due to the electron transfer phenomenon.

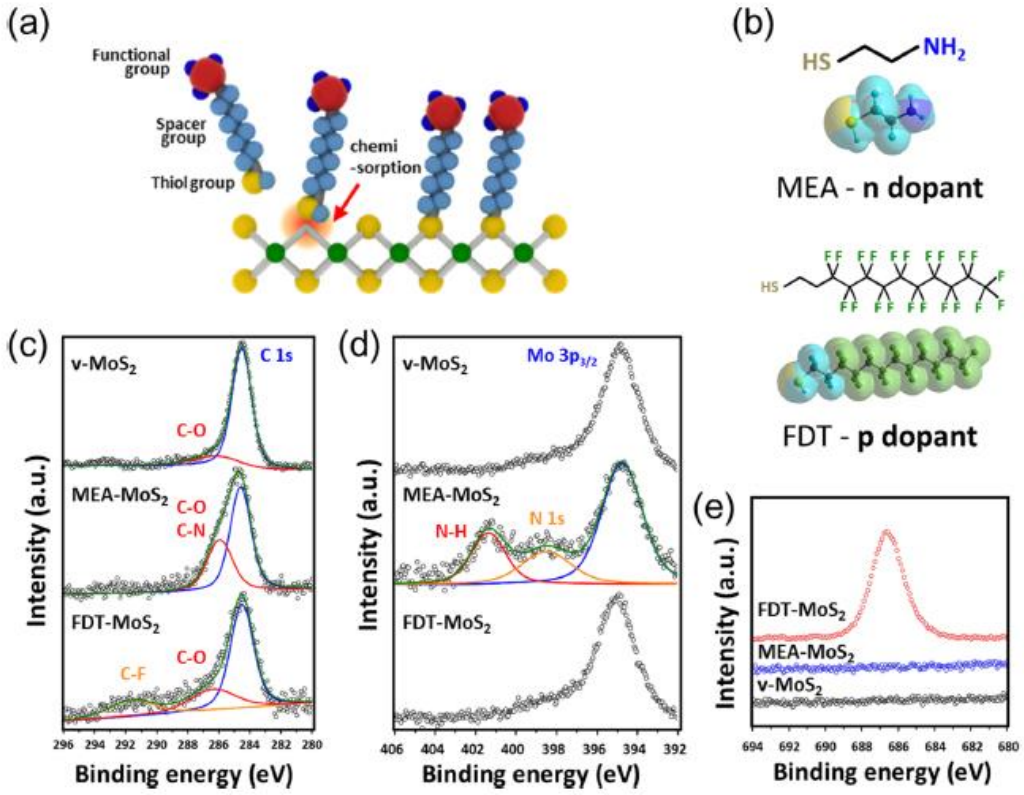

Figure 1.8. Binding of thiol-based molecules in sulfur vacancy defective sites on MoS_2 (a) Schematic of the binding (b) Molecular structure of MEA and FDT. XPS spectra for MoS_2 after functionalization (c) C 1s (d) N 1s (e) F 1s .[41]

Table 1.1. Variation in Threshold Voltage (V_{TH}) of MEA-MoS_2 and FDT-MoS_2 FET Devices

	MEA-MoS_2			FDT-MoS_2		
	undoped	**doped**	**annealed**	**undoped**	**doped**	**annealed**
V_{th} [V]	−25	−38.5	< −40	−27	4	−18.5

[a] V_{th} was defined at V_{GS} having a drain current of 1 nA (constant current method).

The surface charge transfer doping was also confirmed with FET characteristics measurement. It was profound that the threshold voltage (V_{TH}) before and after doping was shifted (**Table 1.1**). N-doping effect in MEA-MoS_2 resulted in a negative shift of V_{TH} while V_{TH} experienced a significant positive shift due to p-doing by FDT. As compared to other methods of functionalization, the device's performance via this method was fully restored via a simple annealing step even after the device aged for 1 week in ambient, confirming an excellent stability of this method. Even though this route of chemical functionalization has many advantages, it still suffers from some limitation. Due to the nature of the binding, the number of thiol group-based binding depends heavily on the number of sulfur vacancies on the surface of MoS_2 film. As a result, the control of subsequent biofunctionalization steps via the functional group terminal on the thiol-based molecule remains as an ongoing challenge.

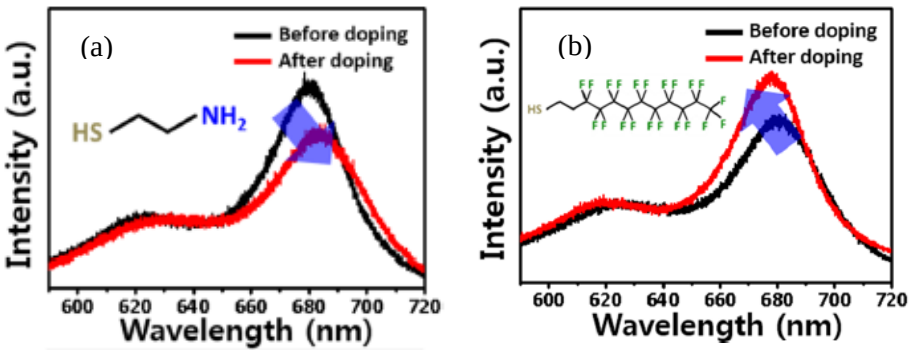

Figure 1.9. PL spectra of functionalized MoS_2 before and after doping process (a)n-doping phenomenon (MEA) (b) p-doping phenomenon (FDT). [41]

1.3.3 High Schottky barrier

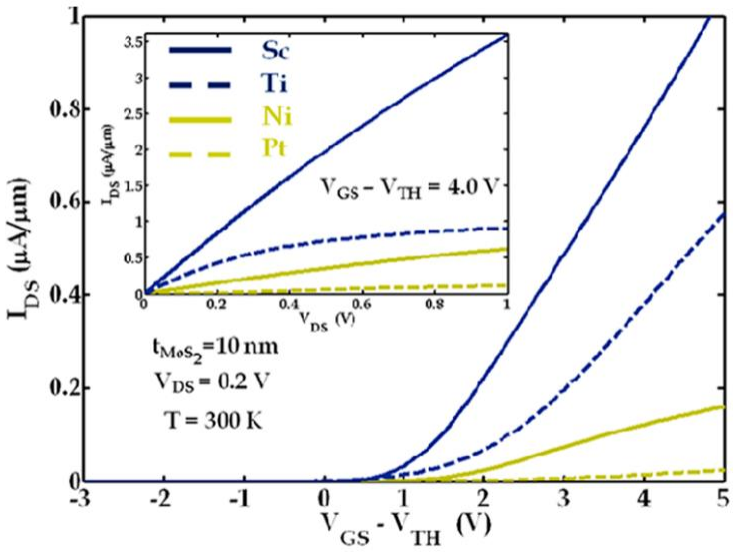

Figure 1.10. FET transfer characteristics curve of 10 nm thin MoS_2 back-gated transistor with Sc, Ti, Ni and Pt metal contacts The inset shows the output current of the corresponding devices for a gate voltage overdrive of 4 V. [46,]

Fermi level pinning in TMD originated in the study of the effect of different contact metals on MoS_2. Due the excellent performance of n-type MoS_2 semiconductors in electronic applications, p-type MoS_2 devices have attracted more attention in order to establish ambipolar MoS_2, which is essential for complementary metal-oxide semiconductor technologies. The intrinsic direct band gap of 1.8 eV in SL structure suggests that MoS_2 devices using high work function metal contact will result in the p-type MoS_2. However, this phenomenon was confirmed otherwise by Kim et. al.[45] both theoretically and experimentally. In this work, pinning factor S was defined by $S = d\Phi_{Bn}/d\Phi_m$, in which

$\Phi_{Bn} = \Phi_m$ *(metal work function of a metal)* $- \chi$ *(electron affinity of the semiconductor)*

S = 1 defines unpinned interface and S = 0 is a strongly pinned interface. Theoretical S value of 0.31 eV higher than the experimental S of 0.11 eV in SL MoS_2 confirmed that Fermi level pinning was significant in band alignment and, hence, responsible for high Schottky barrier in MoS_2 devices. The difference between the two results was attributed to the presence of sulfur vacancy defects in MoS_2. Even though Fermi level pinning severely negates the performance of MoS_2 devices, Das et al. proved that choosing a proper metal contact can alleviate the issue. Das' work investigated the modulation of Schottky barrier using different metal contacts, including Ni, Pt, Ti and Sc.[46] Those metals were chosen due to their low work function (Sc = 3.5 eV, Ti = 4.3 eV) and high work function (Ni = 5.0 eV, Pt = 5.9 eV). However, as illustrated in **Figure 1.10**, high work function metals (Ni and Pt) resulted in the persistent n-type behavior as low work function metals

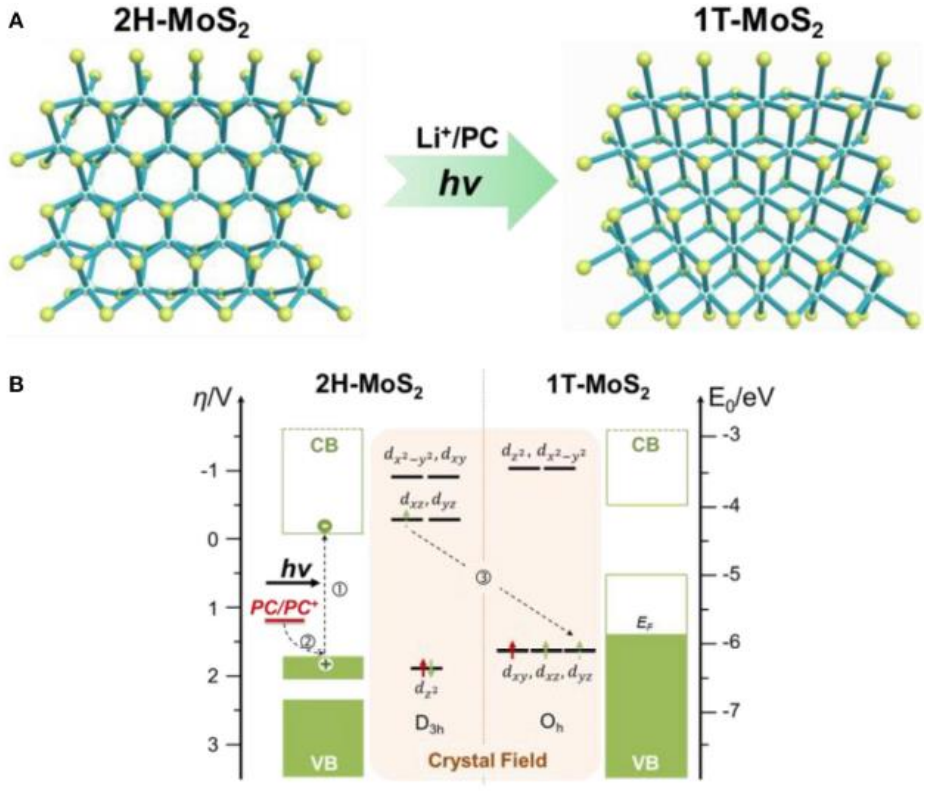

Figure 1.11. Schematic of 2H-and 1T- phase transition in SL MoS_2 (A) Atomic structures of 2H- and 1T-MoS_2 (B) Energy diagram of 2H- and 1T-MoS_2 and the corresponding crystal field of Mo 4d orbitals. [47]

(Sc, Ti) confirmed that MoS_2/metal interface is indeed regulated by Fermi level pinning. However, the increasing magnitude of the current in the transfer characteristics curves is consistent with the increase in work function of the metal that were used. Sc, Ti, Ni and Pt forms a work function of 30 meV, 50 meV, 150 meV and 230 meV, respectively. As a result, the lower Schottky barrier allows smaller contact resistance and, hence, permits better charge flow through the conducting channel. This finding profoundly indicates the importance of selecting a proper metal contact to mitigate the Fermi level pinning effect.

Another approach to alleviate the high Schottky barrier is utilizing phase transition from a semiconducting to metallic MoS_2. Depending on the arrangement of S atoms, SL MoS_2 presents in two distinct symmetries, such as 2H (trigonal prismatic, semiconducting) and 1 T (octahedral, metallic) phases. The 1T phase was first reported to transform from 2H-MoS_2 via Li intercalation.

As shown in **Figure 1.11**, the 2H-MoS_2 has the D_{3h} symmetry and its five Mo 4d orbitals split into three groups: (d_{z^2}), $(d_{xz},\ d_{yz})$, and $(d_{x^2-y^2}, d_{yz})$ orbitals. Molybdenum ion in MoS_2 compound has an oxidation state of 4 and, hence, exhibits 2 electrons in d orbital. Based on the orbital energy level, both electrons reside in the lowest energy d_{z^2} orbital to achieve the most stable energy state. The completely filled d_{z^2} orbital results in 2H-MoS_2 semiconducting properties. On the other hand, a centrosymmetric O_h symmetry in 1T-MoS_2 arranges the Mo 4d orbitals into two

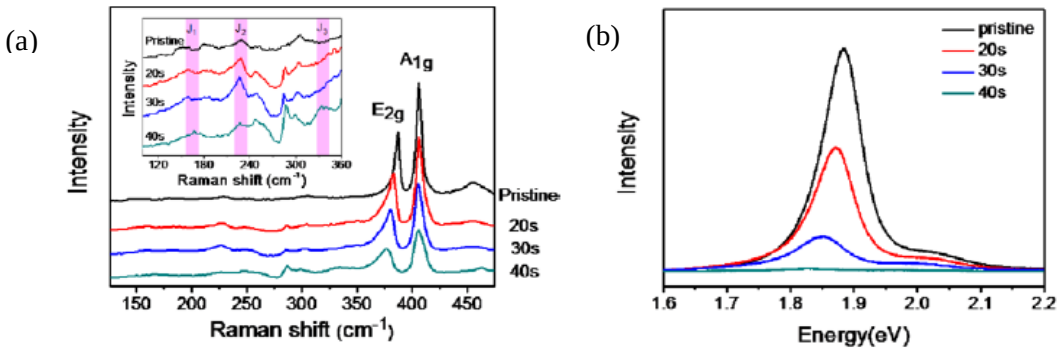

Figure 1.12. Spectroscopic measurement of 1T-MoS_2 (a) Raman Spectra (b) PL of MoS_2 and plasma-treated MoS_2 at different treatment duration. [50]

groups: (d_{xy}, d_{xz}, d_{yz}) and $(d_{z^2}, d_{x^2-y^2})$. Therefore, the two electrons in the d orbital have to fill in 2 of the 3 orbitals instead, leaving an incomplete orbital on the ground state and, hence, making 1T-MoS_2 metallic. In addition, the d_{z^2} orbital in 2H-MoS_2 residing in a lower energy level than the one in 1T-MoS_2 confirms that the semiconducting 2H phase is more thermodynamically stable than the metallic 1T phase. However, when the 2H-MoS_2 receives an additional electron, the extra electron will be allocated to (d_{xz}, d_{yz}) due to the fully occupied d_{z^2} orbital resulting in the destabilization of 2H-MoS_2 phase. On the other hand, the incomplete (d_{xy}, d_{xz}, d_{yz}) orbitals in 1T phase can accept the additional electron resulting in a stable half-filled configuration. The stable configuration in 1T-MoS_2 thus allows the phase transition to occur, suggesting electron injection induces the phase transition in MoS_2. Number of methods to promote the phase transition in MoS_2 have been reported, including alkali intercalated exfoliation[47], electrochemical sulfur etching[48], and light irradiation with induced Au NPs formation[49]. Recently, Zhu et. al. reported a simple MoS_2 phase transition method using argon plasma.[50] The introduction of Ar radicals in plasma initiated the lateral sliding of top S-layer which caused the 1T phase transition. The evidence of 1T formation included the presence of three weak but distinct peaks J_1, J_2, J_3 at 167, 227 and 334 cm^{-1} in the Raman spectra (**Figure 1.12(a)**).

In addition, PL spectra in **Figure 1.12(b)** illustrate the existing peak corresponding with the intrinsic direct bandgap of 1.8 eV in SL MoS_2 PL completely ceased after 40 s of argon plasma

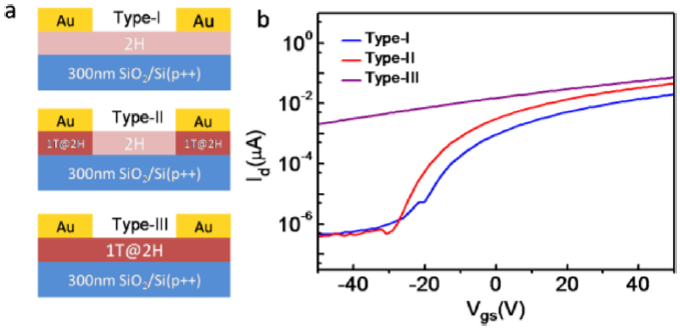

Figure 1.13. Performance of MoS_2 based FET device (a) Schematic of three different device structures (b) Transfer characteristics of three back-gated MoS_2 devices. [50]

treatment, confirming MoS_2 no longer exhibited semiconducting properties but transformed to metallic phase. This phase transformation method was recommended highly compatible with standard lithography techniques. In fact, FET devices were fabricated with this metallic 1T MoS_2 in order to effectively decrease the contact resistance and improve devices' electrical performances. Three types of devices, as seen in **Figure 1.13(a),** were fabricated using standard lithography and phase transition techniques. Type I device showed a typical semiconducting MoS_2 channel, where type III devices showed a minimal on/off current ratio and yet higher current magnitude due to its metallic properties. In addition, type2 device, due to the continuity between metallic 1T-MoS_2 contact and the semiconducting 2H-MoS_2 channel, demonstrated an improved current as compared to the Au contact/2H-MoS_2.

1.4 Future potentials

As discussed above, the major ongoing challenges of MoS_2 in electronic applications include mass-scale production, low charge mobility and high Schottky barrier. Current research and development have taken production scale to another level that is relatively sustainable for wafer-scale application of MoS_2 film in micro/nano electronic devices. On the other hand, sulfur vacancies in MoS_2 diminish the theoretical high charge mobility in MoS_2. Even though the chemical healing method effectively mitigates the issue, the method constantly suffers from poor stability when the device is exposed to ambient conditions. While high Schottky barrier poses one of the most challenging issues, it can be alleviated using phase transition techniques or selecting a proper metal contact to minimize the Schottky barrier height at the contact/MoS_2 interface. However, the process of phase transition requires a strong oxidizing chemical and selection of proper metal is limited. Moreover, the metallic phase is unstable and easy to be reversed to the semiconducting phase under elevated heat. These current challenges demand better approaches to maximize the potential of MoS_2 in real life application. Overall, MoS_2 exhibits many outstanding properties, and there are

many opportunities for development in order to bring this 2D material closer to the current silicon industries.

1.5 Objectives of this work

As per discussion in the above section, with respect to the current limitation of MoS_2 based devices, the objectives of this thesis are

a) **Objective 1**: Develop different methods to synthesize MoS_2 based heterostructures using chemical vapor deposition and characterize the new structures.

b) **Objective 2**: Fabricate field-effect transistor (FET) using a vertical graphene-MoS_2 heterostructure for detection of Volatile Organic Compounds (VOCs).

c) **Objective 3**: Fabricate field-effect transistor (FET) using a vertical metal oxide-MoS_2 heterostructure for detection of single stranded DNA.

d) **Objective 4**: Experimentally investigate the optoelectronic device using graphene electrodes and MoS_2 as conducting/sensing channel for detection of NO_2.

e) **Objective 5**: Explore the potential of MoS_2 and graphene heterostructure in flexible and on-skin application for detection of NO and NO_2.

1.6 Organization of this thesis

Chapter 2 discusses a vertical heterostructure of graphene and MoS_2 for detection of NO_2. Chapter 3 explores the application of optoelectronic devices using graphene as electrodes and MoS_2 as the sensing channel for improved detection of NO_2. Chapter 4 explains the benefit of using Al_2O_3 and MoS_2 heterostructure for enhanced DNA sensing. Chapter 5 discusses the potential of graphene and MoS_2 for flexible on-skin devices. Chapter 6 concludes remarks of this dissertation and provides guidance for future work.

1.7 References

(1) Novoselov, K. S. Electric Field Effect in Atomically Thin Carbon Films. *Science* **2004**, *306* (5696), 666–669. https://doi.org/10.1126/science.1102896.

(2) Balandin, A. A.; Ghosh, S.; Bao, W.; Calizo, I.; Teweldebrhan, D.; Miao, F.; Lau, C. N. Superior Thermal Conductivity of Single-Layer Graphene. *Nano Lett.* **2008**, *8* (3), 902–907. https://doi.org/10.1021/nl0731872.

(3) Lee, C.; Wei, X.; Kysar, J. W.; Home, J. Measurement of the Elastic Properties and Intrinsic Strength of Monolayer Graphene. *Science* **2008**, *321* (5887), 385–388. https://doi.org/10.1126/science.1157996.

(4) Nair, R. R.; Wu, H. A.; Jayaram, P. N.; Grigorieva, I. V.; Geim, A. K. Unimpeded Permeation of Water Through Helium-Leak-Tight Graphene-Based Membranes. *Science* **2012**, *335* (6067), 442–444. https://doi.org/10.1126/science.1211694.

(5) Yang, K.; Zhang, S.; Zhang, G.; Sun, X.; Lee, S.-T.; Liu, Z. Graphene in Mice: Ultrahigh In Vivo Tumor Uptake and Efficient Photothermal Therapy. *Nano Lett.* **2010**, *10* (9), 3318–3323. https://doi.org/10.1021/nl100996u.

(6) Recent advances in graphene-based biosensors | Elsevier Enhanced Reader https://reader.elsevier.com/reader/sd/pii/S095656631100336 8?token=29D8DA3E3EED87DAB7C6E8319DE1F44CF2D92532EDDAB5B973338324ADA43BA3EA11897AA1DCDF97E07380BC7E860348 (accessed Aug 7, 2019).

(7) Stoller, M. D.; Park, S.; Zhu, Y.; An, J.; Ruoff, R. S. Graphene-Based Ultracapacitors. *Nano Lett.* **2008**, *8* (10), 3498–3502. https://doi.org/10.1021/nl802558y.

(8) Yu, W. J.; Duan, X. Tunable Transport Gap in Narrow Bilayer Graphene Nanoribbons. *Sci Rep* **2013**, *3* (1), 1248. https://doi.org/10.1038/srep01248.

(9)2D materials for next generation healthcare applications | Elsevier Enhanced Reader https://reader.elsevier.com/reader/sd/pii/S037851731830700 2?token=6EED1F4FCBE4F7C1205ACF1B48E0BFFBE33E78FF9F393D0C660D1A89E4ED9D9052F7F6B40F5339FB8729791C67A8ACBA (accessed Aug 16, 2019). https://doi.org/10.1016/j.ijpharm.2018.09.041.

(10) Mak, K. F.; Lee, C.; Hone, J.; Shan, J.; Heinz, T. F. Atomically Thin MoS 2 : A New Direct-Gap Semiconductor. *Phys. Rev. Lett.* **2010**, *105* (13), 136805. https://doi.org/10.1103/PhysRevLett.105.136805.

(11) Radisavljevic, B.; Radenovic, A.; Brivio, J.; Giacometti, V.; Kis, A. Single-Layer MoS2 Transistors. *Nature Nanotechnology* **2011**, *6* (3), 147–150. https://doi.org/10.1038/nnano.2010.279.

(12) Janata, J.; Josowicz, M. Conducting Polymers in Electronic Chemical Sensors. *Nature Mater* **2003**, *2* (1), 19–24. https://doi.org/10.1038/nmat768.

(13) Miasik, J. J.; Hooper, A.; Tofield, B. C. Conducting Polymer Gas Sensors. *J. Chem. Soc., Faraday Trans. 1* **1986**, *82* (4), 1117. https://doi.org/10.1039/f19868201117.

(14) Wetchakun, K.; Samerjai, T.; Tamaekong, N.; Liewhiran, C.; Siriwong, C.; Kruefu, V.; Wisitsoraat, A.; Tuantranont, A.; Phanichphant, S. Semiconducting Metal Oxides as Sensors for Environmentally Hazardous Gases. *Sensors and Actuators B: Chemical* **2011**, *160* (1), 580–591. https://doi.org/10.1016/j.snb.2011.08.032.

(15) Fine, G. F.; Cavanagh, L. M.; Afonja, A.; Binions, R. Metal Oxide Semi-Conductor Gas Sensors in Environmental Monitoring. *Sensors* **2010**, *10* (6), 5469–5502. https://doi.org/10.3390/s100605469.

(16) Ponzoni, A.; Baratto, C.; Cattabiani, N.; Falasconi, M.; Galstyan, V.; Nunez-Carmona, E.; Rigoni, F.; Sberveglieri, V.; Zambotti, G.; Zappa, D. Metal Oxide Gas Sensors, a Survey of Selectivity Issues Addressed at the SENSOR Lab, Brescia (Italy). *Sensors* **2017**, *17* (4), 714. https://doi.org/10.3390/s17040714.

(17) Cheah, R.; Forsyth, M.; Truong, V.-T. PII: S0379-6779(98)00006-X | Elsevier Enhanced Reader https://reader.elsevier.com/reader/sd/pii/S037967799800006X?token=0B15BFFD86C828953244105EF54A911FC34FBE3AB2F3238469F97EC1D33E5B7FE072E306472FA571B1BF0B9071126CF9 (accessed Aug 11, 2019). https://doi.org/10.1016/S0379-6779(98)00006-X.

(18) Late, D. J.; Huang, Y.-K.; Liu, B.; Acharya, J.; Shirodkar, S. N.; Luo, J.; Yan, A.; Charles, D.; Waghmare, U. V.; Dravid, V. P.; et al. Sensing Behavior of Atomically Thin-Layered MoS_2 Transistors. *ACS Nano* **2013**, *7* (6), 4879–4891. https://doi.org/10.1021/nn400026u.

(19) Sarkar, D.; Liu, W.; Xie, X.; Anselmo, A. C.; Mitragotri, S.; Banerjee, K. MoS_2 Field-Effect Transistor for Next-Generation Label-Free Biosensors. *ACS Nano* **2014**, *8* (4), 3992–4003. https://doi.org/10.1021/nn5009148.

(20) Novoselov, K. S.; Jiang, D.; Schedin, F.; Booth, T. J.; Khotkevich, V. V.; Morozov, S. V.; Geim, A. K. Two-Dimensional Atomic Crystals. 3.

(21) Lopez-Sanchez, O.; Lembke, D.; Kayci, M.; Radenovic, A.; Kis, A. Ultrasensitive Photodetectors Based on Monolayer MoS2. *Nature Nanotech* **2013**, *8* (7), 497–501. https://doi.org/10.1038/nnano.2013.100.

(22) Wang, Q. H.; Kalantar-Zadeh, K.; Kis, A.; Coleman, J. N.; Strano, M. S. Electronics and Optoelectronics of Two-Dimensional Transition Metal Dichalcogenides. *Nature Nanotech* **2012**, *7* (11), 699–712. https://doi.org/10.1038/nnano.2012.193.

(23) Cunningham, G.; Lotya, M.; Cucinotta, C. S.; Sanvito, S.; Bergin, S. D.; Menzel, R.; Shaffer, M. S. P.; Coleman, J. N. Solvent Exfoliation of Transition Metal Dichalcogenides: Dispersibility of Exfoliated Nanosheets Varies Only Weakly between Compounds. *ACS Nano* **2012**, *6* (4), 3468–3480. https://doi.org/10.1021/nn300503e.

(24) Eda, G.; Fujita, T.; Yamaguchi, H.; Voiry, D.; Chen, M.; Chhowalla, M. Coherent Atomic and Electronic Heterostructures of Single-Layer MoS $_2$. *ACS Nano* **2012**, *6* (8), 7311–7317. https://doi.org/10.1021/nn302422x.

(25) Shih, C.-J.; Vijayaraghavan, A.; Krishnan, R.; Sharma, R.; Han, J.-H.; Ham, M.-H.; Jin, Z.; Lin, S.; Paulus, G. L. C.; Reuel, N. F.; et al. Bi- and Trilayer Graphene Solutions. *Nature Nanotech* **2011**, *6* (7), 439–445. https://doi.org/10.1038/nnano.2011.94.

(26) Synthesis of Large-Area MoS2 Atomic Layers with Chemical Vapor Deposition - Lee - 2012 - Advanced Materials - Wiley Online Library https://onlinelibrary.wiley.com/doi/epdf/10.1002/adma.201104798 (accessed Aug 12, 2019).

(27) Jeon, J.; Jang, S. K.; Jeon, S. M.; Yoo, G.; Park, J.; Lee, S. Controlling Grain Size and Continuous Layer Growth in Two-Dimensional MoS2Films for Nanoelectronic Device Application. *IEEE Transactions on Nanotechnology* **2015**, *14* (2), 238–242. https://doi.org/10.1109/TNANO.2014.2381667.

(28) Dumcenco, D.; Ovchinnikov, D.; Marinov, K.; Lazić, P.; Gibertini, M.; Marzari, N.; Sanchez, O. L.; Kung, Y.-C.; Krasnozhon, D.; Chen, M.-W.; et al. Large-Area Epitaxial Monolayer MoS $_2$. *ACS Nano* **2015**, *9* (4), 4611–4620. https://doi.org/10.1021/acsnano.5b01281.

(29) Han, G. H.; Kybert, N. J.; Naylor, C. H.; Lee, B. S.; Ping, J.; Park, J. H.; Kang, J.; Lee, S. Y.; Lee, Y. H.; Agarwal, R.; et al. Seeded Growth of Highly Crystalline Molybdenum Disulphide Monolayers at Controlled Locations. *Nat Commun* **2015**, *6* (1), 6128. https://doi.org/10.1038/ncomms7128.

(30)Schwierz, F. Graphene Transistors. *Nature Nanotech* **2010**, *5* (7), 487–496. https://doi.org/10.1038/nnano.2010.89.

(31) Yu, Z.; Ong, Z.-Y.; Li, S.; Xu, J.-B.; Zhang, G.; Zhang, Y.-W.; Shi, Y.; Wang, X. Analyzing the Carrier Mobility in Transition-Metal Dichalcogenide MoS2 Field-Effect Transistors. *Advanced Functional Materials* **2017**, *27* (19), 1604093. https://doi.org/10.1002/adfm.201604093.

(32) Cheng, L.; Liu, Y. What Limits the Intrinsic Mobility of Electrons and Holes in Two Dimensional Metal Dichalcogenides? *J. Am. Chem. Soc.* **2018**, *140* (51), 17895–17900. https://doi.org/10.1021/jacs.8b07871.

(33) Hong, J.; Hu, Z.; Probert, M.; Li, K.; Lv, D.; Yang, X.; Gu, L.; Mao, N.; Feng, Q.; Xie, L.; et al. Exploring Atomic Defects in Molybdenum Disulphide Monolayers. *Nat Commun* **2015**, *6* (1), 6293. https://doi.org/10.1038/ncomms7293.

(34) Qiu, H.; Xu, T.; Wang, Z.; Ren, W.; Nan, H.; Ni, Z.; Chen, Q.; Yuan, S.; Miao, F.; Song, F.; et al. Hopping Transport through Defect-Induced Localized States in Molybdenum Disulphide. *Nat Commun* **2013**, *4* (1), 2642. https://doi.org/10.1038/ncomms3642.

(35) Schmidt, H.; Wang, S.; Chu, L.; Toh, M.; Kumar, R.; Zhao, W.; Castro Neto, A. H.; Martin, J.; Adam, S.; Özyilmaz, B.; et al. Transport Properties of Monolayer MoS_2 Grown by Chemical Vapor Deposition. *Nano Lett.* **2014**, *14* (4), 1909–1913. https://doi.org/10.1021/nl4046922.

(36) Zhou, W.; Zou, X.; Najmaei, S.; Liu, Z.; Shi, Y.; Kong, J.; Lou, J.; Ajayan, P. M.; Yakobson, B. I.; Idrobo, J.-C. Intrinsic Structural Defects in Monolayer Molybdenum Disulfide. *Nano Lett.* **2013**, *13* (6), 2615–2622. https://doi.org/10.1021/nl4007479.

(37) Li, L.; Long, R.; Bertolini, T.; Prezhdo, O. V. Sulfur Adatom and Vacancy Accelerate Charge Recombination in MoS_2 but by Different Mechanisms: Time-Domain Ab Initio Analysis. *Nano Lett.* **2017**, *17* (12), 7962–7967. https://doi.org/10.1021/acs.nanolett.7b04374.

(38) Guo, Y.; Wei, X.; Shu, J.; Liu, B.; Yin, J.; Guan, C.; Han, Y.; Gao, S.; Chen, Q. Charge Trapping at the MoS_2-SiO_2 Interface and Its Effects on the Characteristics of MoS_2 Metal-Oxide-Semiconductor Field Effect Transistors. *Appl. Phys. Lett.* **2015**, *106* (10), 103109. https://doi.org/10.1063/1.4914968.

(39) Du, Y.; Liu, H.; Neal, A. T.; Si, M.; Ye, P. D. Molecular Doping of Multilayer ${\rm MoS}_{2}$ Field-Effect Transistors: Reduction in Sheet and Contact Resistances. *IEEE Electron Device Lett.* **2013**, *34* (10), 1328–1330. https://doi.org/10.1109/LED.2013.2277311.

(40) High-Performance Transition Metal Dichalcogenide Photodetectors Enhanced by Self-Assembled Monolayer Doping - Kang - 2015 - Advanced Functional Materials - Wiley Online Library https://onlinelibrary.wiley.com/doi/epdf/10.1002/adfm.201501170 (accessed Aug 13, 2019).

(41) Cho, K.; Min, M.; Kim, T.-Y.; Jeong, H.; Pak, J.; Kim, J.-K.; Jang, J.; Yun, S. J.; Lee, Y. H.; Hong, W.-K.; et al. Electrical and Optical Characterization of MoS_2 with Sulfur Vacancy Passivation by Treatment with Alkanethiol Molecules. *ACS Nano* **2015**, *9* (8), 8044–8053. https://doi.org/10.1021/acsnano.5b04400.

(42) Lu, H.; Kummel, A.; Robertson, J. Passivating the Sulfur Vacancy in Monolayer MoS_2. *APL Materials* **2018**, *6* (6), 066104. https://doi.org/10.1063/1.5030737.

(43) Makarova, M.; Okawa, Y.; Aono, M. Selective Adsorption of Thiol Molecules at Sulfur Vacancies on MoS_2 (0001), Followed by Vacancy Repair via S–C Dissociation. *The Journal of Physical Chemistry C* **2012**, *116* (42), 22411–22416. https://doi.org/10.1021/jp307267h.

(44) Sim, D. M.; Kim, M.; Yim, S.; Choi, M.-J.; Choi, J.; Yoo, S.; Jung, Y. S. Controlled Doping of Vacancy-Containing Few-Layer MoS_2 *via* Highly Stable Thiol-Based Molecular Chemisorption. *ACS Nano* **2015**, *9* (12), 12115–12123. https://doi.org/10.1021/acsnano.5b05173.

(45) Kim, C.; Moon, I.; Lee, D.; Choi, M. S.; Ahmed, F.; Nam, S.; Cho, Y.; Shin, H.-J.; Park, S.; Yoo, W. J. Fermi Level Pinning at Electrical Metal Contacts of Monolayer Molybdenum

Dichalcogenides. *ACS Nano* **2017**, *11* (2), 1588–1596. https://doi.org/10.1021/acsnano.6b07159.

(46) Das, S.; Chen, H.-Y.; Penumatcha, A. V.; Appenzeller, J. High Performance Multilayer MoS_2 Transistors with Scandium Contacts. *Nano Lett.* **2013**, *13* (1), 100–105. https://doi.org/10.1021/nl303583v.

(47) Li, Y.; Wang, L.; Zhang, S.; Dong, X.; Song, Y.; Cai, T.; Liu, Y. Cracked Monolayer 1T MoS_2 with Abundant Active Sites for Enhanced Electrocatalytic Hydrogen Evolution. *Catal. Sci. Technol.* **2017**, *7* (3), 718–724. https://doi.org/10.1039/C6CY02649D.

(48) Gan, X.; Lee, L. Y. S.; Wong, K.; Lo, T. W.; Ho, K. H.; Lei, D. Y.; Zhao, H. 2H/1T Phase Transition of Multilayer MoS_2 by Electrochemical Incorporation of S Vacancies. *ACS Appl. Energy Mater.* **2018**, *1* (9), 4754–4765. https://doi.org/10.1021/acsaem.8b00875.

(49) Kang, Y.; Najmaei, S.; Liu, Z.; Bao, Y.; Wang, Y.; Zhu, X.; Halas, N. J.; Nordlander, P.; Ajayan, P. M.; Lou, J.; et al. Plasmonic Hot Electron Induced Structural Phase Transition in a MoS2 Monolayer. *Advanced Materials* **2014**, *26* (37), 6467–6471. https://doi.org/10.1002/adma.201401802.

(50) Zhu, J.; Wang, Z.; Yu, H.; Li, N.; Zhang, J.; Meng, J.; Liao, M.; Zhao, J.; Lu, X.; Du, L.; et al. Argon Plasma Induced Phase Transition in Monolayer MoS_2. *J. Am. Chem. Soc.* **2017**, *139* (30), 10216–10219. https://doi.org/10.1021/jacs.7b05765.

CHAPTER 2

Graphene-MoS_2 Heterostructure As a Chemical Sensing Material

2.1 Introduction

Two-dimensional (2D) van der Waals (vdW) materials including graphene and transition metal dichalcogenides (TMDs) have recently gathered increasing interests in research communities owing to their intriguing electrical, thermal and optical properties.[1] Graphene consists of sp^2-bonded carbon atoms arranged in a honeycomb lattice and exhibits exceptional properties such as high carrier mobility up to 10^5 $cm^2V^{-1}s^{-1}$ at room temperature, thermal conductivity above 3,000 $Wm^{-1}K^{-1}$, and high optical transparency (~97.7%).[2] However, the absence of a band gap in graphene has limited its applications in electronic devices.

TMDs, chemically abbreviated as MX_2, where M is a transition metal atom (Mo, W, etc.) and X is a chalcogen atom (S, Se, Te, etc.), exhibit a wide range of electrical properties from insulating or semi-conducting to metallic depending upon their crystalline phase.[3,4] One of the most widely researched TMD is molybdenum disulfide (MoS_2). This semi-conducting material possesses an indirect band gap of 1.29 eV in its bulk form but transitions to a direct band gap of 1.9 eV in single layer (SL) structure.[5,6] Due to this sizable band gap, FETs using MoS_2 as the conducting channel exhibit high on/off ratios in the range of 10^4-10^6 and very low power leakage in off-state.[7] However, usage of MoS_2 as a channel material for the future devices is limited by its low charge mobility in the range of ~0.1−100 $cm^2V^{-1}s^{-1}$.[8] Additionally, due to the presence of a high Schottky barrier between metal contacts and MoS_2 layers and poor interface quality, the transport in channel is susceptible to high contact resistance.[9]

One of the proposed solutions to mitigate these limitations is fabrication of a heterostructure that can utilize the complementary properties of MoS_2 and graphene, such as high carrier mobility

and Schottky barrier tunability of graphene and sizable band gap of MoS_2.[10] Similar to the constituent layered materials, these heterostructures are held together by weak interlayer vdW forces. Prior studies on graphene-TMD heterostructures have relied on artificial stacking of individual 2D crystals using mechanical exfoliation and stamping, which usually results in atomically sharp interfaces that are free from any polymer/chemical residue.[11,12] However, mechanical exfoliation of 2D crystals is not a scalable approach, and hence, not suitable for commercial applications. A more scalable approach of fabricating such 2D heterostructures is via physical stacking of thin films synthesized via CVD.[13-18]

FET-based sensors are of interest since they allow on-chip integration of thin films including graphene and TMDs for label-free, highly sensitive and rapid detection of chemicals/biomolecules by fabricating low-power, inexpensive, portable devices. In these thin film FET-based sensors, any surface perturbation created by affinity-based binding or adsorption of chemicals leads to change in the current between the source and drain electrodes due to the extremely high surface-to-volume ratio of the channel material, and this allows for label-free sensing applications. There have been multiple reports in literature on FET-based sensors that utilize graphene or MoS_2 as the channel material.[19,20,21] Though these ultra-scale homogeneous 2D FETs exhibit promise as sensors and flexible electronics, the operational parameters are far from the desired values mainly due to poor surface quality leading to inefficient selectivity and low signal-to-noise ratio (SNR).

In this paper, we investigate the performance of MoS_2/graphene, hereafter referred to as MS/G, based FETs for chemical sensing of volatile organic compounds (VOCs) such as toluene. High quality graphene and MoS_2 thin film were synthesized using CVD on polycrystalline copper and sapphire substrate, respectively, and physically stacked on a Si/SiO_2 substrate to obtain MS/G. FET devices were fabricated with graphene, MoS_2 or MS/G as the channel material and 300 nm Si as the back gate. Upon stacking of MoS_2 over graphene, we observed significant photoluminescence

(PL) quenching of MoS_2 and a shift in charge neutrality point (V_{CNP}) to lower gate voltage in MS/G FET as compared to graphene FET due to n-doping effect in graphene. The shift in energy level for the heterostructure is further explained and confirmed by ultraviolet photoelectron spectroscopy (UPS), electrical double layer-capacitance (C_{EDL}) versus voltage and first-principle simulations. These observations were in-line with the results obtained for other graphene-TMDC heterostructures fabricated by mechanically exfoliated crystals and paves the way for exploring CVD as a scalable route for fabrication of high quality vdW heterostructures.[22-24] We also observed that unlike the graphene FET, the MS/G FET was less susceptible to doping from ambient air and showed excellent stability with negligible shift of V_{CNP} in dry air over time. This stability and robustness of the channel material is vital for FET-based sensors that rely on shift in transfer characteristics for sensitive detection of chemicals with low limit of detection. Finally, we compared the performance of graphene, MoS_2 and MS/G FETs for dynamic sensing of toluene vapor by performing chronocurrent measurements. The response of the three FETs to toluene has shown MS/G based device has the highest sensitivity and selectivity due to its high surface area-to-volume ratio and high SNR ratio.

2.2 Experimental details

2.2.1 Synthesis of graphene and MoS_2

2.2.1.1 Graphene

SL graphene was synthesized using the method recently reported by our group to produce single, uniform crystals of graphene with diameter larger than 300 μm.[25] A 2x2 cm^2 piece of polycrystalline copper foil is inserted into a 1 in. quartz tube furnace and heated to 1030 °C in the presence of H_2 (10 sccm) and argon (300 sccm) gases and held at these conditions for 2 h. For graphene growth, diluted CH_4 in argon (90 ppm) is introduced for 20 minutes while H_2 flow remains unchanged. The foil is then cooled to room temperature under H_2 and argon gas flow. The

graphene/copper foil is coated with PMMA and copper is then etched in 0.2 M ammonium persulfate (APS) solution. The floating graphene/PMMA is washed multiple times with deionized (DI) water in order to remove remaining residues. This PMMA/graphene stack is transferred onto a Si/SiO_2 wafer that is pre-cleaned in piranha solution (3:1 volume ratio of H_2SO_4:H_2O_2) and the PMMA layer is removed in acetone at 60 °C overnight.

2.2.1.2 MoS_2

A CVD method is employed with sulfur and molybdenum trioxide (MoO_3) as the growth precursors and sapphire as the substrate. The growth is carried out in the presence of argon flow at 50 sccm under ambient pressure. The substrate is placed facing down on top of the MoO_3 source at the center of the furnace, where the temperature is ramped from room temperature to 650 °C at a ramp rate of 25 °C min^{-1}. Sulfur is introduced to the system by evaporation using a heating jacket at 170 °C as soon as the furnace is turned on. When the furnace reaches 650 °C, the temperature is held constant for 10 minutes. Then, both the furnace and heating jacket are turned off and cooled down to room temperature. For the transfer, MoS_2 on sapphire is spin-coated with polystyrene (PS) and the PS/MoS_2 stack is isolated using simple lift-off in DI water, which does not require any etching process. The PS/MoS_2 film is washed several times with DI water to remove remaining residues and PS is removed by immersing in toluene solution.

2.2.2 Fabrication of FET devices

2.2.2.1 Graphene FET device

PMMA/graphene film is transferred onto pre-patterned gold electrodes and PMMA is removed in acetone at 60 °C. The collected large-area graphene film is patterned in a 50 μm x10 μm pattern using conventional photolithography and the excess graphene is removed by reactive ion etching process with O_2 plasma. Photoresist on patterned graphene is cleaned overnight in acetone at 60 °C.

Finally, 10 nm/100 nm in thickness of Cr/Au, respectively, is deposited on the back Si interface acting as a back-gate electrode.

2.2.2.2 MS/G FET device

After graphene FET is fabricated, PS/MoS_2 film is transferred onto the patterned graphene and air-dried for 1 h. The polystyrene layer is removed in toluene and the resulting device is annealed in 300 sccm Ar at 200 °C to remove remaining residues and also enhance the contact between graphene and MoS_2 layers. Finally, 10 nm/100 nm in thickness of Cr/Au, respectively, is deposited on the silicon interface acting as a back-gate electrode.

2.2.3 Electrochemical characterization

4-layer graphene is prepared by repeated stacking of PMMA-coated graphene onto SL graphene/copper. This method avoids PMMA contamination in the interlayer of multi-layer graphene, as only the top layer is coated with PMMA. For the MoS_2/4LG device, a layer of PS/MoS_2 is stacked onto the fourth graphene/copper layer and the PS is dissolved in toluene. Then, the PMMA/3LG is scooped on top. The pristine and doped PMMA/4LG are transferred onto glass. The PMMA layer is dissolved using acetone and a Cr/Au contact (10 nm/140 nm) is evaporated surrounding a circular graphene area of 0.13 cm^2. The Cr/Au contact is insulated with PMMA for the electrochemical measurement, to leave only graphene exposed to the electrolyte. The electrochemical measurement is performed with a CHI 660C electrochemical station. The impedance of the electrodes is measured at a relatively high concentration of 0.5 M KCl, to make diffusion capacitance negligible with respect to the total C_{EDL}. An AC voltage with a frequency of 10 kHz and a perturbation amplitude of 5 mV is swept from -0.8 to 0.6 V using a Ag/AgCl reference electrode (saturated KCl) and a Pt mesh counterelectrode. The impedance of the MoS_2/4LG device is measured before and after annealing at 200˚C in Ar atmosphere.

2.2.4 Theoretical modeling

Our calculations are based on first-principles density functional theory (DFT) using the projector augmented wave method and the Perdew-Burke-Ernzerhof (PBE) type generalized gradient approximation as implemented in the software package VASP.[26,27,28] More details are discussed in the Supplemental Information (SI). In brief, spin-orbit coupling (SOC) is included during self-consistent charge calculations. To improve the accuracy of the work-function calculations calculated from the PBE functional, we also carry out calculations using the Heyd-Scuseria-Ernzerhof (HSE) hybrid functional.[29] The HSE calculations incorporate 25% short-range Hartree-Fock exchange and the screening parameter is set to 0.2 Å. A Monkhorst-Pack scheme is adopted to integrate over the Brillouin zone with a converged k-mesh of $2 \times 8 \times 1$ for the surface and the heterostructure. A plane-wave basis cutoff of 550 eV is used. The atomic coordinates are optimized using the DFT-D2 dispersion correction.[30] All the relaxations are applied until all the interatomic forces are below 0.01 $eVÅ^{-1}$. For the calculations of the few-layer and monolayer structures with a vacuum distance of 20 Å is used to avoid interactions between the periodically repeated slabs. The MoS_2/graphene heterostructure is created using Cellmatch Method.[31] To handle the in-plane lattice mismatch of ~9% between graphene and MoS_2 unit cells, the graphene unit cell is repeated 5 times, while the MoS_2 unit cell is repeated 3 times. The layer-to-layer strain is further reduced to ~5% by rotating graphene supercell by -R30° while fixing the MoS_2 super cell.

2.2.5 Optical and spectrometric characterization

Optical images are taken by Hirox KH-7700 digital microscope and AFM images are taken by Assylum Research MFP-3D Atomic Force Microscope. Both Raman spectra and PL measurements are collected by Horiba LabRam using a green laser (λ = 532 nm) for excitation. A minimal power of 5 mW is used to avoid local heating and possible damage to the materials. Characteristics curves

of the FET devices are obtained by Keithley 2636 system by applying a constant $V_{source\text{-}drain}$ = 0.1 V while sweeping the back-gate voltage from -20 V to 120 V.

2.2.6 Gas sensing set-up and measurement

For stability of the devices in dry air and NO_2 detection, the flow rates of dry air and NO_2 are controlled by two mass flow controllers. The target concentration of NO_2 gas for detection is varied by changing the ratio of NO_2 and dry air's flow rates. The two gas streams are well-mixed in a mixer prior to being fed into the gas chamber.

For toluene detection, the set-up consists of an incoming carrier gas (dry air) which branches into two air streams. One stream is directed through a bubbler containing pure toluene solution in order to create a saturated toluene gas flow. This saturated toluene gas flow is then diluted and well-mixed with the other dry air gas stream in a mixer tube to desired concentrations. This resulting gas stream is fed into the gas chamber capped on the sensor for real-time detection.

For all gas detection measurements, a constant bias $V_{source\text{-}drain}$ = 0.1 V is applied. Both current and resistance are monitored by the aforementioned Keithley system.

2.3 Result and Discussion

Both SL graphene and SL MoS_2 were synthesized using CVD method, which is discussed in the experimental section, and then characterized using optical and electron microscopy, Raman spectrometry, atomic force microscope (AFM) and PL. Graphene was initially grown on polycrystalline copper substrate, according to our previous report, in a hexagonal crystal structure as shown in **Figure 2.1(a)** and then transferred onto SiO_2 via a metal etching process with the aid of flexible polymer layer.[25] The uniform color contrast in **Figure 2.1(b)** indicates that the graphene is single layer and residue-free after the transfer process. In addition, the absence of the D peak at 1260 cm^{-1} in the Raman spectra of our CVD graphene denotes there are no defects introduced

during both the growth and transfer processes.[32] The ratio of the G peak at 1570 cm^{-1} and 2D peak at 2650 cm^{-1}, $I_{2D}/I_G \approx 2$, confirms our CVD graphene is single layer and uniform across the film.[33]

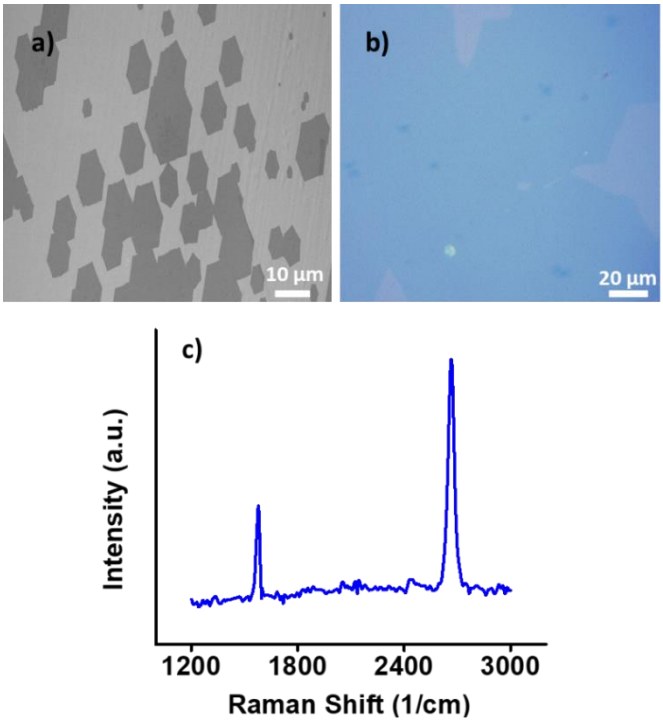

Figure 2.1. CVD graphene properties: (a) SEM image of CVD grown graphene on copper substrate (b) Optical image of graphene transferred onto SiO_2 substrate (c) Raman spectra of SL graphene.

On the other hand, MoS_2 was synthesized via CVD on two different substrates: sapphire and SiO_2. We observe that MoS_2 grows in a more continuous and uniform film on sapphire substrate than on SiO_2 substrate as seen in **Figure 2.2(a) and 2.2(b)**, respectively. For the device fabrication, we have used CVD-grown MoS_2 on sapphire which grows in more continuous film and comprises of mainly SL-MoS_2. The thickness of the MoS_2 film, which was initially synthesized on sapphire substrate and later transferred to SiO_2/Si substrate for device fabrication, is measured using AFM. The height profile between the two surfaces of SiO_2 substrate and MoS_2 film, shown in **Figure 2.2(c)** and **Figure 2.2(d)**, is about 8 Å, which corresponds to SL-MoS_2.[34] Raman spectra of CVD-MoS_2 in **Figure 2.3(a)** illustrates the two significant E_{2g} and A_{1g} peaks, corresponding to the in-plane and out-of-plane vibration modes at 388 cm^{-1} and 407 cm^{-1}, respectively. The distance of ~ 19-20 cm^{-1} between the two peaks is indicative of monolayer of CVD MoS_2 as reported elsewhere.[34] The band gap of a SL MoS_2 is determined using PL measured under excitation of green laser beam (λ_{ex}= 532 nm) at low power of 5 mW to avoid local heating. The PL spectra in **Figure**

2.3(b) shows a sharp peak at 675-680 nm of energy, which corresponds to direct band gap of ~1.87 eV. This value agrees with the band gap of SL MoS_2 that has been reported previously.[6]

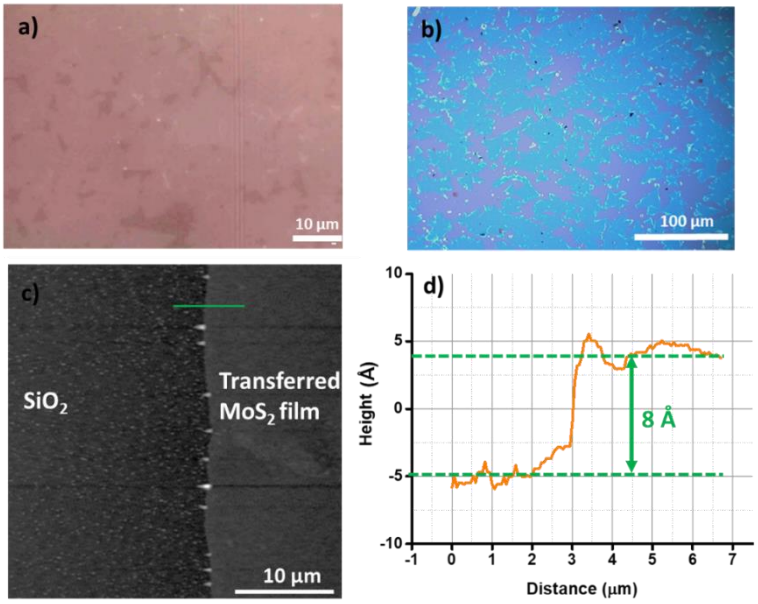

Figure 2.2. CVD MoS_2 properties: (a) As-grown CVD MoS_2 on sapphire. (b) As-grown CVD MoS_2 on Si/SiO_2 substrate. (c) AFM Image of MoS_2 film (d) Height profile of MoS_2 film.

After both individual materials were synthesized, the heterostructure was then fabricated by capping graphene with MoS_2 through a physical transfer method, followed by annealing to promote the contact between two materials. Raman spectra were recorded to ensure the properties of both materials were well-preserved after the transfer process. We also observed insignificant shift in E_{2g} and A_{1g} peaks between the SL MoS_2 and MoS_2/Graphene heterostructure (**Appendix (Appx.) A2**) which is an indication of contamination free interface [35]. While two E_{2g} and A_{1g} peaks of MoS_2 remain unchanged, a shift in G and 2D peaks of graphene is observed as seen in **Figure 2.4(a)**. Unlike a minor shift in the 2D peak, the noticeable redshift, i.e. shift to the right, in G peak confirms the doping of graphene layer due to its interaction with the SL MoS_2 layer, consistent with earlier results.[36,37,38] On the other hand, PL measurement of MoS_2 in the heterostructure, as seen in **Figure 2.4(b),** finds a significant quench of over 50% in intensity when compared to SL MoS_2. This

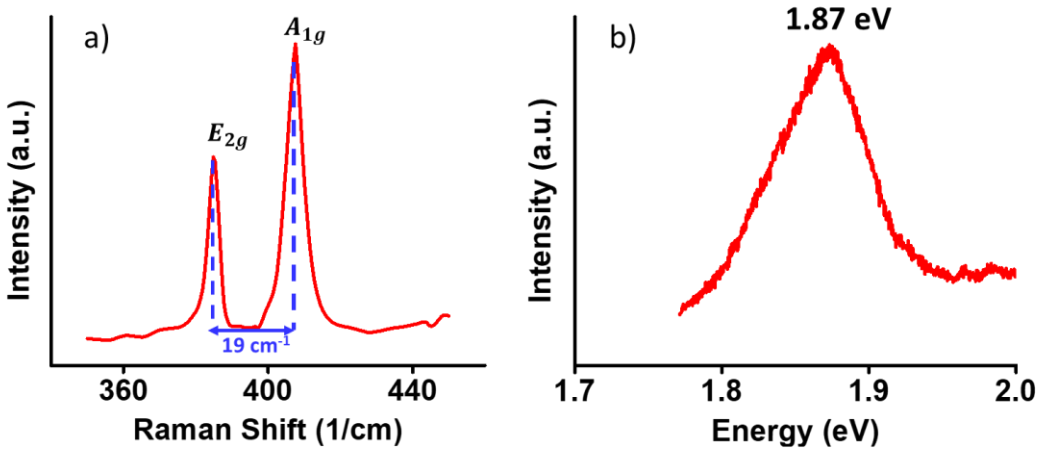

Figure 2.3. Raman spectra (a) and PL spectra (b) of SL MoS_2.

demonstrates a strong interaction between graphene and MoS_2 layers and is usually ascribed to charge transfer processes.[15,22,35]

For further elucidation of the doping effect due to charge transfer, the electronic properties of back-gated (BG) FETs fabricated with these materials were investigated. The resulting FET transfer curve was plotted in **Figure 2.5**. The graphene FET shows V_{CNP} at 85 V measured in atmosphere at room temperature, which is typical for a CVD grown graphene.[39,40] This high p-doping of graphene is commonly observed after a photolithography process of patterning involving the use

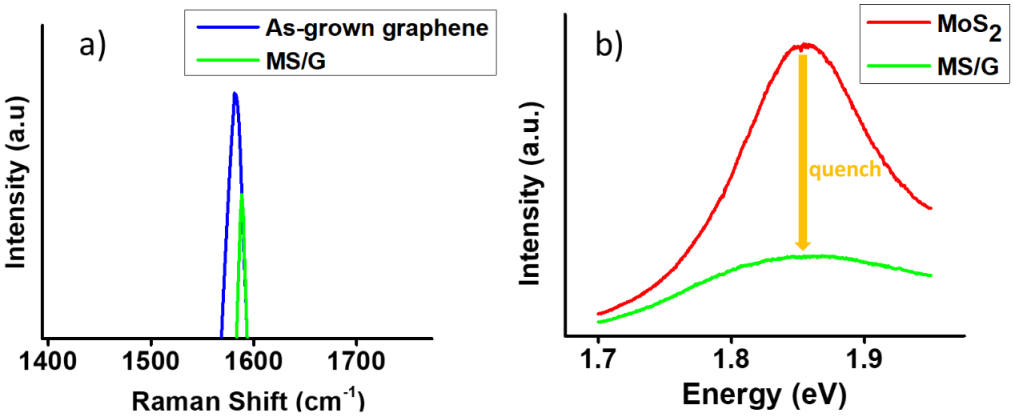

Figure 2.4. Raman shift observed at G peak (a) and PL intensity quench (b) in MS/G.

of O_2 plasma and exposure to metal etching solution such as ammonium persulfate (APS) and other adsorbents such as water and oxygen from the atmosphere.[41,42] Even though CVD-graphene is an ambipolar material, the significant difference between the two slopes of the right arm (related to electron concentration) and left arm (related to hole concentration) of the graphene FET's transfer curve indicates holes are the majority carriers in our CVD-graphene based FETs. However, when graphene is fully covered by MoS_2 the V_{CNP} is found at V_{BG} = 50 V indicating that graphene capped with MoS_2 becomes less p-doped (i.e more n-doped), due to the transfer of electrons from MoS_2 to graphene. In addition, the electron-to-hole ratio in the heterostructure increases as confirmed by the gain in the slope of the transfer curve's right arm.

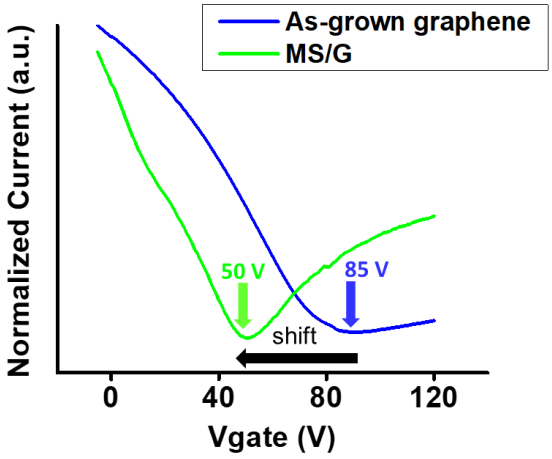

Figure 2.5. Transfer curve of as- grown graphene FET and MS/G FET.

In order to understand the fundamentals of doping and charge transport phenomena, the electronic structure and band alignment of the heterostructure is modeled as seen in **Figure 2.6** and **Figure 2.7**. The MS/G supercell is created by

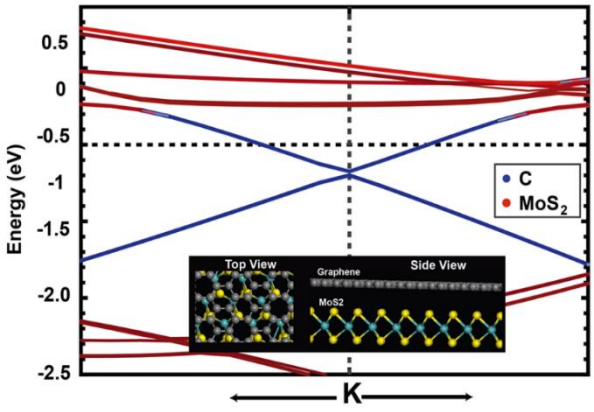

Figure 2.6. Band structure of MoS_2/graphene heterostructure. Inset illustrates graphene-MoS_2 model used in our simulation.

straining the graphene layer. The detail on model design and method used is described in the method section. The site-projected band structure is shown in **Figure 2.6**. Due to the in-built strain and charge transfer, the Fermi-level shifted above the CNP or Dirac point by n-doping the graphene system, as compared to pure SL graphene. In addition, the bi-axial strains also contribute to the band gap opening in the order of few meV at the Dirac cone of graphene. The origin of the bandgap opening is further confirmed by performing separate band structure calculation for 5% strained graphene layer. The work-functions, which is defined as the energy difference between the Fermi energy and the vacuum levels relative to their vacuum levels, of SL graphene and MS/G heterostructure are illustrated in **Figure 2.7**. Quantitatively, the work-functions of SL graphene and MS/G heterostructure are 4.487 eV and 4.390 eV, respectively. The work-function difference of 97 meV between the SL graphene and MS/G heterostructure is primarily due to the shift in the Fermi-level resulting from the charge transfer from the MoS_2 layer to graphene layer. This computed value of 97 meV is similar to the change in work function (i.e. shift of Fermi level) measured via UPS method of 100 meV, which is presented in the subsequent section. The small difference may be resulted by variation in work functions of theoretical and as-prepared graphene, namely 4.487 eV and 5.2 eV. The observed in-built Schottky barrier heights (SBH) of the MS/G heterostructure is 127 meV, which is consistent with previous studies.[43,44,45]

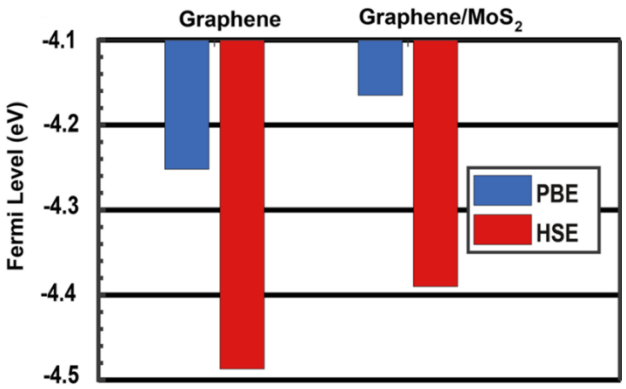

Figure 2.7. Comparison of work-function between a SL graphene and MoS_2/graphene heterostructure model used in our simulation.

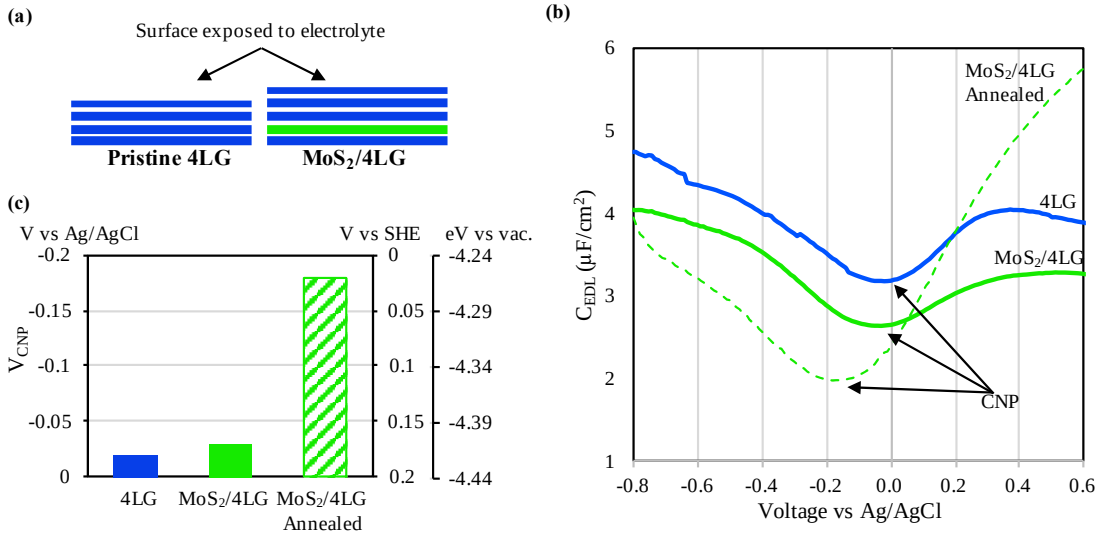

Figure 2.8. Electrical double-layer capacitance (C_{EDL}) of 4LG and MoS_2/4LG electrodes. (a) Schematic of 4LG and MoS_2/4LG heterostructure electrodes studied by electrochemical impedance. (b) C_{EDL} plotted vs the electrode potential measured against Ag/AgCl reference electrode calculated form Equation [1]. (c) Potential at charge neutrality point (V_{cnp}) for each electrode.

To further explore the effect of MoS_2 in the electronic properties of graphene, we obtained the electrochemical impedance of the pristine and heterostructure electrodes with the configuration shown in **Figure 2.8(a)**. The impedance is measured at a frequency (*f*) of 10 kHz while sweeping the potential of the electrode. The electrical double-layer capacitance (C_{EDL}), which can be approximated to the quantum capacitance in graphene, was calculated according to **Equation 1**, where Z'' is the imaginary part of the complex impedance.

$$C_{EDL} = -\frac{1}{2\pi f Z''} \qquad \textbf{Equation (1)}$$

The area-normalized $C_{EDL}$with respect to the electrode potential vs. Ag/AgCl is shown in **Figure 2.8(b)**. The C_{EDL} vs. V curves are all concave-shaped with the capacitance suppressed near the CNP, with minimum values between 2-3.5 μFcm^{-2}, in agreement to previous reports for four-layer graphene (4LG).[46] The low C_{EDL} obtained is attributed to the low density of states near or at the Fermi level.[47] The low defect density of our graphene results in C_{EDL} similar to the basal plane

of HOPG.[48] The CNP is summarized for each electrode in **Figure 2.8(c)**, with a value of -0.02 V for pristine 4LG, close to the values of -0.05 V for 4LG or -0.1 V reported by electrochemical methods for graphene nanoplatelets.[34,49] Mostly no shift is observed for the non-annealed stack of MoS_2/4LG with CNP at -0.03 V, however, after annealing there is a significant shift to -0.18 V. The MoS_2 layer induces a net CNP or Fermi level upshift of 0.16 eV, attributed to doping of the graphene sheet due to electron transfer from MoS_2. Simple physical stacking of MoS_2 as an interlayer does not change the electrochemical behavior of 4LG, annealing is necessary for hybridization of the electronic states of both materials. Annealing removes adsorbed molecules at the interface like O_2 and H_2O, which reduces the interfacial distance between graphene and MoS_2, increasing the electric field that cause charge transfer from one material to the other, i.e. doping.[50,51]

The n-doping effect of combining MoS_2 and graphene is explained by band-alignment diagram in **Figure 2.9**. All the parameters used in this diagram are extracted from experiment (**Appx. A1**). CVD-MoS_2 is well-known as an n-type material due to its sulfur vacancies and other lattice impurities.[52-44] On the other hand, CVD-graphene as a highly p-doped material has a Fermi level found closer to the valance band (VB) energy, which results in a higher work-function than that of

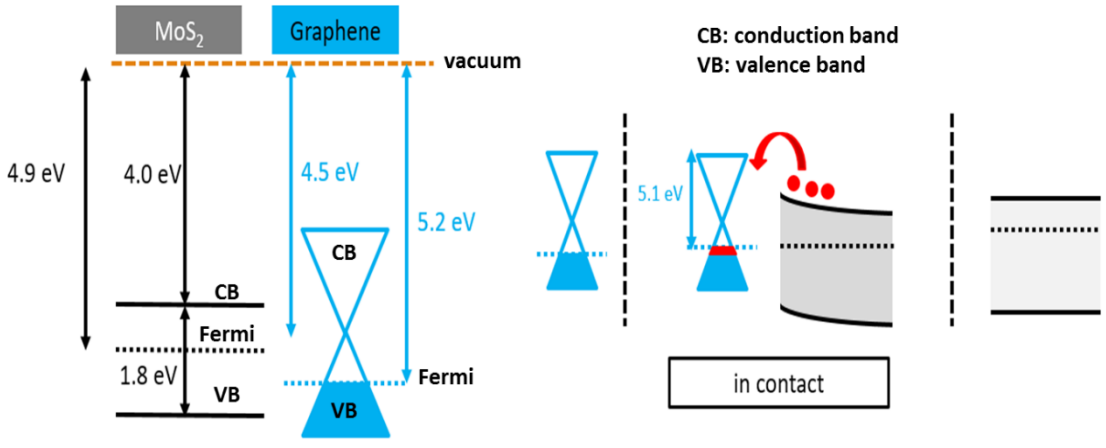

Figure 2.9. Band diagram of graphene, MoS_2 and MS/G (in contact).

n-doped MoS_2. In fact, the work-function of graphene measured by UPS is 5.2 eV, which is higher than one of MoS_2 at 4.9 eV. These values are consistent with first principle calculated values for the single layer graphene and MoS_2. As the two materials come in contact forming heterojunction, the difference in their work-function triggers electron transfer from n-type MoS_2 to highly p-doped graphene, and those electrons are then combined with excess holes in graphene. Such mechanism is consistent with the observed reduction in hole concentration from electrochemical measurement of capacitance. As a result, the Fermi level of graphene in the heterostructure shifted up (i.e., less p-doped) resulting in 0.1 eV work-function reduction, as compared to as-grown SL graphene. The CNP shift of +0.1 eV measured with UPS is also close to the value obtained from electrochemical measurements (+0.16 eV) and first principle calculations (+0.097 eV). This is also consistent with the negative shift of V_{CNP} in MS/G FETs in field-effect transfer curve observed in **Figure 2.5**. The reduction in work-function due to the shift in CNP point could be the source of PL intensity quenching observed in MS/G heterostructure, as compared to SL MoS_2. Due to the electron transfer, the number of electrons in MoS_2 reduces, which causes the decrease in the number of electron-hole combination during the PL excitation. Similar n-doping effect is also observed in heterostructure of n-type WS_2 and graphene, and expected to further enhance under illumination, which is not discussed in scope of this paper.[22,23] Thus, this finding offers a new method of n-doping

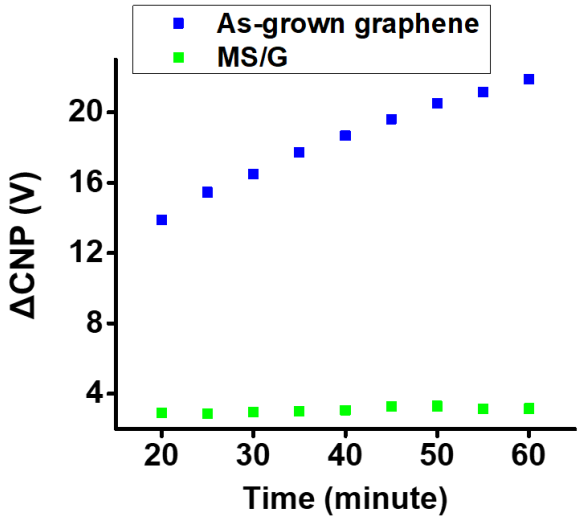

Figure 2.10. ΔCNP of graphene and MS/G FET devices in dry air.

graphene for p-n junction transistor applications without introducing signification defects via conventional doping methods which requires chemical enhancement.[55,56]

Utilizing the FET design with MoS_2, graphene and heterostructure as channel materials, we then analyzed the feasibility of these devices as sensors by exposing them to different gaseous analytes. More detail of the gas sensing system is described in the experimental section. Firstly, the stability of the heterostructure device was examined in the presence of dry air. The initial V_{CNP0} was measured before the dry air was introduced to the system (t = 0 minute). After the devices stabilized in the continuous air flow for 20 minutes, the V_{CNP} of the devices were taken every subsequent 5 minutes. The shift in CNP (ΔCNP) is defined as $\Delta CNP = V_{CNP} - V_{CNP0}$. Therefore, ΔCNP at t = 0 minute, by definition, equals 0 V, which is not explicitly plotted in **Figure 2.10**. After the devices stabilize, ΔCNP of graphene FET is measured at 14 V while one of the MS/G FET changes by 3 V. Oxygen, as oxidizing gas molecules, in the dry air contributes to the observed ΔCNP.[57] For the first 20 minutes, these changes of 3 V vs. 14 V indicates that MS/G is more stable than graphene. In addition, 40 minutes after the devices stabilize, the MS/G device shows a negligible change of 0.3 V of ΔCNP while ΔCNP of graphene FET increases by an additional 8 V (from 14 V to 22 V). Due to its atomic thickness, SL graphene possesses an exceptionally high surface area-to-volume ratio, deeming its surface highly favorable for gas molecules to adsorb.[57] On the other hand, due to the termination of the existing lone pair of electrons of the sulfur on the surface, MoS_2 behaves more passively and hence its interaction with the ambient environment is negligible. This explains why the MS/G device becomes more stable when graphene is capped with MoS_2. This phenomenon is also seen in other studies where MoS_2 FETs are highly stable for 24 h in wet conditions and at different pH conditions.[58] As a result, MoS_2 in such a heterostructure acts as a protective layer on graphene to minimize the atmospheric interference, which can lead to inaccuracies in gas sensing.

Taking advantage of the stability of the heterostructure, we investigated the sensing properties using CNP shift as an alternative to the traditional transient response. FET devices using MS/G as a conducting channel were exposed to different concentrations of NO_2 in dry air. The result is shown in **Figure 2.11**. In this experiment, ΔCNP is defined the same as above. V_{CNP0} was first taken after 20 minutes of device stabilization in dry air. Each concentration of NO_2 was introduced to the gas chamber for 20 minutes to achieve saturation, and measurement of V_{CNP} was then recorded. From the previous FET transfer characteristics curves, MS/G FETs shows p-type behavior at V_{BG} = 0 V. Upon binding to typical electron-withdrawing gas molecules (NO_2), electrons are withdrawn from the conducting material and hence causes the increase in hole concentration of the materials, which in turn enhances the p-type doping effect. As a result, the CNP of the device then shifts to the positive direction of V_{BG}. As the concentration of NO_2 increases, more holes accumulate in the material and subsequently greater p-doping effect is observed as represented by the upshifting of CNP. It is also noticed in **Figure 2.10** that the shift of CNP in MS/G during the exposure to NO_2 at our lowest tested concentration of 200 ppm, is 8 times higher than in the control experiment in presence of pure dry air. This ensures the shift of CNP is due to the interaction between the analyte gas NO_2 and the sensing materials.

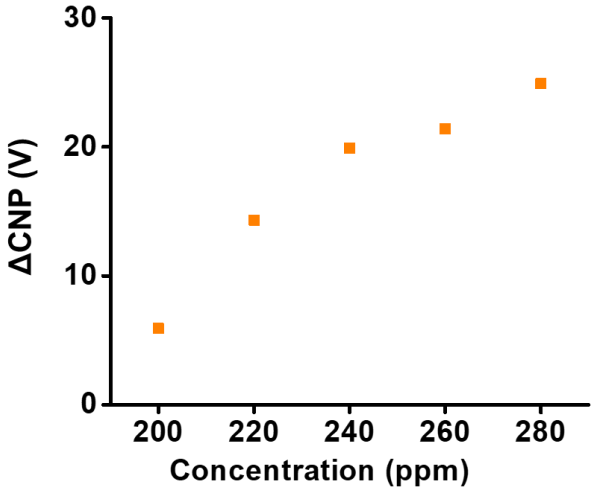

Figure 2.11. ΔCNP of MS/G FET devices in presence of NO_2.

We also investigated the dynamic response of the MS/G heterostructure-based devices with volatile organic compounds. Toluene is chosen as a candidate analyte for our experiment because it has been widely used as a solvent for paint, glue, rubber or varnish industries, etc. However, exposure to high concentration of toluene at thousands of ppm may cause extreme damage to human health.[59] In addition, its higher binding affinity to MoS_2 than to graphene makes toluene a perfect candidate for comparison between MS/G, MoS_2 and graphene.[39,41,60] **Figure 2.12** shows sensing responses, current output, of FET devices with the three materials as sensing channel at varying concentrations of toluene vapors. As expected, due to a low binding affinity of toluene to graphene, the graphene-based FET device shows no response at investigated concentrations (**Figure 2.12(b)**). However, the MoS_2-based FET device, despite having a higher binding affinity

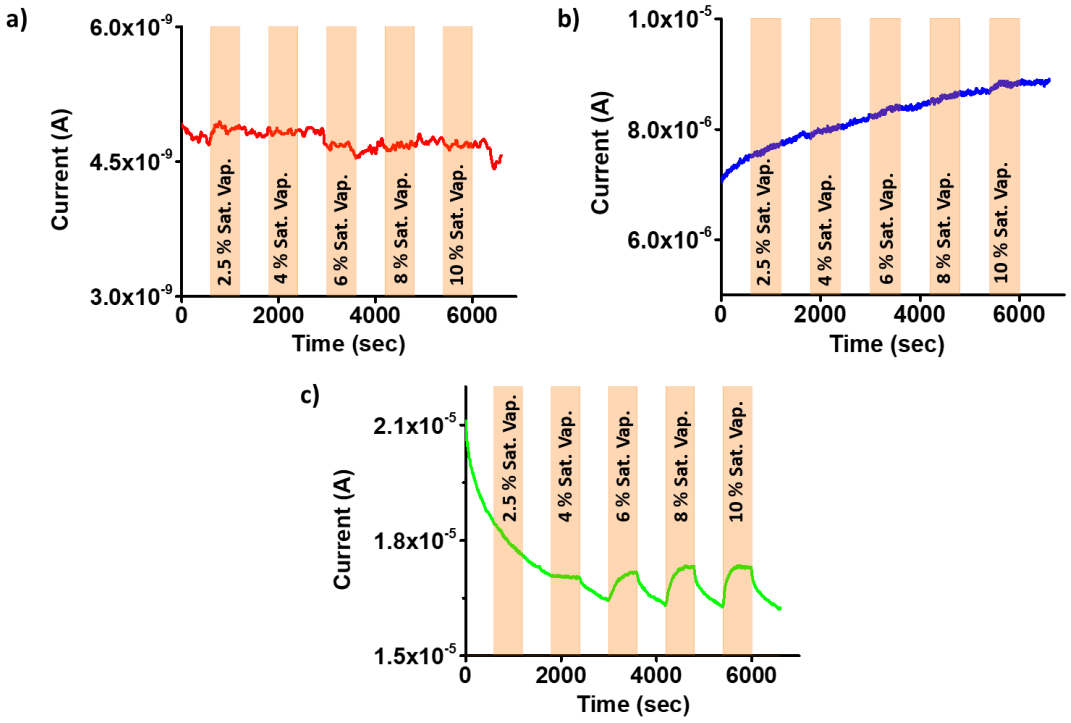

Figure 2.12. Dynamic response of (a) MoS_2, (b) graphene and (c) MS/G FET devices in presence of toluene at $V_{source\text{-}drain}$ = 0.1 V and V_{bg} = 0

to toluene, still experiences an extremely low signal-to-noise ratio due to a high contact resistance and low electrical mobility (**Figure 2.12(a))**. On the other hand, the MS/G sensing channel device exhibited a high response, approximately 12.5% change in current within 10 minutes at the concentration of 10% of saturated vapor at room temperature (**Figure 2.12(c))**. The response is ascribed to an increase in concentrations of holes in the p-type MS/G FET device (at $V_{bg} = 0$ V) upon binding of electron-withdrawing toluene gas molecules to the sensing channel. This suggests a superior application of the MS/G material over the constituent materials due to the increased stability, sensitivity and signal-to-noise ratio.

2.4 Conclusion

In this study, the n-doping effect was investigated in a vertically stacked heterostructure of MoS_2 and graphene. The FET characteristics transfer curve confirms the highly p-doped graphene attributed to both the CVD process of synthesis and the device fabrication process. This graphene becomes less p-doped in its heterostructure as observed by a shift of CNP from a high back-gate voltage of 85 V to a smaller value of 50 V. The electron transfer from MoS_2 to graphene in the annealed heterostructure is further confirmed by the shift of the graphene Raman peaks, the PL quenching of the MoS_2, a shift of CNP in C_{EDL} vs V curve measured in electrochemical setup, and the reduction in work-function measured by UPS and predicted by first principle simulations. In addition, the top MoS_2 layer in the heterostructure performs as a passive layer on graphene, which successfully minimizes the electrical drifting due to the strong interaction between the sensing channel and the ambient atmosphere. Hence, this new method of gas sensing using a shift of CNP is novel and efficient, as compared to traditional amperometric measurement. Finally, the study of the MoS_2/graphene heterostructure as a channel material for sensing applications to the volatile gas molecules, such as toluene, suggests it as a novel material with high sensitivity and stability for gas detection.

2.5 References

(1) Ajayan, P.; Kim, P.; Banerjee, K. Two-dimensional van der Waals Materials, *Physics Today* **2016**, *69*, 38-44.

(2) Novoselov, K. S.; Geim, A. K.; Morozov, S. V.; Jiang, D.; Zhang, Y.; Dubonos, S. V.; Grigorieva, I. V.; Firsov, A. A. Electric Field Effect in Atomically Thin Carbon Films. *Science* **2004**, *306*, 666-668.

(3) Meric, I.; Han, M. Y.; Young, A. F.; Ozyilmaz, B.; Kim, P.; Shepard, K. L. Current Saturation in Zero-Bandgap, Top-Gated Graphene Field-Effect Transistors. *Nat. Nanotechnol.* **2008**, *3*, 654-659.

(4) Xu, M.; Liang, T.; Shi, M.; Chen, H. Graphene-Like Two-Dimensional Materials. *Chem. Rev.* **2013**, *113*, 3766-3798.

(5) Lee, C.; Yan, H.; Brus, L. E.; Heinz, T. F.; Hone, J.; Ryu, S. Anomalous Lattice Vibrations of Single- and Few-Layer MoS_2. *ACS Nano* **2010**, *4*, 2695-2700.

(6) Mak, K. F. ; Lee, C. ; Hone, J. ; Shan, J. ; Heinz, T. F. Atomically Thin MoS_2 : A New Direct-Gap Semiconductor. *Phys. Rev. Lett.* **2010**, *105*, 136805.

(7) Radisavljevic, B.; Radenovic, A.; Brivio, J.; Giacometti, V.; Kis, A. Single-Layer MoS_2 Transistors. *Nat. Nanotechnol.* **2011**, *6*, 147-150.

(8) Novoselov, K. S.; Jiang, D.; Schedin, F.; Booth, T. J.; Khotkevich, V. V.; Morozov, S. V.; Geim, A. K. Two-Dimensional Atomic Crystals. *Proc. Natl. Acad. Sci. U. S. A.* **2005**, *102*, 10451-10453.

(9) Kaushik, N.; Nipane, A.; Basheer, F.; Dubey, S.; Grover, S.; Deshmukh, M. M.; Lodha, S. Schottky Barrier Heights for Au and Pd Contacts to MoS_2. *Appl. Phys. Lett.* **2014**, *105*, 113505.

(10) Yu, Y. J.; Zhao, Y.; Ryu, R.; Brus, L. E.; Kim, K. S.; Kim, P. Tuning the Graphene Work Function by Electric Field Effect. *Nano Lett.* **2009**, *9*, 3430-3434.

(11) Lee, C. H.; Lee, G. H.; van der Zande, A. M.; Chen, W.; Li, Y.; Han, M.; Cui, X.; Arefe, G.; Nuckolls, C.; Heinz, T. F.; Guo, J.; Hone, J.; Kim, P. Atomically Thin P–n Junctions with van der Waals Heterointerfaces. *Nat. Nanotechnol.* **2014**, *9*, 676-681.

(12) Rathi, S.; Lee, I.; Lim, D.; Wang, J.; Ochiai, Y.; Aoki, N.; Watanabe, K.; Taniguchi, T.; Lee, G. H.; Yu, Y. J.; Kim, P.; Kim, G. H. Tunable Electrical and Optical Characteristics in Monolayer Graphene and Few-Layer MoS_2 Heterostructure Devices. *Nano Lett.* **2015**, *15*, 5017-5024.

(13) Lin, Y. C.; Gosh, R. K.; Addou, R.; Lu, N.; Eichfeld, S. M.; Zhu, H.; Li, M. Y.; Peng, X.; Kim, M. J.; Li, L. J.; Wallace, R. M.; Datta, S.; Robinson, J. A. Atomically Thin Resonant Tunnel Diodes Built from Synthetic van der Waals Heterostructures. *Nat. Commun.* **2015**, *6*, 7311.

(14) Lin, Y. C.; Lu, N.; Lopez, N. P.; Li, J.; Lin, Z.; Peng, X.; Lee, C. H.; Sun, C.; Calderin, L. Browning, P. N.; Bresnehan, M. S.; Kim, M. J.; Mayer, T. S.; Terrones, M.; Robinson, J. A. Direct Synthesis of van der Waals Solids. *ACS Nano* **2014**, *8*, 3715-3723.

(15) Shi, Y.; Zhou, W.; Lu, A. Y.; Fang, W.; Lee, Y. H.; Hsu, A. L.; Kim, S. M.; Kim, K. K.; Yang, H. Y.; Li, L. J.; Idrobo, J. C.; Kong, J. Van der Waals Epitaxy of MoS_2 Layers Using Graphene As Growth Templates. *Nano Lett.* **2012**, *12*, 2784-2791.

(16) Yang, W.; Chen, G.; Shi, Z.; Liu, C. C.; Zhang, L.; Xie, G.; Cheng, M.; Wang, D.; Yang, R.; Shi, D.; Watanabe, K.; Taniguchi, T.; Yao, Y.; Zhang, Y.; Zhang, G. Epitaxial Growth of Single-Domain Graphene on Hexagonal Boron Nitride. *Nat. Mater.* **2013**, *12*, 792-797.

(17) Gong, Y.; Lin, J.; Wang, X.; Shi, G.; Lei, S.; Lin, Z.; Zou, X.; Ye, G.; Vajtai, R.; Yakobson, B. I.; Terrones, H.; Terrones, M.; Tay, B. K.; Lou, J.; Pantelides, S. T.; Liu, Z.; Zhou, W.; Ajayan, P. M. Vertical and In-plane Heterostructures from WS_2/MoS_2 Monolayers. *Nat. Mater.* **2014**, *13*, 1135-1142.

(18) Levendorf, M. P.; Kim, C. J.; Brown, L.; Huang, P. Y.; Havener, R. W.; Muller, D. A.; Park, J. Graphene and Boron Nitride Lateral Heterostructures for Atomically Thin Circuitry. *Nature* **2012**, *488*, 627-632.

(19) Perkins, F. K.; Friedman, A. L.; Cobas, E.; Campbell, P. M.; Jernigan, G. G.; Jonker, B. T. Chemical Vapor Sensing with Monolayer MoS_2. *Nano Lett.* **2013**, *13*, 668-673.

(20) Schedin, F.; Geim, A. K.; Morozov, S. V.; Hill, E. W.; Blake, P.; Katsnelson, M. I.; Novoselov, K. S. Detection of Individual Gas Molecules Adsorbed on Graphene. *Nat. Mater.* 2007, *6*, 652-655.

(21) Kong, J.; Franklin, N. R.; Zhou, C.; Chapline, M. G.; Peng, S.; Cho, K.; Dai, H. Nanotube Molecular Wires as Chemical Sensors. *Science* **2000**, *287*, 622-655.

(22) Tan, H.; Fan, Y.; Rong, Y.; Porter, B.; Lau, C. S.; Zhou, Y.; He, Z.; Wang, S.; Bhaskaran, H.; Warner, J. H. Doping Graphene Transistors Using Vertical Stacked Monolayer WS_2 Heterostructures Grown by Chemical Vapor Deposition. *ACS Appl. Mater. Interfaces* **2016**, *8*, 1644-1652.

(23) Huo, N.; Wei, Z.; Meng, X.; Kang, J.; Wu, F.; Li, S. S.; Wei, S. H.; Li, J. Interlayer Coupling and Optoelectronic Properties of Ultrathin Two-Dimensional Heterostructures Based on Graphene, MoS_2 and WS_2. *J. Mater. Chem. C* **2015**, *3*, 5467-5473.

(24) De Fazio, D.; Goykhman, I.; Yoon, D.; Bruna, M.; Eiden, A.; Milana, S.; Sassi, U.; Barbone, M.; Dumcenco, D.; Marinov, K.; Kis, A.; Ferrari, A. C. High Responsivity, Large-Area Graphene/MoS_2 Flexible Photodetectors. *ACS Nano* **2016**, *10*, 8252-8262.

(25) Malekpour, H.; Ramnani, P.; Srinivasan, S.; Balasubramanian, G.; Nika, D. L.; Mulchandani, A.; Roger, K.; Lake, R. K.; Balandin, A. A. Thermal Conductivity of Graphene with Defects Induced by Electron Beam Irridiation. *Nanoscale* **2016**, *8*, 14608-14616.

(26) Perdew, J. P.; Burke, K.; Ernzerhof, M. Generalized Gradient Approximation Made Simple. *Phys. Rev. Lett.* **1996,** *77*, 3865-3868.

(27) Ernzerhof, M.; Scuseria, G. Assessment of the Perdew-Burke-Ernzerhof Exchange-Correlation Functional. *J. Chem. Phys.* **1999**, *110*, 5029.

(28) Kresse, G.; Hafner, J. Ab Initio Molecular Dynamics for Liquid Metals. *Phys. Rev. B* **1993**, *47*, 558.

(29) Heyd, J.; Scuseria, G. E.; Ernzerhof, M. Hybrid Functionals Based on a Screened Coulomb Potential. *J. Chem. Phys.* **2003**, *118*, 8207.

(30) Grimme, S. Semiempirical GGA-Type Density Functional Constructed with a Long-Range Dispersion Correction. *J. Comput. Chem.* **2006**, *27*, 1787-1799.

(31) Lazic, P. CellMatch: Combining Two Unit Cells into a Common Supercell with Minimal Strain. *Comput. Phys. Comm.* **2015**, *197*, 324-334.

(32) Beams, R.; Cançado, L. G.; Novotny, L. Raman Characterization of Defects and Dopants in Graphene. *J. Phys. Condens. Matter* **2015**, *27*, 083002.

(33) Ni, Z.; Wang, Y.; Yu, T.; Shen, Z. Raman Spectroscopy and Imaging of Graphene. *Nano Res.* **2008**, *1*, 273-291.

(34) Zhan, Y.; Liu, Z.; Najmaei, S.; Ajayan, P. M.; Lou, J. Large-Area Vapor-Phase Growth and Characterization of MoS_2 Atomic Layers on A SiO_2 Substrate. *Small* **2012**, *8*, 966-971.

(35) Liang, L.; Zhang, J.; Sumpter B. G.; Tan, Q. H.; Tan P. H.; Meunier, V. Low-Frequency Shear and Layer-Breathing Modes in Raman Scattering of Two-Dimensional Materials. *ACS Nano*. **2017**, *11*, 11777-11802.

(36) Li, Y. Intrinsic Doping Dependence of Raman 2D Mode in Graphene: Signatures of Electron-Electron Interaction. In: Probing the Response of Two-Dimensional Crystals by Optical Spectroscopy (pp. 9-18). Springer Theses (Recognizing Outstanding Ph.D. Research). Springer, Cham.

(37) Stampfer, C.; Wirtz, L.; Jungen, A.; Graf, D.; Molitor, F.; Hierold, C.; Ensslin, K. Raman Imaging of Doping Domains in Graphene on SiO_2. *Appl. Phys. Lett.* 2007, *91*, 241907.

(38) Pandey, T.; Nayak, A. P.; Moran, S. T.; Kim, J. S.; Li, L. J.; Lin, J. F.; Akinwande, D.; Singh, A. K. Pressure-Induced Charge Transfer Doping of Monolayer Graphene/MoS_2 Heterostructure. *Small* **2016**, *12*, 4063-4069.

(39) Peng, S.; Jin, Z.; Ma, P.; Yu, G. H.; Shi, J. Y.; Zhang, D. Y.; Chen, J.; Liu, X. Y.; Ye, T. C. Heavily P-Type Doped Chemical Vapor Deposition Graphene Field-Effect Transistor with Current Saturation. *Appl. Phys. Lett.* **2013**, *103*, 223505.

(40) Goniszewski, S.; Adabi, M.; Shaforost, O.; Hanham, S. M.; Hao, L.; Klein, N. Correlation of P-Doping in CVD Graphene with Substrate Surface Charges. *Sci. Rep.* **2016**, *6*, 22858.

(41) Kim, K.; Park, H. H. J.; Woo, B. C.; Kim, K. J.; Ki, G. T.; Yun, W. S. Electric Property Evolution of Structurally Defected Multilayer Graphene. *Nano Lett.* **2008**, *8*, 3092-3096.

(42) Kantar, B. B.; öZtüRk, M.; çEtin, H. The Effects of Lithographic Residues and Humidity on Graphene Field Effect Devices. *Bull. of Mater. Sci.* **2017**, *40*, 239-245.

(43) Yu, L.; Lee, Y. H.; Ling, X.; Santos, E. J. G.; Shin, Y. C.; Lin, Y.; Dubey, M.; Kaxiras, E.; Kong, J.; Wang, H.; Palacios, T. Graphene/MoS_2 Hybrid Technology for Large-Scale Two-Dimensional Electronics. *Nano Lett.* **2014**, *14*, 3055-3063.

(44) Yoon, J.; Park, W.; Bae, G. Y.; Kim, Y.; Jang, H. S.; Hyun, Y.; Lim, S. K.; Kahng, Y. H.; Hong, W. K.; Lee, B. H.; Ko, H. C. Highly Flexible and Transparent Multilayer MoS_2 Transistors with Graphene Electrodes. *Small* **2013**, *9*, 3295-3300.

(45) Yu, W. J.; Li, Z.; Zhou, H.; Chen, Y.; Wang, Y.; Huang, Y.; Duan, X. Vertically Stacked Multi-Heterostructures of Layered Materials for Logic Transistors and Complementary Inverters. *Nat. Mater.* **2013**, *12*, 246-252.

(46) Ji, H.; Zhao, X.; Qiao, Z.; Jung, J.; Zhu, J.; Lu, Y.; Zhang, L. L.; MacDonald, A. H.; Ruoff, R. S. Capacitance of Carbon-Based Electrical Double-Layer Capacitors. *Nat. Commun.* **2014**, *5*, 3317.

(47) Pope, M. A.; Aksay, I. A. Four-Fold Increase in the Instrinsic Capacitance of Graphene through Functionalization and Lattic Disorder. *J. Phys. Chem. C* **2015**, *119*, 20369-20378.

(48) Gerischer, H.; McIntyre R.; Scherson, D.; Storck, W. Density of the Electronic States of Graphite: Derivation from Differential Capacitance Measurements. *J. Phys. Chem.* **1987**, *91*, 1930-1935.

(49) Kim, J. H.; Lee, J.; Hwang, C. C.; Lee, C.; Park, J. Y. Work Function Variation of MoS_2 Atomic Layers Grown with Chemical Vapor Deposition: The Effects of Thickness and The Adsorption of Water/Oxygen Molecules. *Appl. Phys. Lett.* **2015**, *106*, 251606.

(50) Janicki, L.; Kunert, G.; Sawicki, M.; Piskorska-Hommel, E.; Gas, K.; Jakiela, R.; Hommel, D.; Kudrawiec, R. Fermi Level and Bands Offsets Determination in Insulating (Ga,Mn)N/GaN Structures. *Sci. Rep.* **2017**, *7*, 41877.

(51) Poon, J.; Batchelor-McAuley, C.; Tschulik, K.; Compton, R. G. Single Graphene Nanoplatelets: Capacitance, Potential of Zero Charge and Diffusion Coefficient. *Chem. Sci.* **2015**, *6*, 2869-2876.

(52) Tong, X.; Ashalley, E.; Lin, F.; Li, H.; Wang, Z. M. Advances in MoS_2-Based Field Effect Transistors (FETs). *Nano-Micro Lett.* 2015, *7*, 203-218.

(53) Kang, J.; Liu, W.; Banerjee, K. High-Performance MoS_2 Transistors with Low-Resistance Molybdenum Contacts. *Appl. Phys. Lett.* **2014**, *104*, 093106.

(54) Namgung, S. D.; Yang, S.; Park, K.; Cho, A. J.; Kim, H.; Kwon, J. Y. Influence of Post-Annealing on the Off Current of MoS_2 Field-Effect Transistors. *Nanoscale Res. Lett.* **2015**, *10*, 1.

(55) Brenner, K.; Murali, R. Single Step, Complementary Doping of Graphene. *Appl. Phys. Lett.* **2010**, *96*, 063104.

(56) Xiang, D.; Han, C.; Wu, J.; Zhong, S.; Liu, Y.; Lin, J.; Zhang, X. A.;. Hu, W. P; Ozyilmaz, B.; Castro Neto, A. H.; Wee, A. T. S.; Chen, W. Surface Transfer Doping Induced Effective Modulation on Ambipolar Characteristics of Few-Layer Black Phosphorus. *Nat. Commun.* **2015**, *6*, 6485.

(57) Kong, L.; Enders, A.; Rahman, T. S.; Dowben, P. A. Molecular Adsorption on Graphene. *J. Phys. Condens. Matter* **2014**, *26*, 443001.

(58) Lee, D. W.; Lee, J.; Sohn, I. Y.; Kim, B. Y.; Son, Y. M.; Bark, H.; Jung, J.; Choi, M.; Kim, T. H.; Lee, C.; Lee, N. E. Field-Effect Transistor with a Chemically Synthesized MoS_2 Sensing Channel for Label-Free and Highly Sensitive Electrical Detection of DNA Hybridization. *Nano Res.* **2015**, *8*, 2340-2350.

(59) Low, L. K.; Meeks, J. R.; Mackerer, C. R. Health Effects of the Alkylbenzenes. I. Toluene. Toxicol. Ind. Heath, **1988**, *4*, 49-75.

(60) Samnakay, R.; Jiang, C.; Rumyantsev, S. L.; Shur, M. S.; Balandin, A. A. Selective Chemical Vapor Sensing with Few-Layer MoS_2 Thin-Film Transistors: Comparison with Graphene Devices. *Appl.*

CHAPTER 3

All 2D Nanomaterial-Based Optoelectronic NO_2 Sensors

3.1 Introduction

Following the discovery of graphene,[1] other two dimensional (2D) materials such as transition metal dichalcogenides (TMDs) have attracted significant attention because of their electronic properties originated from their low-dimensional electronic structure.[2-6] In contrast to graphene, TMDs possess finite bandgap in the range from 0.2 to 3 eV, depending on specific type of material and number of layers, and became a valuable alternative to the conventional or narrow band semiconductors in a variety of electronic and optoelectronic applications.[2-7] MoS_2 is one of the most prominent materials from TMD family possessing a direct bandgap of 1.8 eV as a single layer,[8,9] and showing promising performance in field-effect transistors (FETs), p-n junctions and heterojunctions, photovoltaic cells, and photodetectors demonstrations.[10-15]

Because of their high surface to volume ratio, electronic transport in atomically thin TMD channels is extremely sensitive to the surrounding atmosphere thus allowing their exploration in chemical and biological molecules sensing applications.[16-22] TMDs is now considered as a promising alternative to the conventional metal oxides sensing materials,[23-26] which typically require elevated temperature operations causing excessive energy consumption, reliability issues, and safety concerns. Chemiresistors based on single-and multi-layer MoS_2, either mechanically exfoliated or CVD grown, have been explored for sensing of such hazardous analytes as NO, NH_3, Volatile Organic Compounds (VOCs) and nerve agents at ppm level.[16-22] Nitrogen dioxide (NO_2) is one of the most dangerous pollutants produced mainly as a byproduct of combustion reaction in transportation and industrial processes.[27] It is reported that exposure to as small concentration as 3 ppm can lead to eye and lung irritation, lower resistance to respiratory infection, and possible

fatality.[23] In addition, NO_2 can react with other chemicals in ambient atmosphere to form acid rain and ozone, which are the major harmful components to most ecosystems. Due to such negative impacts to both environment and human life, the United States Environmental Protection Agency (US EPA) has regulated limit of exposure to NO_2 at 53 ppb,[28] thus leading to urgent need to develop a highly sensitive and real-time operating NO_2 gas sensors performing reliably at ppb level.

In recent years, a number of studies demonstrated efficient MoS_2 based NO_2 sensors performances at ppm level.[20,21,29] Moreover, it has been reported recently that chemical vapor deposition (CVD) grown MoS_2 FET-based gas sensor is capable for NO_2 detection at sub-ppm (200 ppb) level.[20] However, these sensors had a slow response and poor recovery at room temperature. Later reports show improved recovery by utilization of elevated temperatures ranging from 100 ºC to 150 ºC due to accelerated desorption of the gas molecules.[30,31] As an alternative strategy, UV light irradiation of the MoS_2 channel was employed to improve sensitivity and recovery rate of the response to NO_2 exposure at ppm level[29] following the strategy developed earlier for metal oxide based sensors.[32,33] In that report,[29] UV light is used as a tool to release oxygen ions from MoS_2 surface thus facilitating the interaction of NO_2 molecules with conducting electrons in MoS_2 channel and yielding faster removal rate of NO_2 molecules after the exposure.

MoS_2 sensing channel can be prepared in different morphologies such as mechanically exfoliated single- or multi-layered,[16,18] MoS_2 nanowires network,[34] or horizontally and vertically aligned MoS_2 layers.[35,36] Each of those morphologies providing significant input in the development of MoS_2-based sensing technology. CVD grown single layer MoS_2 is an ultimate 2D material with highest possible surface-to-volume ratio and is more suited for semiconducting processing platform. However, due to several factors such as large bandgap of MoS_2, grain boundaries of MoS_2 triangular crystals forming its single-layer structure, and contribution of Schottky barriers at metal-MoS_2 contact interfaces, the typical sensor resistance can reach

extremely high values of 10 GΩ to 1 TΩ. This complicates the sensor electrical integration with readout circuit and increases electrical noise thus degrading the sensor performance in terms of limit of detection of gaseous analytes.

Here, we utilize LED illumination with photon energy matching the bandgap of single-layer MoS_2 in order to decrease the MoS_2 channel resistance by 3 orders of magnitude by inducing a photocurrent and employ the generated photocurrent instead of dark current for NO_2 gas sensing. As a result, an efficient response to sub-ppm level of NO_2 concentrations (25 to 200 ppb) exposure was demonstrated with a sensitivity of 4.9%/ppb (4900%/ppm). Further optimization of the MoS_2 based optoelectronic gas sensor by using a graphene (Gr) with lower work function than of Au for the electrical contacts to the MoS_2 channel allowed an increase of photocurrent and improving signal to noise ratio of the gas detection. Calculations of the optimized chemi-photoresistor limit of detection (*LOD*) following IUPAC procedure,[37] provided an evaluation of *LOD* for NO_2 detection at the level of ~0.1 ppb which by far exceeds the US Environment Protection Energy requirement of NO_2 detection at ppb level.

3.2 Experimental Details

3.2.1 MoS_2 growth

MoS_2 films were grown by a CVD method using sulfur and molybdenum trioxide (MoO_3) powders as the precursors and sapphire as the substrate. The growth is carried out in a two-zone tube furnace in 50 sccm of argon under ambient pressure. Temperature at the center of the furnace, where the substrate is positioned above MoO_3 powder, is increased to 650 °C at a ramp rate of 25 °C min^{-1}. Sulfur is introduced to the system by evaporation using a heating jacket at 170 °C as soon as the furnace is turned on. The temperature remains constant at 650 °C for 10 minutes to complete the growth after the furnace and the heating jacket are turned off, and the system is naturally cooled to room temperature.

3.2.2 Graphene growth

We employ the method recently reported in our recent publication to produce continuous graphene film.[58] In brief, a 2x5 cm^2 piece of polycrystalline copper foil is used as the growth substrate. The copper foil is annealed 1030 °C in the presence of H_2 (10 sccm) and argon (300 sccm) for 2 hours in one-inch quartz tube furnace. Diluted CH_4 in argon (90 ppm) is introduced for 1 hour at a flowrate of 375 sccm while H_2 flow remains unchanged. The system is then cooled to room temperature under H_2 (10 sccm) and argon (300 sccm).

3.2.3 Device preparation

3.2.3.1 Au-MoS_2-Au device

After the growth, MoS_2 on sapphire is spin-coated with polystyrene (PS). (PS/MoS_2) film is delaminated in DI water and washed several times with DI water to remove remaining residues. The floating PS/MoS_2 is transferred on a SiO_2(300 nm)/Si, and PS coating is dissolved by immersing the chip in toluene solution at room temperature. 5 nm/ 50 nm thick Cr/Au electrodes are patterned and deposited using standard photolithography procedures and electron-beam metal deposition. The lateral dimensions of MoS_2 channel of 10 μm by 10 μm are defined by the inter-electrode spacing and the electrodes width, both of 10 μm. No additional patterning of MoS_2 channel was required due to high MoS_2 layer sheet resistance as the only area between the electrodes is contributing to the device dark or photo- currents.

3.2.3.2 Gr-MoS_2-Gr device

Appx. B6(a) and B6(b) present optical images of the MoS_2 optoelectronic gas sensor with two patterned graphene electrodes of width of 10 μm and separated by 10 μm. Graphene electrodes are fabricated directly on graphene/copper foil using standard photolithography. The unwanted graphene area is removed using reactive ion etching (O_2 plasma). Graphene electrodes are isolated from the copper foil *via* a common wet transfer technique supported by PMMA film and using 0.2

M APS solution as copper etching solution. The floating PMMA/graphene electrodes film is washed multiple times with deionized (DI) water to remove any residue. This PMMA/graphene electrode film is transferred onto a MoS_2 film prepared on Si/SiO_2 substrate. The PMMA layer is then removed in acetone at 60 °C. A small area of 5 nm/ 50 nm thick Cr/Au areas are deposited as electrical contacts using electron-beam metal deposition. Raman spectrum of graphene **(Appx. B6(c))** shows strong G peak at 1590 cm^{-1} and 2D peak at 2680 cm^{-1} as compared to very weak D peak at 1350 cm^{-1}, confirming the high quality of graphene and preservation of its properties after the transfer and lithographic electrode patterning.

3.2.3.3 Au/Gr-MoS_2-Gr/Au device

For this device structure, another step of photolithography is required to create an overlapping pattern on the existing graphene electrodes. A 5 nm/ 50 nm thick Cr/Au layer is deposited on top of graphene electrodes using electron-beam metal deposition. For all three structures, a final step of annealing at 200 °C in 15 sccm H_2 and 300 sccm argon is required to remove remaining residues and increase the contact between layers.

3.2.4 Material and device characterization

Raman and PL spectra were collected on Horiba LabRam system using a green laser with wavelength of 532 nm and 100x objective (NA=0.9). The power of the laser beam is fixed at 5 mW to avoid local heating to the materials. Optical image is taken with Hirox KH-7700 digital microscope. SEM imaging was conducted utilizing Zeiss 1540 XB Crossbeam Scanning Electron Microscope.

3.2.5 Electrical and photoconductivity measurements, and NO_2 sensing experiments

The current-voltage (I-V) measurement in dark and under the light were conducted utilizing a Keithley 236 source-measure unit. The instruments control and data acquisition for all the measurements were conducted utilizing Labview hardware and software. For photoconductivity

and gas sensing measurements the red LED (model L10762, Hamamatsu Photonics) with the central wavelength of 660 nm was integrated with the gas sensing mini-chamber. The LED power density was modulated utilizing a function generator DS360 (Stanford Research Systems), and the light intensity on the device was calibrated by silicon photodetector. The frequency dependencies of the photoresponse were studied using a lock-in amplifier (SRS 830, Stanford Research Systems) with the dc bias of 5 V supplied by Keithley 236 source-measure unit, and the load resistance of 100 kΩ.

For gas sensing experiments, the concentrations of NO_2 gas is regulated by two Alicat Scientific mass flow controllers: one controlling the flow of 99.99% pure N_2 gas and the other controlling the flow of 10 ppm NO_2 in N_2. The target NO_2 concentration for detection of 25 ppb, 50 ppb, 100 ppb, 150 ppb, 200 ppb are achieved by mixing NO_2 flow with N_2 flow at ratios of 1:399, 2:398, 4:396, 6:394 and 8:392, respectively while the total flowrate to the sensing chamber remains constant at 400 sccm.

3.3 Results and Discussion

Figures 3.1(a) presents an optical image of the MoS_2 optoelectronic gas sensor with two patterned Au electrodes with 10 μm by 10 μm gap. **Figures 3.1(b) and 3.1(c)** show SEM imaging of MoS_2 layer forming the device channel with typical morphology of one atomic layer network of merging triangular MoS_2 crystals. Detailed information on MoS_2 layer growth and the device preparation is presented in Experimental Section below. Raman spectrum of MoS_2 (**Figure 3.1(d)**) shows E^1_{2g} peak at 386 cm^{-1} and A_{1g} peak at 405 cm^{-1} in a ratio of $E^1_{2g}/A_{1g} \approx 1$ indicating a basal plane exposed morphology[34,35] and separated by 19 cm^{-1} in agreement with the expected value for a single-layer MoS_2.[8,9] The presence of strong photoluminescence peak at 1.86 eV photon energy (**Figure 3.1(e)**) confirms that the device channel is predominantly single-layer MoS_2.[8]

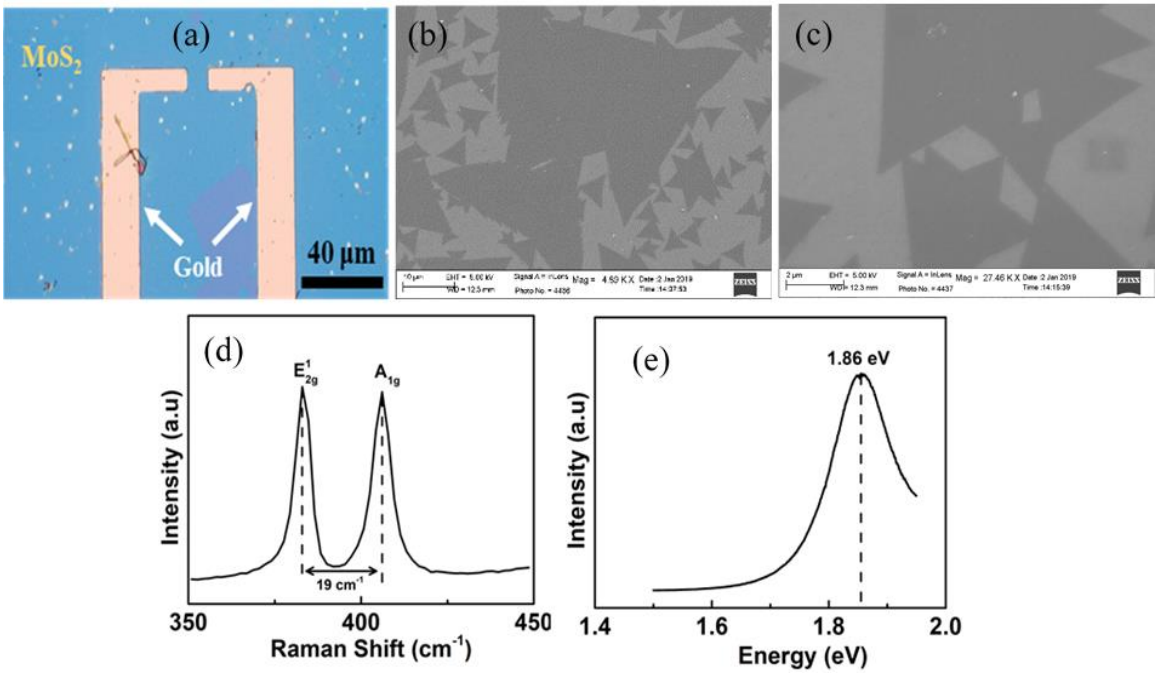

Figure 3.1. (a) Optical image of MoS_2 device with Au electrodes; (b) and (c) SEM images of MoS_2 layer at different magnifications with MoS_2 corresponding to lighter areas (scale bars 10 μm and 2 μm, respectively); (d) Raman and (e) Photoluminescence spectra of MoS_2 layer.

Figure 3.2(a) shows a schematic of MoS_2 channel with Cr/Au electrodes denoted in this paper as Au-MoS_2-Au device. I-V curve in dark (**Figure 3.2(b)**) shows very low current in pico-amperes range corresponding to the very high device resistance of ~200 GΩ. Such high device resistance is due to the presence of two Schottky diode type Au/MoS_2 junctions connected in series in opposite directions, so the current through the channel is always limited by the Schottky diode which is biased in reverse. In most of our measurements the bias across the device is limited to 5 V while at higher voltages the devices show non-linearity associated with reverse breakdown typical for Schottky diodes (**Appx. B1**). Under illumination of red LED of incident power of 60.9 nW (light intensity of 60.9 mW/cm^2) the channel current increased by ~500 times exceeding 10 nA at 5 V channel bias (**Figure 3.2(c)**).

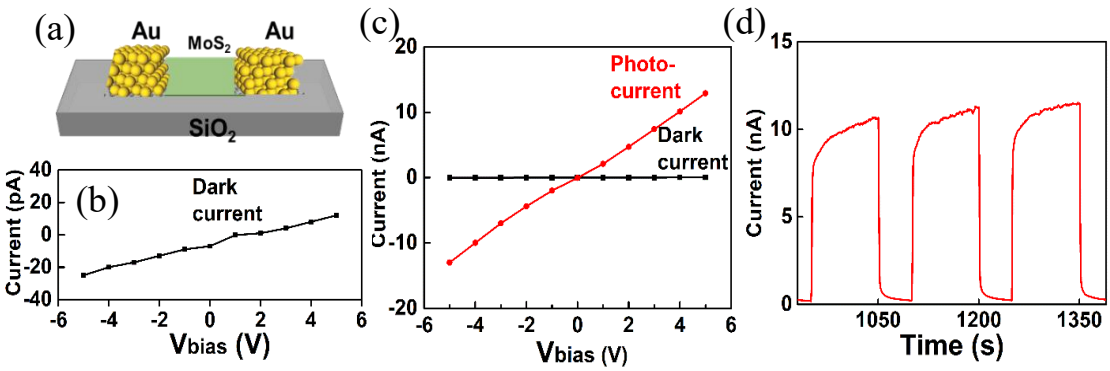

Figure 3.2. (a) Schematic of MoS_2 channel with Au electrodes; I-V dependence of Au-MoS_2-Au device (b) in dark and (c) under red LED illumination of incident power of 60.9 nW; (d) photocurrent pulses as a response to "on" and "off" switching of red LED irradiation.

The temporal evolution of the photocurrent when LED irradiation was switched "on" and "off" is presented in **Figure 3.2(d)**. It shows a relatively fast rise of the photocurrent to ~80% level in less than 1 s when LED irradiation was switched "on" followed by a slow increase continuing for hundreds of seconds. A similar shape was observed in the photocurrent decay when LED was turned "off" with an initial fast decay to below 10% level in less than 1 s followed by a slow decay.

We next investigated the ability of the above device as a gas sensor for NO_2. **Figure 3.3(a)** compares typical responses, represented in terms of normalized change of resistance ($\Delta R/R_{N2}$, where R_{N2} is the resistance of the device established under N_2 flow before NO_2 exposure in dark or under illumination and ΔR is a resistance change caused upon NO_2 exposure), of single-layer MoS_2-based gas sensors with Cr/Au electrodes (from here on referred to by Au-MoS_2-Au) to NO_2 gas exposure in dark and under red LED illumination of incident power of 60.9 nW (light intensity of 60.9 mW/cm^2). For raw resistance data please see **Appx. B2 and B3** in Supporting Information. It is worth noting, that the sensor exhibited similar sensitivity to NO_2 even when air was used as the carrier/dilution gas instead of nitrogen (data not shown).

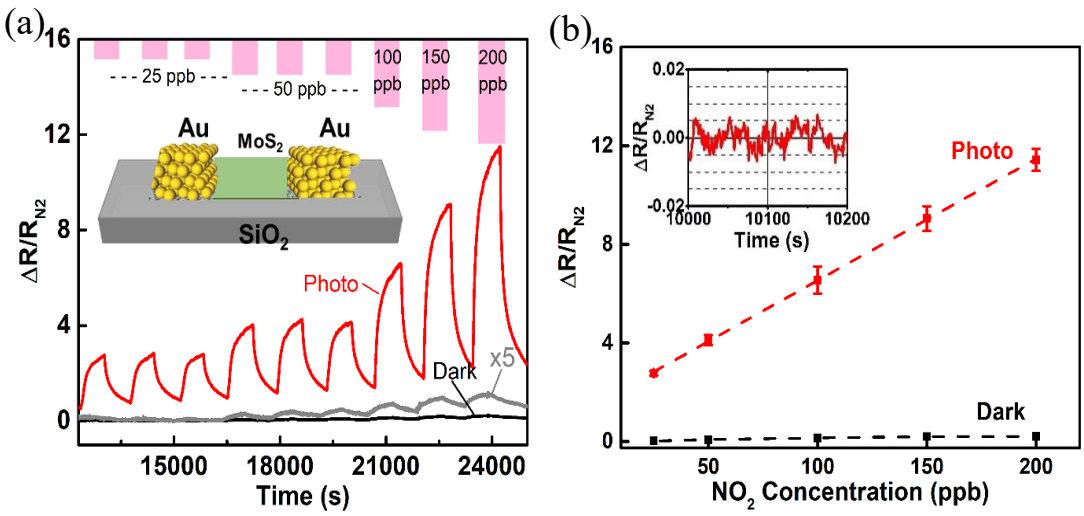

Figure 3.3. (a) Effect of NO_2 gas exposure at concentrations from 25 to 200 ppb on normalized resistance of Au-MoS_2-Au device in dark (black line, gray line shows 5-fold magnified data) and under red LED illumination (red curve). (b) Dependence of the normalized amplitude of resistance change $\Delta R/R_{N2}$ on the concentration of NO_2 gas. Inset shows a temporal trace of experimentally recorded noise of $\Delta R/R_{N2}$. All data were collected under DC bias of 5 V.

Noticeably, the response to NO_2 exposure under illumination is enhanced dramatically even when the dark current data is magnified by a factor of 5. **Figure 3.3(b)** presents the amplitude of relative response $\Delta R/R_{N2}$ in dark and under illumination as a function of NO_2 concentration C (ppb) with a slope of such dependence defining the device sensitivity $S=\Delta R/R_{N2}(\%)/C(\text{ppb})$. Under red LED illumination the NO_2 sensitivity of S=4.9%/ppb (4900%/ppm) was observed which is ~50-fold higher than the best values of 0.1%/ppb obtained in the dark. Some of the tested Au-MoS_2-Au sensors didn't show any response in the dark to sub-ppm concentrations of NO_2, while the sensitivity under red LED light illumination was consistently high. It should be noted that the sensitivity is usually normalized to the concentration expressed in ppm units, however, in our work we report sensitivity in %/ppb units due to the strong response of our sensor to ppb level concentration of NO_2.

Another important figure of merit of chemical sensor is limit of detection (*LOD*) of the particular analyte which, following IUPAC procedure, is typically defined as a concentration of the analyte which causes a response 3 times higher than the noise level of the device (*i.e.* in the absence of the analyte).[37,38] From the noise data presented in **Figure 3.3(b) (inset)** for the illuminated sensor root-mean-square (RMS) value of $\Delta R/R_{N2}$ noise of ~ 0.32% is obtained giving an calculated *LOD* of 3x0.32/4.9 ≈ 0.2 ppb. For comparison, the noise level for the sensor in dark is ~0.6% with much lower sensitivity of 0.1%/ppb resulting in detection limit of 3x0.6/0.1≈18 ppb in agreement with the visual observation of data presented in **Figure 3.3**. Thus, bandgap matching illumination of MoS_2 sensor induces photocurrent in the sensor channel which can be used to significantly improve the sensitivity and detection limit of NO_2 sensing.

The observed improvement of MoS_2 sensor performance is associated with current enhancement in MoS_2 channel induced by photoexcitation of electron-pairs across the direct bandgap of single-layer MoS_2. Here, we utilized Au as a metal to provide the electrical contacts to the MoS_2 channel, but recent theoretical study and related experiments suggested that this most common metal may be inefficient for electron injection into single-layer MoS_2.[39] Other metals,

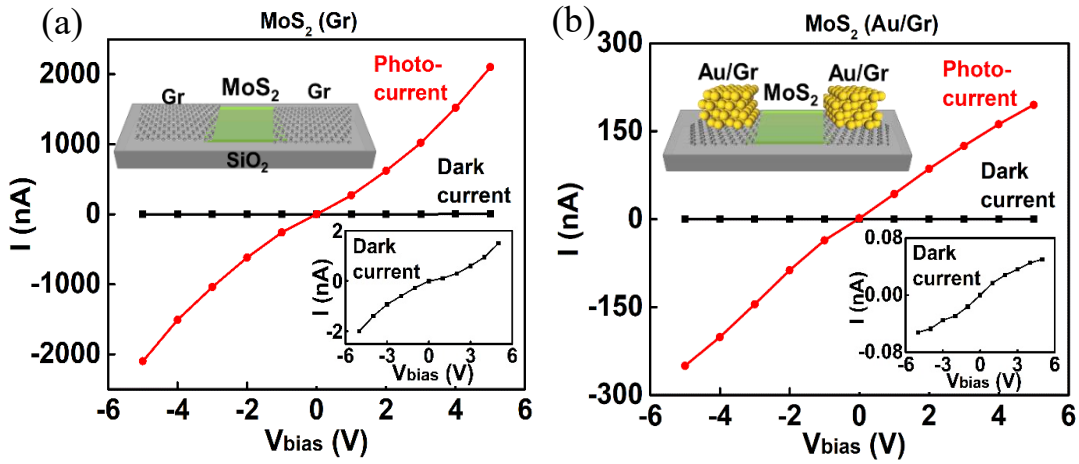

Figure 3.4. I-V curves under red LED illumination (red line) and in dark (black line) of (a) Gr-MoS_2-Gr and (b) Au/Gr-MoS_2-Gr/Au devices. Insets show corresponding schematics of the devices and expanded I-V curves in dark.

such as Ti, were suggested as alternatives, but also graphene was proposed and experimentally tested as an atomically thin contacting layer ideally matching 2D structure of MoS_2.[40-42] Thus two additional variations of MoS_2 based optoelectronic NO_2 sensor were fabricated and tested. In the first variation gold electrodes were substituted by graphene resulting in Gr-MoS_2-Gr sensor (**Figure 3.4(a) (inset)**; **Appx. B6**); in the 2nd variation graphene electrodes were protected from the exposure to NO_2 gas by applying a top Cr/Au (5 nm/50 nm) coating resulting in Au/Gr-MoS_2-Gr/Au type sensor (**Figure 3.4(b) (inset)**).

As shown in **Figure 3.4**, both device configurations involving graphene electrodes show more than 3 orders of magnitude higher current under the incident red LED illumination power of 60.9 nW (per 10 μm by 10 μm sensor area) when compared to absence of light. The highest dark- and photo-currents are observed for the device with bare graphene electrodes. Among the devices with three types of electrodes, the device with Au electrodes (Au-MoS_2-Au) shows the lowest current (**Figure 3.2, Appx. B1**). We ascribe this to a higher work function of Au (5.1 eV) than the work function of pristine graphene (4.5-4.6 eV);[17] however, the later can increase to 5.0 eV and higher[43] as graphene is commonly p-doped due to nano-fabrication processes, such as copper etching, lithography and O_2 plasma etching. Assuming that the currents are limited by the height of the Schottky barrier Φ_{SB} at the electrode – MoS_2 interfaces, the ratio of the currents in case of Au (I_{Au}) and graphene (I_{GR}) can be used for rough estimation of the Schottky barrier height differences in the approximation of thermionic emission model:[17, 44] $\Delta\Phi_{SB} = \Phi_{SB}$ (Au) - Φ_{SB} (Gr) = $(k_BT/e)*\ln(I_{Au}/I_{GR}) \approx 0.12$ eV, where k_B and e are Boltzmann constant and elementary charge of electron, respectively. For the case of Au coated graphene a smaller Schottky barrier difference

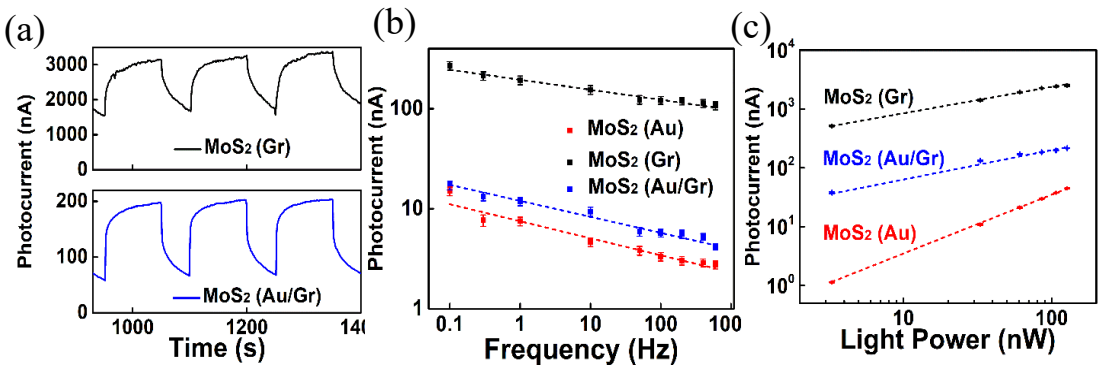

Figure 3.5. (a) Photocurrent pulses as a response to switching of red LED irradiation "on" and "off" for Gr-MoS_2-Gr (top) and Au/Gr-MoS_2-Gr/Au (bottom) devices. Dependence of photocurrent on (b) frequency of red LED modulation and (c) power of red LED irradiation for MoS_2 devices with 3 types of electrodes. Dashed lines show power law fits of experimental dependences as described in the text. All data were taken with bias of 5 V.

$\Delta\Phi_{SB}$ = Φ_{SB} (Au) - Φ_{SB} (Gr/Au) of 0.07-0.08 eV was obtained which can be explained by the influence of bulk layer of Au on the work function of graphene shifting the work function of the Au coated graphene closer to the Au work function. The results of photoconductivity and NO_2 gas sensing were obtained from 4-5 devices with each type of electrodes. MoS_2 devices with graphene electrodes show the highest photoresponsivity in the range of 30-150 A/W, which is on the high end of the photoresponsivities reported in literature for MoS_2 based devices.[45,46] With increasing Schottky barrier height the photoresponsivity decreases to values 3-12 A/W for the case of Gr/Au electrodes, and to 0.2-0.34 A/W for the case of Au electrodes as measured on several devices of each type.

Figure 3.5(a) shows time-dependent photocurrent induced in the MoS_2 channels with graphene electrodes (bare and Au coated) in a response to the "on" and "off" switching of the LED illumination. In both cases, fast and slow components of the photoresponse can be observed similar to the case of the device with Au electrodes (**Figure 3.2(c)**). In case of graphene electrodes, the slow component dominates resulting in large persistent photocurrent,[47] so the current remains well

above its steady state dark current value during the intervals when the LED irradiation is turned off.

The dependences of the amplitude of the photocurrent of the MoS_2 devices on the frequency f of square-wave red LED light modulation are presented in **Figure 3.5(b)** and show a decrease of photocurrent with increasing frequency described by power law $I_{ph} \propto f^{-\alpha}$ with best fitting obtained using exponents α of 0.17, 0.1 and 0.16 for the devices with Au, graphene and graphene/Au electrodes, respectively. Such type of power law dependence of photocurrent with exponent α <1 are well known in the field of classical photoconductors, and is usually associated with wide distribution of photocarrier lifetimes (in our case from milliseconds to tens of seconds) due to the presence of trap states.[13, 46-49] Such traps can be associated with sulfur vacancies which are typically major defects present in the CVD-MoS_2 also responsible for n-type doping.[50,51] Additional trap states may originate from the dangling Si-O bonds at the surface of SiO_2 substrate, as reported previously.[52,53] **Figure 3.5(c)** shows that the dependence of photocurrent on the incident irradiation power P deviates from direct proportionality and is best described by the power law $I_{ph} \propto P^{\beta}$, similar to the recent reports,[19] with the exponents β values less than unity of 0.63, 0.45, and 0.50 for the devices with Au, graphene and graphene/Au electrodes, respectively. Such β <1 values are also typically associated with the presence of trap states distributed in energy within the bandgap of the conventional photoconductors.[47] In case of 2D materials with high surface to volume ratio the effect of trap states on the photoconductivity is often described in terms of photogating when under illumination one type of photocarriers is trapped by lattice defects or impurities.[46,49] Such trapping leads to the spatial charge accumulation and induced electric field which acts as a gate voltage in conventional FETs shifting the Fermi level of 2D channel to the energy position dependent on the time and intensity of incident radiation.[13,46,47,49] The contribution of photogating can explain the power law dependences of photocurrent on frequency and incident power with

exponents α and β less than unity presented in **Figure 3.5**. In case of single layer MoS_2 channel utilized in this study the trap states can be formed at the interface of MoS_2 and supporting dielectric (SiO_2) layer or on the top of MoS_2 layer. The fast photoresponse component visible at the moment of LED switching "on" and "off" and at high frequencies of modulation can be attributed to direct photoconductivity while slow component of photoresponse can be associated with photogating, however, the boundary between these two contributions cannot be well defined.

The devices with graphene and graphene/Au electrodes were evaluated for NO_2 sensing under light. **Figure 3.6(a)** shows the transient normalized resistance change (response) of MoS_2 channel with graphene electrodes (Gr-MoS_2-Gr) to 25 to 200 ppb of NO_2 gas exposure. As illustrated in the figure, the device exhibited a response ($\Delta R/R_{N2}$) of ~16% (from 0.85 MΩ to 0.99 MΩ) to as low as 25 ppb NO_2 concentration, the smallest reliably achievable concentration in our setup. Further, the normalized resistance change showed a stronger increase with increasing NO_2 concentration, followed by a full recovery. A similar trend, but of much higher magnitude with faster and fuller recovery to baseline upon exposure to only N_2, was observed in the case of device made of MoS_2 channel with graphene electrodes protected by Au layer (Au/Gr-MoS_2-Gr/Au) (Fig. 6b). **Appx. B4 and B5** present the raw resistance data upon exposure to different NO_2 concentrations for the above two types of devices used in these figures. Additionally, the baseline photocurrent (in the absence of NO_2 exposure) of Au/Gr-MoS_2-Gr/Au was an order of magnitude lower, 6 *vs* 0.8 μA, when compared to the Gr-MoS_2-Gr (bare graphene electrodes) device which is ascribed to higher Schottky barrier caused by the influence of bulk Au layer, discussed previously.

Figure 3.6(c) and 3.6(d) present the normalized resistance change ($\Delta R/R_{N2}$), sensor response, as a function of NO_2 concentration (*i.e.* calibration plot) for Gr-MoS_2-Gr and Au/Gr-MoS_2-Gr/Au devices, respectively. The corresponding analytical characteristics of sensitivity and limit of

detection of these devices for NO_2 sensing (calculated the same way as described earlier/above) are summarized in **Table 3.1**.

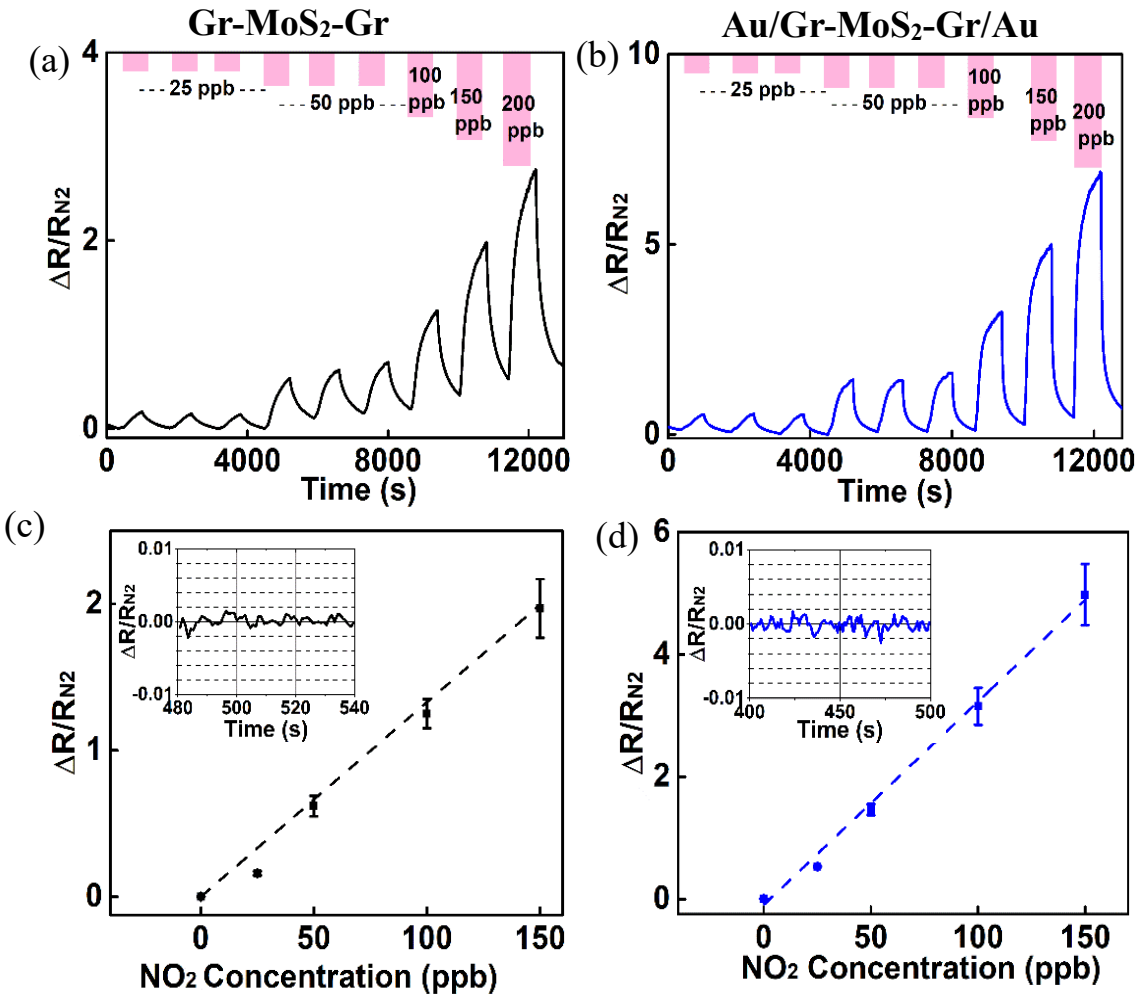

Figure 3.6. Effect of NO_2 gas exposure at concentrations from 25 to 200 ppb under red light on normalized resistance of Gr-MoS_2-Gr device (a) and Au/Gr-MoS_2-Gr/Au (b). Dependence of the normalized amplitude of resistance change of Gr-MoS_2-Gr (c) and Au/Gr-MoS_2-Gr/Au (d) devices on the concentration of NO_2 gas. Inset shows a temporal trace of experimentally recorded noise of $\Delta R/R_{N2}$. All data were collected under dc bias of 5 V.

Table 3.1. Analytical characteristics of single-layer MoS_2 channel gas sensors with different source-drain electrodes for NO_2 sensing

Device/Condition	Sensitivity, %/ppb	Limit of Detection, ppb
Au-MoS_2-Au/Dark	0.1	18
Au-MoS_2-Au/Light	4.9	0.2
Gr-MoS_2-Gr	1.3	0.2
Au/Gr-MoS_2-Gr/Au	3.3	0.1

The results show that the Au/Gr-MoS_2-Gr/Au device had higher sensitivity (3.3%/ppb *vs* 1.3%/ppb) and lower *LOD* (0.1 ppb *vs* 0.2 ppb) compared to Gr-MoS_2-Gr device. We should note that MoS_2-based sensors demonstrated long term stability under many hours of red LED illumination, NO_2 exposure during performance testing, and storage as illustrated in **Appx. B7**.

The band diagram of the MoS_2 channel in dark is presented in **Figure 3.7(a)** with Fermi level shifted towards conduction band for typically n-type doped MoS_2. Because of the relatively large band gap of MoS_2 and high Schottky barriers at the metal electrode/MoS_2 interfaces the concentration of free carriers is very low with thermally excited electrons and holes acting as majority and minority carriers, respectively. The relatively low sensitivity of the sensor in dark can

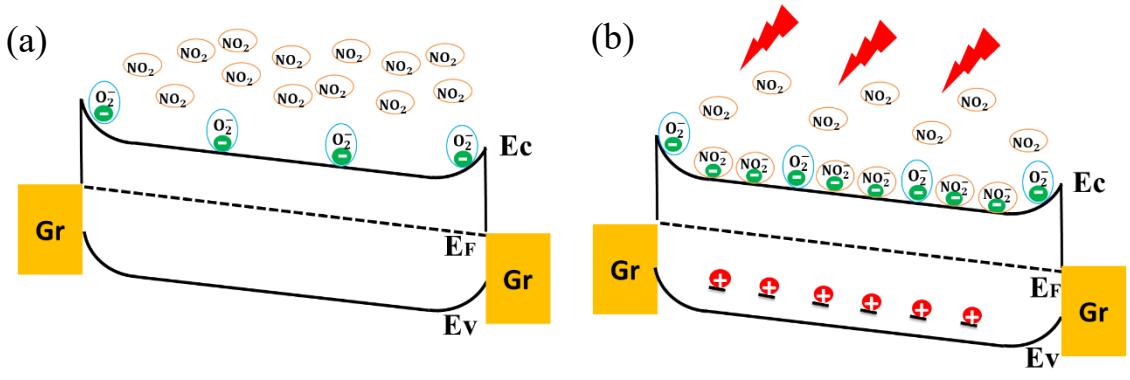

Figure 3.7. Band diagram of the device showing interaction of conduction band electrons in MoS_2 with NO_2 gas molecules (a) in dark and (b) under red light illumination.

be explained by the presence of oxygen which traps the thermally excited electrons in MoS_2 channel leading to further reduction of the device current. Thus, most of electrons are blocked by oxygen from interaction with NO_2 molecules resulting in suppressed response to the analyte. As schematically illustrated in **Figure 3.7(b)**, under red light illumination the population of free electrons increases by several order of magnitude.

Part of this increase can be due to photogating[46,49] when photoexcited holes are trapped at the MoS_2/SiO_2 interface generating a spatial positive charge which shifts the Fermi level closer to the edge of conduction band and increasing a population of the thermally excited electrons. These extra electrons are not blocked by oxygen and available for interaction with NO_2 molecules because of the single layer structure of MoS_2 when any charge carrier is at the surface. As discussed in literature, NO_2 gas molecules absorbed on MoS_2 channel surface act as electron acceptors and capture the photoexcited electrons thus leading to a decrease of current (photocurrent) in the channel.[17,29]

Substitution of Au with graphene results in decreasing Schottky barrier height and improving current injection which leads to higher photocurrent. However, due to its high surface-area-to-volume ratio, graphene provides a high density of binding sites for NO_2 gas molecules. It has been reported that the work function of single layer graphene and the height of the Schottky barrier at MoS_2/graphene interface can be affected by NO_2 exposure[54,55] which may lead to observed decreasing sensitivity of MoS_2(Gr) as compared to the other types of electrodes. In addition, trapping of NO_2 molecules on the high surface area graphene electrodes can be a cause of more slow recovery after the exposure than in case of Au/Gr-MoS_2-Gr/Au device as observed in **Figure 3.6**. The exposure of the contact layer to the analyte can also serve as an additional source of noise which can be eliminated in a case of graphene electrode protected from NO_2 exposure by Au layer.

As discussed above, the encapsulation of graphene electrodes with Au layer affects the work function of graphene resulting in increasing Schottky barrier height and decreasing photocurrent. On the other hand, it protects the device from the negative effects originated from interaction of graphene electrodes with NO_2 molecules such as decreasing sensitivity due to modulation of work function and a slow sensor recovery. The encapsulation of graphene may also improve the long-term stability of the optoelectronic gas sensor which will be evaluated in our future studies.

Table 3.2 summarizes state of the art parameters reported in literature for MoS_2 based NO_2 gas sensors.[16,17,19,20,29-31,34,56,57] The optoelectronic MoS_2 sensor operating under red LED light illumination presented in this work shows the highest reported sensitivity to low dosage of NO_2 gas, because the photocurrent is used to enhance the sensor response. The calculations following IUPAC defined procedure gave extremely low detection limit in sub-ppb range (0.1 ppb) well suited to US EPA needs for NO_2 sensing at ppb level.

Table 3.2. Comparison between reports on MoS_2 based NO_2 gas sensors and present work

Material	Temperature	Minimum concentration tested	Detection limit (Calculation)	Sensitivity %/ppm	Ref.
MoS_2	RT	100 ppm	20 ppm	1.37/ppm	16
MoS_2	RT	20 ppb	10 ppb	194/ppm	17
MoS_2	RT	120 ppb	25 ppb	90/ppm	19
Gr/MoS_2	150 ^{o}C	1.2ppm	1.2 ppm	3/ppm	20
MoS_2	RT (UV)	5 ppm	1-5 ppm	0.12/ppm	29
MoS_2	100 ^{o}C	5 ppm	1-5 ppm	0.06/ppm	29
MoS_2/Gr	200 ^{o}C	50 ppb	14 ppb	18/ppm	30
3D MoS_2	200 ^{o}C	50 ppb	28 ppb	20 /ppm	31
MoS_2 Nanowire	60 ^{o}C	1 ppm	4.6 ppb	2.65/ppm	34
PtNPs/MoS_2	RT	0.5 ppm	2 ppb	11/ppm	56
MoS_2	100 ^{o}C	25 ppb	2 ppb	0.18/ppm	57
MoS_2	RT (red light)	25 ppb	0.1ppb	3.3/ppb (3300/ppm)	This work

3.4 Conclusion

Red light LED illumination with photon energy matching the direct bandgap of the single layer MoS_2 allowed to use induced photocurrent instead of dark current as a tool for NO_2 gas sensing. The resulted sensor showed extremely high sensitivity to ppb level NO_2 gas exposure up to 3.3 %/ppb (3300 %/ppm) and sub-ppb limit of NO_2 gas detection at the 0.1 ppb level. The presented concept of enhancing gas sensing performance by inducing a photocurrent can be expanded on different analytes and employ other 2D TMD materials by matching the photon energies to the specific bandgaps.

3.5 References

(1) Novoselov, K. S.; Geim, A. K.; Morozov, S. V.; Jiang, D.; Zhang, Y.; Dubonos, S. V.; Grigorieva, I. V.; Firsov, A. A. Electric Field Effect in Atomically Thin Carbon Films. *Science* **2004**, *306*, 666-669.

(2) Wang, H.; Yu, L.; Lee, Y. H.; Shi, Y.; Hsu, A.; Chin, M. L.; Li, L. J.; Dubey, M.; Kong, J.; Palacios, T. Integrated Circuits Based on Bilayer MoS_2 Transistors. *Nano Lett.* **2012**, *12*, 4674-4680.

(3) Geim, A. K.; Grigorieva, I. V. Van der Waals Heterostructures. *Nature* 2013, *499*, 419-425.

(4) Xu, M.; Liang, T.; Shi, M.; Chen, H. Graphene-Like Two-Dimensional Materials. *Chem. Rev.* **2013**, *113*, 3766-3798.

(5) Jariwala, D.; Sangwan, V. K.; Lauhon, L. J.; Marks, T. J.; Hersam, M. C. Emerging Device Applications for Semiconducting Two-Dimensional Transition Metal Dichalcogenides. *ACS Nano* **2014**, *8*, 1102-1120.

(6) Tan, C.; Cao, X.; Wu, X. J.; He, Q.; Yang, J.; Zhang, X.; Chen, J.; Zhao, W.; Han, S.; Nam, G. H.; Sindoro, M.; Zhang, H. Recent Advances in Ultrathin Two-Dimensional Nanomaterials. *Chem. Rev.* **2017**, *117*, 6225-6331.

(7) Sun, Z.; Martinez, A.; Wang, F. Optical Modulators with 2D Layered Materials. *Nat. Photonics* **2016**, *10*, 227-238.

(8) Mak, K. F.; Lee, C.; Hone, J.; Shan, J.; Heinz, T. F. Atomically Thin MoS_2: A New Direct-Gap Semiconductor. *Phys. Rev. Lett.* **2010**, *105*, 136805.

(9) Lee, C.; Yan, H.; Brus, L. E.; Heinz, T. F.; Hone, J.; Ryu, S. Anomalous Lattice Vibrations of Single- and Few-Layer MoS_2. *ACS Nano* **2010**, *4*, 2695-2700.

(10) Radisavljeic, B.; Radenovic, A.; Brivio, J.; Giacometti, V.; Kis, A. Single-Layer MoS_2 Transistors. *Nat. Nanotechnol.* **2011**, *6*, 147-150.

(11) Choi, M. S.; Qu, D.; Lee, D.; Liu, X.; Watanabe, K.; Taniguchi, T.; Yoo, W. J. Lateral MoS_2 p-n Junction Formed by Chemical Doping for Use in High-Performance Optoelectronics. *ACS Nano* **2014**, *8*, 9331-9340.

(12) Wi, S.; Kim, H.; Chen, M.; Nam, H.; Guo, L. J.; Meyhofer, E.; Liang, X. Enhancement of Photovoltaic Response in Multilayer MoS_2 Induced by Plasma Doping. *ACS Nano* **2014**, *6*, 5270-5281.

(13) Lopez-Sanchez, O.; Lembke, D.; Kayci, M.; Radenovic, A.; Kis, A. Ultrasensitive Photodetectors Based on Monolayer MoS_2. *Nat. Nanotechnol.* **2013**, *8*, 497-501.

(14) Zhang, W.; Huang, J. K.; Chen, C. H.; Chang, H. Y.; Cheng, Y. J.; Li, L. J. High-Gain Phototransistors Based on a CVD MoS_2 Monolayer. *Adv. Mater.* **2013**, *25*, 3456-3461.

(15) Yin, Z.; Li, H.; Li, H.; Jiang, L.; Shi, Y.; Sun, Y.; Lu, G.; Zhang, Q.; Chen, X.; Zhang, H. Single-Layer MoS_2 Phototransistors. *ACS Nano* **2012**, *6*, 74-80.

(16) Late, D. J.; Huang, Y. K.; Liu, B.; Acharya, J.; Shirodkar, S. N.; Luo, J.; Yan, A.; Charles, D.; Waghmare, U. V.; Dravid, V.; Rao, C. N. R. Sensing Behavior of Atomically Thin-Layered MoS_2 Transistors. *ACS Nano* **2013**, *7*, 4879-4891.

(17) Liu, B.; Chen, L.; Liu, G.; Abbas, A. N.; Fathi, M.; Zhou, C. High-Performance Chemical Sensing Using Schottky-Contacted Chemical Vapor Deposition Grown Monolayer MoS_2 Transistors. *ACS Nano* **2014**, *8*, 5304-5314.

(18) Li, H.; Yin, Z.; He, Q.; Li, H.; Huang, X.; Lu, G.; Fam, D. W. H.; Tok, A. L. Y.; Zhang, Q.; Zhang, H. Fabrication of Single- and Multilayer MoS_2 Film-Based Field-Effect Transistors for Sensing NO at Room Temperature. *Small* **2011**, *8*, 63-67.

(19) Cho, B.; Kim, A. R.; Yoon, D.; Lee, Y. J.; Lee, S.; Yoo, T. J.; Kang, C. G.; Lee, B. H.; Ko, H. C.; Kim, D. H.; Hahm, M. G. Bifunctional Sensing Characteristics of Chemical Vapor Deposition Synthesized Atomic-Layered MoS_2. *ACS Appl. Mater. Interfaces* **2015**, *7*, 2952-2959.

(20) Cho, B.; Yoon, J.; Lim, S. K.; Kim, D. H.; Park, S. G.; Kwon, J. D.; Lee, Y. J.; Lee, K. H.; Lee, B. H.; Ko, H. C.; Hahm, M. G. Chemical Sensing of 2D Graphene/MoS_2 Heterostructure Device. *ACS Appl. Mater. Interfaces* **2015**, *7*, 16775-16780.

(21) Perkins, F. K.; Friedman, A. L.; Cobas, E.; Campbell, P. M.; Jernigan, G. G.; Jonker, B. T. Chemical Vapor Sensing with Monolayer MoS_2. *Nano Lett.* **2013**, *13*, 668-673.

(22) Kim, J. S.; Yoo, H. W.; Choi, H. O.; Jung, H. T. Tunable Volatile Organic Compounds Sensor by Using Thiolated Ligand Conjugation on MoS_2. *Nano Lett.* **2014**, *14*, 5941-5947.

(23) Wetchakun, K.; Samerjai, T.; Tamura, N.; Liewhiran, C.; Siriwong, C.; Kruefu, V.; Wisitsoraat, A.; Tuantranont, A.; Phanichphant, S. Semiconducting Metal Oxides as Sensors for Environmentally Hazardous Gases. *Sens. Actuators B: Chem.* **2011**, *160*, 580-591.

(24) Mubeen, S.; Lai, M.; Zhang, T.; Lim, J. H.; Muchandani, A.; Deshusses, M. A.; Myung, N. V. Hybrid Tin Oxide-SWNT Nanostructures based Gas Sensor. *Electrochim. Acta* **2013**, *92*, 484-490.

(25) Dey, A. Semiconductor Metal Oxide Gas Sensors: A Review. *Mater. Sci. Eng. B* **2018**, *229*, 206-217.

(26) Fine, G. F.; Cavanagh, L. M.; Afonja, A.; Binions, R. Metal Oxide Semi-Conductor Gas Sensors in Environmental Monitoring. *Sensors* **2010**, *10*, 5469-5502.

(27) Atkinson, R. Atmospheric Chemistry of VOCs and NO_x. *Atmos. Environ.* **2000**, *34*, 2063-2101.

(28)U. S. Environmental Protection Agency, "Air Trends Summary Report": https://www3.epa.gov/ttn/naaqs/standards/nox/s_nox_history.html #3 (accessed Feb 5, **2019**).

(29) Kumar, P.; Goel, N.; Kumar, M. UV-Activated MoS_2 Based Fast and Reversible NO_2 Sensor at Room Temperature. *ACS Sens.* **2017**, *2*, 1744-1752.

(30) Long, H.; Harley-Trochimczyk, A.; Pham, T.; Tang, Z.; Shi, T.; Zettl, A.; Carraro, C.; Worsley, M. A.; Maboudian, R. High Surface Area MoS_2/Graphene Hybrid Aerogel for Ultrasensitive NO_2 Detection. *Adv. Funct. Mater.* **2016**, *26*, 5158-5165.

(31) Long, H.; Chan, L.; Harley-Trochimczyk, A.; Luna, L. E.; Tang, Z.; Shi, T.; Zettl, A.; Carraro, C.; Worsley, M. A.; Maboudian, R. 3D MoS_2 Aerogel for Ultrasensitive NO_2 Detection and Its Tunable Sensing Behavior. *Adv. Mater. Interfaces* **2017**, *4*, 1700217.

(32) Fan, S. W.; Srivastava, A. K.; Dravid, V. P. UV-Activated Room-Temperature Gas Sensing Mechanism of Polycrystalline ZnO. *Appl. Phys. Lett.* **2009**, *95*, 142106.

(33) Park, S.; An, S.; Mum, Y.; Lee, C. UV-Enhanced NO_2 Gas Sensing Properties of SnO_2-Core/ZnO-Shell Nanowires at Room Temperature. *ACS Appl. Mater. Interfaces* **2013**, *5*, 4285-4292.

(34) Kumar, R.; Goel, N.; Kumar, M. High Performance NO_2 Sensor Using MoS_2 Nanowires Network. *Appl. Phys. Lett.* **2018**, *112*, 053502.

(35) Cho, S. Y.; Kim, S. J.; Lee, Y.; Kim, J. S.; Jung, W. B.; Yoo, H. W.; Kim, J.; Jung, H. T. Highly Enhanced Gas Adsorption Properties in Vertically Aligned MoS_2 Layers. *ACS Nano* **2015**, *9*, 9314-9321.

(36) Cho, B.; Hahm, M. G.; Choi, M. S.; Yoon, J.; Kim, A. R.; Lee, Y.; Park, S.; Kwon, J.; Kim, C. S.; Song, M.; Jeong, Y.; Nam, K.; Lee, S.; Yoo, T. J.; Kang, C. G.; Lee, B. H.; Ko, H. C.; Ajayan, P.; Kim, D. H. Charge-Transfer-Based Gas Sensing Using Atomic-Layer MoS_2. *Sci. Rep.* **2015**, *5*, 8052.

(37) Analytical Methods Committee. Recommendations for the Definition, Estimation and Use of the Detection Limit. *Analyst* **1987**, *112*, 199-204.

(38) Lee, K.; Gatensby, K.; McEvoy, N.; Hallam, T.; Duesberg, G. S. High-Performance Sensors Based on Molybdenum Disulfide Thin Films. *Adv. Mater.* **2013**, *25*, 6699-6702.

(39) Popov, I.; Seifert, G.; Tomanek, D. Designing Electrical Contacts to MoS_2 Monolayers: A Computational Study. *Phys. Rev. Lett.* **2012**, *108*, 156802.

(40) Das, S.; Chen, H. Y.; Penumatcha, A. V.; Appenzeller, J. High Performance Multilayer MoS_2 Transistors with Scandium Contacts. *Nano Lett.* **2013**, *13*, 100-105.

(41) Shih, C. J.; Wang, Q. H.; Son, Y.; Jin, Z.; Blankschtein, D.; Strano, M. S. Tuning On-Off Current Ratio and Field-Effect Mobility in a MoS_2-Graphene Heterostructure *via* Schottky Barrier Modulation. *ACS Nano* **2014**, *8*, 5790-5798.

(42) Lee, Y. T.; Choi, K.; Lee, H. S.; Min, S. W.; Jeon, P. J.; Hwang, D. K.; Choi, H.; Im, S. Graphene *Versus* Ohmic Metal as Source-Drain Electrode for MoS_2 Nanosheet Transistor Channel. *Small* **2014**, *10*, 2356-2361.

(43) Yu, Y. J.; Zhao, Y.; Ryu, S.; Brus, L. E.; Kim, K. S.; Kim, P. Tunning the Graphene Work Function by Electric Field Effect. *Nano Lett.* **2009**, *9*, 3430-3434.

(44) Sze, S. M. *Physics of Semiconductor Devices*, Wiley: New York, **1981**.

(45) Koppens, F. H. L.; Mueller, T.; Avouris, P.; Ferrari, A. C.; Vitiello, M. S.; Polini, M. Photodetectors Based on Graphene, Other Two-Dimensional Materials and Hybrid System. *Nat. Nanotechnol.* **2014**, *9*, 780-793.

(46) Fang, H.; Hu, W. Photogating in Low Dimensional Photodetectors. *Adv. Sci.* **2017**, *4*, 1700323.

(47) Joshi, N. V. *Photoconductivity: Art, Science, and Technology*, Marcel Dekker, Inc.: New York: NY, NY, **1990**; Vol. 25, p 309.

(48) Li, G.; Suja, M.; Chen, M.; Bekyarova, E.; Haddon, R. C.; Liu, J. L.; Itkis, M. E. Visible-Blind UV Photodetector Based on Single-Walled Carbon Nanotube Thin Film/ZnO Vertical Heterostructures. *ACS Appl. Mater. Interfaces* **2017**, *9*, 37094-37104.

(49) Furchi, M. M.; Polyushkin, D. K.; Pospischil, A.; Mueller, T. Mechanisms of Photoconductivity in Atomically Thin MoS_2. *Nano Lett.* **2014**, *14*, 6165-6170.

(50) Cho, K.; Min, M.; Kim, T. Y.; Jeong, H.; Pak, J.; Kim, J. K.; Jang, J.; Yun, S. J.; Lee, Y. H.; Hong, W. K.; Lee, T. Electrical and Optical Characterization of MoS_2 with Sulfur Vacancy Passivation by Treatment with Alkanethiol Molecules. *ACS Nano* **2015**, *9*, 8044-8053.

(51) Qiu, H.; Xu, T.; Wang, Z.; Ren, W.; Nan, H.; Ni, Z.; Chen, Q.; Yuan, S.; Miao, F.; Song, F.; Long, G.; Shi, Y.; Sun, L.; Wang, J.; Wang, X. Hopping Transport Through Defect-Induced Localized States in Molybdenum Disulphide. *Nat. Commun.* **2013**, *4*, 2642.

(52) Guo, Y.; Wei, X.; Shu, J.; Liu, B.; Yin, J.; Guan, C.; Han, Y.; Gao, S.; Chen, Q. Charge Trapping at the MoS_2-SiO_2 Interface and its Effects on the Characteristics of MoS_2 Metal-Oxide-Semiconductor Field Effect Transistor. *Appl. Phys. Lett.* **2015**, *106*, 103109.

(53) Illarionov, Y. Y.; Rzepa, G.; Waltl, M.; Knobloch, T.; Grill, A.; Furchi, M. M.; Mueller, T.; Gasser, T. The Role of Charge Trapping in MoS_2/SiO_2 and MoS_2/hBN Field-Effect Transistor. *2D Mater.* **2016**, *3*, 035004.

(54) Schedin, F.; Geim, A. K.; Morozov, S. V.; Hill, E. W.; Blake, P.; Katsnelson, M. I.; Novoselov, K. S. Detection of Individual Gas Molecules Adsorbed on Graphene. *Nat. Mater.* **2007**, *6*, 652-655.

(55) Caffrey, N. M.; Armiento, R.; Yakimova, R.; Abrikosov, I. A. Changes in Work Function due to NO_2 Adsorption on Monolayer and Bilayer Epitaxial Graphene on SiC (0001). *Phys. Rev. B* **2016**, *94*, 205411.

(56) He, Q.; Zeng, Z.; Yin, Z.; Li, H.; Wu, S.; Huang, X.; Zhang, H. Fabrication of Flexible MoS_2 Thin-film Transistor Arrays for Practical Gas-sensing Applications. *Small* **2012**, *8*, 2994-2999.

(57) Deokar, G.; Vancsó , P.; Arenal, R.; Ravaux, F.; Casanov-Cháfer; Llobet, E.; Makarova, A.; Vyalikh, D.; Struzzi, C.; Lambin, P.; Jouiad, M.; Colomer, J. F. MoS_2-Carbon Nanotube Hybrid Material Growth and Gas Sensing. *Adv. Mater. Interfaces* **2017**, *4*, 1700801.

(58) Malekpour, H.; Ramnani, P.; Srinivasan, S.; Balasubramanian, G.; Nika, D. L.; Muchandani, A.; Lake, R. K.; Balandin, A. A. Thermal Conductivity of Graphene with Defects Induced by Electron Beam Irradiation. *Nanoscale* **2016**, *8*, 14608-14616.

CHAPTER 4

MoS_2-Metal Oxide Heterostructure for Enhanced DNA Sensing

4.1 Introduction

The concept of nanotechnology started in mid 1900s and commenced with the breakthrough invention of a scanning tunneling microscope and the discovery of zero-dimensional fullerene in 1980s (Binnig and Rohrer, n.d.). This 0D material paved the way to finding of other dimensional materials such as 1D (carbon nanotubes), 2D (graphene, metal oxides, hexagonal boron nitride). Among these structures, 2D materials have attracted the most interest in a broad spectrum of applications ranging from electronic devices, energy storage, and catalysis (Deng et al., 2016; Mas-Ballesté et al., 2011; Novoselov et al., 2016; Zhang et al., 2018). Due to its high surface-area-to-volume ratio and up to centimeter scale of appreciable lateral size of the nanomaterial, these properties render 2D materials suitable for integrating with current nanofabrication technology and highly favorable for making sensors that rely primarily on surface interaction.(Tao et al., 2017)

Graphene was the first 2D material isolated from its bulk structure in 2004 and has been extensively investigated. Despite its extraordinary properties, such as high optical transparency, thermal conductivity up to 3,000 W $m^{-1}K^{-1}$, high charge carrier concentration, and mobility (Novoselov, 2004), the lack of energy gap between the conduction and valence band in graphene has limited its application in electronic devices. There have been several approaches to engineer a bandgap in graphene; however, most of the successful methods require lengthy processes of fabrication using e-beam lithography or unstable doping treatment with harsh chemicals (Chang et al., 2013; Hu et al., 2018). As a result, these intensive processes negatively impact the amount of charge carrier and increase the concentration of defects in graphene.

This challenge has encouraged researchers to find an alternative 2D material and transition metal dichalcogenides (TMDs), for that reason, have become an emerging field of research. Unlike graphene, TMDs possess a direct bandgap in range of 0.2-3 eV in their single-layer (SL) structure (Xu et al., 2013). This intrinsic band gap suggests that TMDs are more suitable for electronic applications than graphene. One of the most studied TMD compounds is molybdenum disulfide (MoS_2), which consists of one layer of molybdenum atoms in between of two layers of sulfur atoms. SL-MoS_2 exhibits a direct bandgap of 1.87 eV which transitions to an indirect bandgap as the number of layers increases. Therefore, a field-effect transistor (FET) using SL-MoS_2 as a conducting channel expects a high on/off current ratios up to 10^8 and excellent subthreshold swing of 74 mV/decade (Radisavljevic et al., 2011). In addition, due to its planar structure confined to few angstroms thick MoS_2 is ultra-sensitive to minimal perturbation at the surface. These advantages make MoS_2 a great choice of sensing material in FET based biosensors.

In recent years, the concept of label-free immunosensor platform has become intriguing due to its simplicity. In general, a label-free MoS_2 based biosensors require biomolecules to adhere to the surface of MoS_2. This functionalization step can be done via hydrophobic interaction, silanization, and sulfide/disulfide bonding. (J. Lee et al., 2015; Nam et al., 2015; Sim et al., 2015) However, these methods either employ weak van der Waals bonding or significantly rely on the number of defects in MoS_2, which mainly comprises sulfur vacancies. As a result, MoS_2 based biosensors are commonly fabricated using MoS_2 compounds synthesized via chemical/physical exfoliation or hydrothermal reaction. MoS_2 synthesized via these methods produce a large number of defects permitting the direct functionalization. On the other hand, biosensing applications using chemical vapor deposition grown (CVD) MoS_2 are relatively limited due to inadequate number of the defect sites in CVD-MoS_2's crystal lattice. Despite this hinderance, CVD-MoS_2 exhibits such

high crystallinity and potential in mass scale production and hence should deserve more attention in research of sensing applications.

The general mechanism of biosensors is to detect the binding event between an antibody (receptor) and an antigen (target) through electrical signals. Upon the hybridization of a matching biological pair, some perturbation is introduced to sensing channel and hence induces the change in current/resistance or threshold voltage. While several methods of electrical detection, such as voltammetry, amperometry with applied gate (FET characteristic measurement) and without applied gate (chemiresistivity), are available for biosensors using semi-metallic graphene, conductive graphene derivatives and carbon nanotubes (Hatada et al., 2019; Pham et al., 2019; Shen et al., 2019; Terse-Thakoor et al., 2019), MoS_2 based biosensors heavily rely on FET characteristic technique in which a source-drain (SD) current is measured at a constant bias while varying an applied gate voltage to modulate the current. This required gate voltage serves as an amplifier of the small current originated by the nature of low charge mobility in semiconducting MoS_2 and high Schottky barrier at the interface of MoS_2/metal contact. Because the applied back-gating effect plays the key parameter in FET based measurement it requires an adequate contact between MoS_2 and dielectric substrate. A poor contact at the interface can result in a decrease of the gating effect which in turn induces significant reduction of current and thus yields a false positive signal in detection.

In this work, we report a systematic investigation of CVD-MoS_2 based biosensors' stability and the methods to alleviate the device's degradation. We have found that CVD MoS_2 based biosensors degraded during unavoidable incubation step in 10 mM phosphate buffer (pH = 7.4) and deionized water (pH = 7). We conclude the observed degradation was caused by delamination of MoS_2 film from Si/SiO_2 substrate which decreased the gating effect and negated the usage of FET characteristic transfer curve as a mean for detection. This issue was mitigated by stabilizing the

device with a 30 nm thick Al_2O_3 coating. In additional, the oxide layer provided available sites for single stranded DNA (ssDNA)-functionalization via surface chemical functionalization with (3-aminopropyl) triethoxysilane (APTES) and glutaraldehyde. Such sensors demonstrated a great performance to detect mutations in human gene TP53 with high selectivity and a limit of detection at concentrations as low as 10^{-13} M.

4.2 Experimental details

4.2.1 Materials and reagents

Si wafer with a 300 nm thermal grown oxide layer were purchased from Ultrasil, Hayward, California USA. Sulfur powder and molybdenum trioxide MoO_3 were purchased from Sigma Aldrich. Single stranded DNAs including probe, complimentary, and non-complementary DNA were synthesized and purified by Integrated DNA Technologies Inc. The DNA sequences were as follows: aptamer probe: mu.175 complement: 5'-NH_2-$(CH_2)_6$-ATG GTG GGG GCA GTG CCT CAC AAC CTC-3'; perfectly complementary target: mu.175: 5'-GAG GTT GTG AGG CAC TGC CCC CAC CAT-3'; and non-complementary target: 5'-TTT ATG CAT GCA TGC ATG CAT GCA CAT-3'.

4.2.2 Synthesis of MoS_2

MoS_2 was synthesized via CVD method with sulfur and MoO_3 as the precursors and Si/SiO_2 as the substrate. 0.01 g of MoO_3 was centered in a ceramic boat with the Si/SiO_2 substrate positioned on top of the MoO_3 source. This growth took place at the center of a two-zone quartz tube furnace at 650 °C while the tube was saturated with sulfur vapor by heating 0.7 g of sulfur at 170 °C from the upstream. The temperature maintains at 650 °C for complete reaction and the entire system was naturally cooled down to room temperature by removing the tube from the furnace.

4.2.3 Fabrication of FET device

MoS_2 film was isolated from Si/SiO_2 substrate with aid of PS via simple wet etching in 1 M KOH solution. The PS/MoS_2 film was washed several times with deionized (DI) water and transferred on a pre-cleaned Si/SiO_2 substrate. The film was dried in ambient air and annealed at 80 °C for 15 minutes to increase the contact between MoS_2 and Si/SiO_2 substrate. PS layer was removed in toluene at room temperature.

A 10 nm/100 nm Cr/Au was deposited on the silicon side of the Si/SiO_2 as a back gate. The source and drain terminals with a gap size of 10 µm x10 µm were fabricated using a conventional photolithography followed by electron-beam evaporation of 10 nm/100 nm Cr/Au.

4.2.4 Aluminum oxide via atomic layer deposition (ALD)

The deposit took place at 250 °C. Trimethylaluminum (TMA) and water, as precursors, were pulsed in the system periodically for 0.03 seconds. The thickness of the oxide layer was varied by changing the number of cycles, estimated about 1 Å/cycle. 10 nm and 30 nm thick aluminum oxide were grown using 100 and 300 cycles.

4.2.5 Material characterization and measurement

Optical images were taken by Hirox KH-7700 digital microscope and Al_2O_3 thickness was taken by Jobin Yvon UVISEL model M200 Ellipsometer. Both Raman spectra and PL measurements were collected by Horiba LabRam using a green laser (λ = 532 nm) and 100X objective (NA = 0.9). A minimal power of 5 mW was used to avoid local heating and possible damage to the materials. SEM images were taken by a Zeiss STEM. Aluminum oxide layers were deposited using Cambridge Nanotech Savannah 100. FET characteristics curves were obtained by Keithley 2636 system. A constant V_{SD} = 5 V was applied while sweeping the back-gate voltage from 0 V to 40 V.

4.2.6 TP53 detection

The Al_2O_3 passivated MoS_2 based device was incubated in 1 ml of APTES for one hour and washed thoroughly with ethanol. The amine group on APTES then reacted in 4 ml of 25% glutaraldehyde in DI water for two hours. As-prepared device was functionalized with 20 µL of 10^{-6} M NH_2-probe DNA overnight and the reaction was quenched by 20 µL of 10% ethanolamine. For the detection, 20 µL of each concentration of target DNA was incubated for 30 minutes at room temperature and the device was dried using N_2 gun. FET and I-V curves were collected by the Keithley system.

4.3 Results and Discussion

The optical image in **Appx. C1(a)** (**inset)** shows as-grown MoS_2 remained a continuous film after the transfer. The similarity of color contrast across the film illustrates the growth of MoS_2 was uniform and the transfer was residue-free. The film thickness and electrical bandgap of the synthesized MoS_2 were confirmed by different techniques such as Raman spectroscopy, photoluminescence (PL) under a green laser with spot size ≈ 1µm.

The presence of two signature peaks of E_{2g} at 385 cm^{-1} and A_{1g} at 404 cm^{-1} in **Appx. C1(a)** confirms the successful growth of MoS_2. In addition, the difference in wavenumber of 19 cm^{-1} between the two peaks indicates as-grown MoS_2 was single-layer (Li et al., 2012). Due to the intrinsic direct bandgap in single-layer MoS_2 structure, the photoluminescence spectrum in **Appx. C1(b)** shows a significantly high peak at 1.87 eV.

A back-gated field-effect transistor (FET) using such MoS_2 as the conducting channel was prepared using a conventional photolithography process followed by a metal (Cr/Au) deposition. As shown in **Appx. C2**, the FET characteristics curve shows a typical n-type behavior with a high on/off current ratio of 10^4 in ambient condition. Under the applied positive back-gate voltage the device was turned on, i.e dramatic increase in current, due to the accumulation of electrons in MoS_2.

The field-effect mobility was calculated to be 20.5 $cm^2V^{-1}s^{-1}$. This low charge mobility is mainly caused by charge trapping at the interface between the SiO_2 substrate and MoS_2 (Guo et al., 2015; Illarionov et al., 2016) and high contact resistance at metal/MoS_2 interface (Hossain et al., 2015). As a result, electrical measurement methods in MoS_2 based devices are relatively limited to FET characteristics curve with applied gate voltage (D.-W. Lee et al., 2015; Sarkar et al., 2014; Shan et al., 2018).

Due to the significant role of FET measurement in detection, the stability of as-fabricated FET device becomes vital. A stability test was carried out initially in ambient air and later in both bio-compatible media such as phosphate buffer (PB, pH = 7.4) and deionized (DI) water (pH = 7). In **Figure 4.1,** the FET characteristics curve experienced a slight decrease in current after 30 mins in ambient air which was due to the interaction between MoS_2 film and oxidizing gas molecules in air. However, the device was stable after 30 minutes and the FET characteristics curve remained unchanged for additional 90 minute under the same condition.

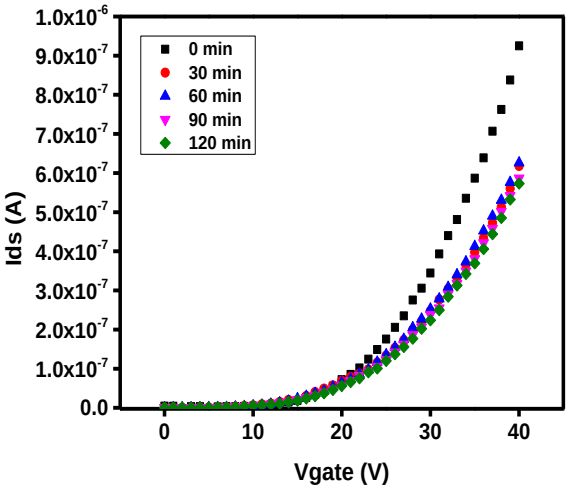

Figure 4.1. Stability of MoS_2 device in ambient air.

On the other hand, device incubated in PB for 30 mins experienced a dramatic decrease in current as seen in **Figure 4.2(a)** and the same behavior was also observed with one in DI water (**Figure 4.2(b)**). Thus, this suggests salt ions in PB solution were not responsible for the observed degradation of the device, but water molecules were, instead, the accountable factor. Three possible mechanisms how water could diminish the performance of FET MoS_2 based device were proposed as below:

(1) Water altered the properties of MoS_2 during the incubation

(2) Water intercalated between gold electrodes and MoS_2 and increased the contact resistance

(3) Water intercalated between MoS_2 and the substrate and decreased the gating effect on the MoS_2 channel.

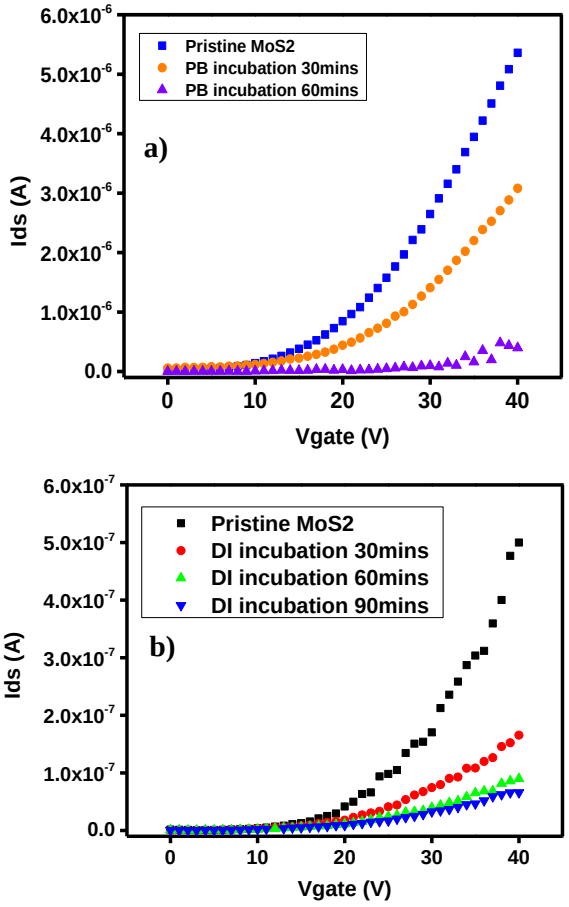

Figure 4.2. FET characteristics curve of MoS_2 based device in (a) PB (pH=7.4) and (b) DI water (pH=7)

Raman spectrometry was employed to examine the properties of MoS_2 after 30-minute incubation in DI water. As seen in **Appx. C3**, the two signature peaks of MoS_2 remained unaffected after the incubation indicating there was no oxidation taking place. As a result, water induced no chemical effect on MoS_2 film, which disregarded mechanism (1).

A thin layer of positive photoresist S1813 was spin-coated on top of the device, and a small photoresist area of 50 x 10 um at the contact of MoS_2 and gold electrodes was removed using photolithographic patterning. An optical image of the actual device can be found in **Appx. C4(a)**. This polymeric layer behaved as a hydrophobic layer that prevented water from inserting between MoS_2 and the Si/SiO_2 substrate but still allowed the possibility of water intercalating between the gold contacts and MoS_2 due to the open area of 50 x 10 um. **Appx. C4(a)** shows the result of FET characteristic curves of pre-photoresist, post-photoresist and after device incubation from 30

minutes to 120 minutes in DI water. As a protecting layer S1813 film minimized interaction between MoS_2 and oxidizing gas molecules in the ambient, such as O_2 and water vapor, and thus increased the performance of FET devices observed by the increase in the FET current. The similar FET transfer curves were collected after 30, 60, 90 and 120 mins indicating the device were relatively stable after the incubation steps. Therefore, this experiment series removed the possibility of mechanism (2) and confirmed mechanism (3) in which water indeed intercalated between conducting channel and the Si/SiO_2 substrate causing the delamination of MoS_2 film. This resulting poor contact between MoS_2 and the dielectric SiO_2 layer decreased the gating effect on the conducting channel in FET measurement yielding the false positive response in detection. In fact, the delamination phenomenon is commonly observed in method of isolation CVD-grown MoS_2 from its growth substrate. Due to the high hydrophobicity of the substrate and MoS_2, water is used as a great medium for a clean, complete lift-off for MoS_2 as reported elsewhere (Gurarslan et al., 2014; Jia et al., 2016).

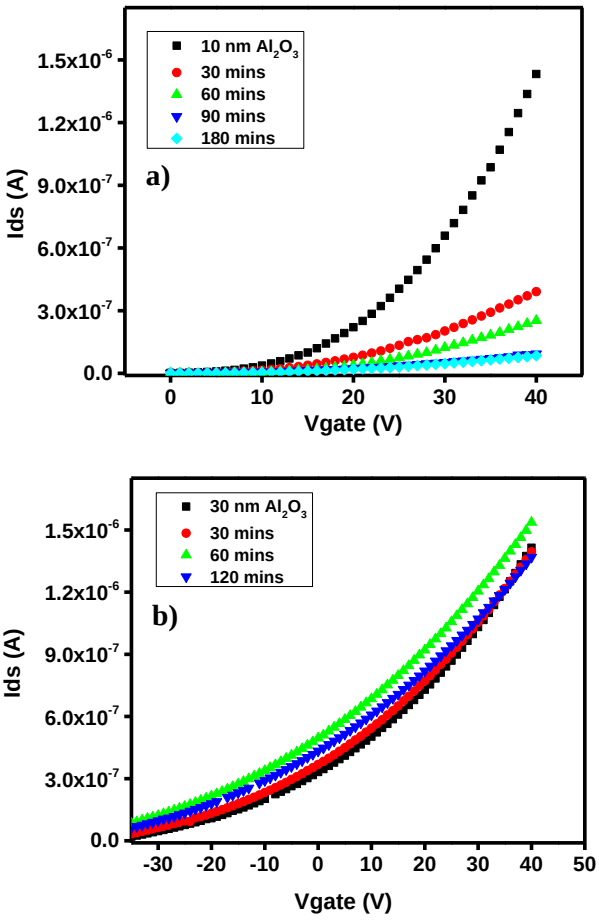

Figure 4.3. FET characteristics curves of the sensor with (a) 10 nm and (b) 30 nm Al_2O_3 after incubation in DI water.

Further investigation on grain boundaries of as-grown CVD MoS_2 was conducted to understand more in depth of the delamination phenomenon that resulted in the instability of MoS_2 based device. Work function of a similar CVD-SL-MoS_2 was measured at 4.90 eV in our previously (Pham et al., 2019) while the absolute potential of Au^{3+} to Au is 5.64 eV. The difference in the work functions created an internal force driving electrons from n-type MoS_2 to Au^{3+} ions and reduced it to Au nanoparticles (NPs). This reduction happened at the reactive sites on MoS_2's lattice concentrated at its edge and grain boundaries (Cao et al., 2015; Sun and Zheng, 2018; Zuo et al., 2017) and hence MoS_2 grain boundaries became distinguishable due the presence of gold NPs. **Appx. C5** shows scanning electron microscopic (SEM) images taken at the same location before and after the incubation of MoS_2 in 5.9 mM $AuCl_3$ solution for 10 minutes. The grain boundaries were indistinguishable but became noticeable after the reduction due to the formation of Au NPs. This indicates as-grown continuous film MoS_2, in fact, consisted of many coalescing MoS_2 crystals. These existing large grain boundaries permitted water molecules to severely penetrate through MoS_2 film and delaminate it from the substrate.

This result renders a passive layer required to prevent the delamination of MoS_2 in an aqueous solution. Although a hydrophobic polymeric layer such as S1813 proved to alleviate the degradation of the FET device its inert to surface chemical modification inhibits the subsequent bio functionalization steps. On the other hand, thin metal oxide layers, such as hafnium oxide, silicon oxide, and aluminum oxide, are well known as passive layers in logic electronics to

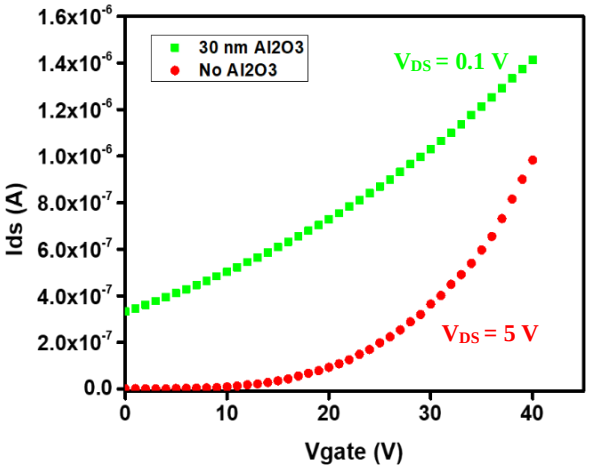

Figure 4.4. FET characteristics curve of MoS_2 based device with and without passive Al_2O_3 layer.

protect the underneath material from being oxidized in the ambient. In addition, the oxide layer in presence of ambient water vapor produced a sufficient number of hydroxyl groups making the device's surface feasible for bio functionalization. In this work, aluminum oxide layer was deposited on the sensor using an ALD method. This deposition involved two steps in which the first step provided hydroxyl seeding by casting water vapor on the SiO_2 surface while the second step was a chemical reaction between OH- groups and TMA to form the Al_2O_3 layer. **Appx. C6** shows the different color contrast of a device between before and after Al_2O_3 deposition which confirmed the successful deposition of oxide layer on the device. The thickness of Al_2O_3 layer on SiO_2 substrate was measured at 30 nm by ellipsometer which can be found in **Appx. C3(b)**. The oxide layer's thickness was optimized by the device's stability after incubation in DI water. **Figure 4.3** demonstrates a device with 10 nm thick Al_2O_3 layer suffered from the degradation. On the other hand, delamination subsided in a device coated by 30 nm thick oxide layer proven by the stable FET transfer curve of the device after 120 minutes. Additionally, a strong n-doping effect of Al_2O_3 onto MoS_2 was noticed in the FET measurement as seen in **Figure 4.4**. Due to the nature of semiconducting properties and relatively large work function, CVD MoS_2 exhibits low charge

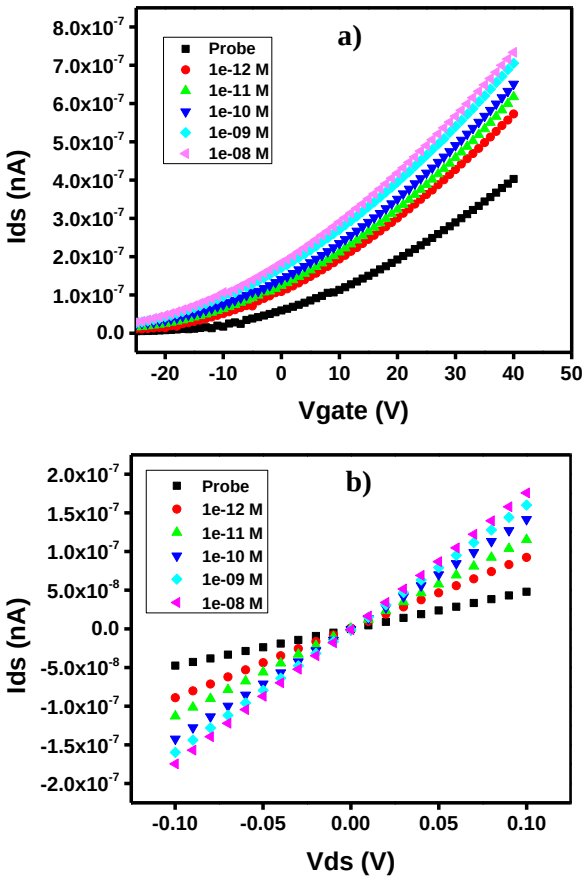

Figure 4.5. FET characteristics curves (a) and I-V curves (b) of Al_2O_3 passivated MoS_2 based sensor for detection of TP53.

mobility and the high contact resistance at MoS_2/gold interface. However, when the device was passivated by Al_2O_3 the insignificant current of $3x10^{-10}$ A at V_g = 0 V was magnified by 1000 times ($3x10^{-7}$ A). Additionally, field-effect charge mobility of as-grown MoS_2 and Al_2O_3-MoS_2 were calculated at 14 $cm^2V^{-1}s^{-1}$ and 367 $cm^2V^{-1}s^{-1}$, respectively. The threshold voltage (V_{TH}) also experienced a shift to a more negative threshold voltage (V_{TH}) proving a strong n-doping effect in MoS_2. We anticipate the two possible reasons including the incomplete oxidation of Al_2O_3 and the passivation of sulfur vacancy defects. During the Al_2O_3 growth, the incomplete reaction between TMA and water vapor resulted to excess positive charged Al^{n+} ions. These resulting positive charges in the oxide layer attracted additional electrons in MoS_2 channel and hence promoted n-doping effect. This led to the appreciable current found in the Al_2O_3 passivated device at V_g=0 V. While as grown CVD MoS_2 exhibited a number of sulfur vacancies at the boundaries and edges as observed in the previous experiment with gold chloride solution. These vacancies created a deep and localized states trapping electrons and hence impaired electron mobility in MoS_2 (Li et al., 2017; Ma et al., 2016). The presence of Al_2O_3 layer allowed its oxygen atoms to fill sulfur vacancies and in turn minimized electrons trapping. Such healing mechanism has been reported previously using other chemicals

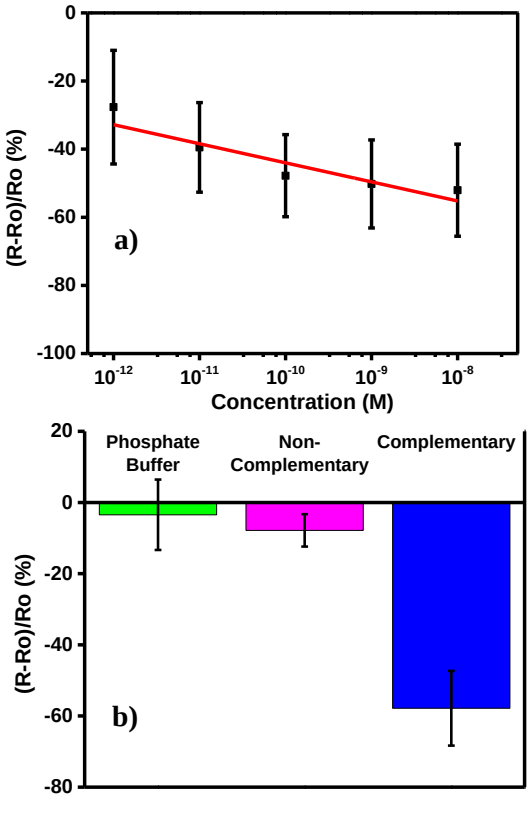

Figure 4.6. Calibration curve (a) and selectivity (b) of Al_2O_3 passivated MoS_2 based sensor to complimentary and non-complimentary ssDNAs.

such as CO, NO, NO_2 and other sulfonate groups (Lu et al., 2018; Ma et al., 2016). This increase in current and charge mobility beneficially provided additional electrical measurement method with less power consumption (no gate and lower V_{DS}) and simpler fabrication due to the elimination of the gate.

As the oxide layers provided available hydroxyl groups on its surface ssDNAs of human gene TP053 were covalently bonded on the device via surface chemical reactions using APTES and glutaraldehyde. Upon the binding to the target ssDNA, additional negatively charged ssDNA accumulated more positive charges in the dielectric Al_2O_3 layer, which in turn attracted the electrons in n-type MoS_2. As a result, there was an increase in current upon target ssDNA's binding as seen in **Figure 4.5(a)**. In addition, due to the strong n-doping effect the oxide layer permitted another measurement method without the need of back gate voltage. I-V measurement at V_g=0 V (no back gate) in **Figure 4.5(b)** shows consistent results with FET measurement. Theoretical limit of detection defined by 3 times the standard deviation of the blank samples (in PB) divided by the slope of the calibration curve plotted in **Figure 4.6(a)** was calculated to be 5.3 x 10^{-13} M. **Figure 4.6(b)** illustrates such device showed a response seven times higher to the target DNA than a non-complementary ssDNA at the same concentration thus concluding the device has a good selectivity. It is worth noting that the current in DNA detection increased which opposed to the decrease in current observed in device's degradation event.

4.4 Conclusion

In conclusion, this work presents an extended deliberation for electrical measurement analysis of biosensors. Although the sensitivity aspect of a biosensor is intensively researched, the device's accuracy, specifically in an event of false positive response, should be equally considered. CVD grown MoS_2 due to the nature of its process of synthesis forms a large number of grain boundaries and a device using such materials, as a result, suffers from delamination of the material from the

substrate. A facile growth of aluminum oxide layer using ALD has been proven to alleviate the degradation of the sensor in aqueous media and the sensor also benefits from the n-doping effect by the oxide layer creating additional less-power consumption method of detection. This metal oxide passivated device not only exhibits a higher stability but also demonstrates high sensitivity and selectivity.

4.5 References

(1) Binnig, G.; Rohrer, H. SCANNING TUNNELING MICROSCOPY. 9.

(2) Deng, D.; Novoselov, K. S.; Fu, Q.; Zheng, N.; Tian, Z.; Bao, X. Catalysis with Two-Dimensional Materials and Their Heterostructures. *Nature Nanotech* **2016**, *11* (3), 218–230. https://doi.org/10.1038/nnano.2015.340.

(3) Mas-Ballesté, R.; Gómez-Navarro, C.; Gómez-Herrero, J.; Zamora, F. 2D Materials: To Graphene and Beyond. *Nanoscale* **2011**, *3* (1), 20–30. https://doi.org/10.1039/C0NR00323A.

(4) Novoselov, K. S.; Mishchenko, A.; Carvalho, A.; Castro Neto, A. H. 2D Materials and van Der Waals Heterostructures. *Science* **2016**, *353* (6298), aac9439. https://doi.org/10.1126/science.aac9439.

(5) Zhang, P.; Wang, F.; Yu, M.; Zhuang, X.; Feng, X. Two-Dimensional Materials for Miniaturized Energy Storage Devices: From Individual Devices to Smart Integrated Systems. *Chem. Soc. Rev.* **2018**, *47* (19), 7426–7451. https://doi.org/10.1039/C8CS00561C.

(6) Tao, L.; Chen, K.; Chen, Z.; Chen, W.; Gui, X.; Chen, H.; Li, X.; Xu, J.-B. Centimeter-Scale CVD Growth of Highly Crystalline Single-Layer MoS_2 Film with Spatial Homogeneity and the Visualization of Grain Boundaries. *ACS Applied Materials & Interfaces* **2017**, *9* (13), 12073–12081. https://doi.org/10.1021/acsami.7b00420.

(7) Novoselov, K. S. Electric Field Effect in Atomically Thin Carbon Films. *Science* **2004**, *306* (5696), 666–669. https://doi.org/10.1126/science.1102896.

(8) Chang, C.-K.; Kataria, S.; Kuo, C.-C.; Ganguly, A.; Wang, B.-Y.; Hwang, J.-Y.; Huang, K.-J.; Yang, W.-H.; Wang, S.-B.; Chuang, C.-H.; et al. Band Gap Engineering of Chemical Vapor Deposited Graphene by *in Situ* BN Doping. *ACS Nano* **2013**, *7* (2), 1333–1341. https://doi.org/10.1021/nn3049158.

(9) Hu, Y.; Xie, P.; De Corato, M.; Ruini, A.; Zhao, S.; Meggendorfer, F.; Straasø, L. A.; Rondin, L.; Simon, P.; Li, J.; et al. Bandgap Engineering of Graphene Nanoribbons by Control over Structural Distortion. *Journal of the American Chemical Society* **2018**, *140* (25), 7803–7809. https://doi.org/10.1021/jacs.8b02209.

(10) Xu, M.; Liang, T.; Shi, M.; Chen, H. Graphene-Like Two-Dimensional Materials. *Chemical Reviews* **2013**, *113* (5), 3766–3798. https://doi.org/10.1021/cr300263a.

(11) Lee, J.; Dak, P.; Lee, Y.; Park, H.; Choi, W.; Alam, M. A.; Kim, S. Two-Dimensional Layered MoS2 Biosensors Enable Highly Sensitive Detection of Biomolecules. *Scientific Reports* **2015**, *4* (1). https://doi.org/10.1038/srep07352.

(12) Nam, H.; Oh, B.-R.; Chen, P.; Chen, M.; Wi, S.; Wan, W.; Kurabayashi, K.; Liang, X. Multiple MoS2 Transistors for Sensing Molecule Interaction Kinetics. *Scientific Reports* **2015**, *5* (1). https://doi.org/10.1038/srep10546.

(13) Sim, D. M.; Kim, M.; Yim, S.; Choi, M.-J.; Choi, J.; Yoo, S.; Jung, Y. S. Controlled Doping of Vacancy-Containing Few-Layer MoS_2 *via* Highly Stable Thiol-Based Molecular Chemisorption. *ACS Nano* **2015**, *9* (12), 12115–12123. https://doi.org/10.1021/acsnano.5b05173.

(14) Hatada, M.; Tran, T.-T.; Tsugawa, W.; Sode, K.; Mulchandani, A. Affinity Sensor for Haemoglobin A1c Based on Single-Walled Carbon Nanotube Field-Effect Transistor and Fructosyl Amino Acid Binding Protein. *Biosensors and Bioelectronics* **2019**, *129*, 254–259. https://doi.org/10.1016/j.bios.2018.09.069.

(15) Pham, T.; Ramnani, P.; Villarreal, C. C.; Lopez, J.; Das, P.; Lee, I.; Neupane, M. R.; Rheem, Y.; Mulchandani, A. MoS2-Graphene Heterostructures as Efficient Organic Compounds Sensing 2D Materials. *Carbon* **2019**, *142*, 504–512. https://doi.org/10.1016/j.carbon.2018.10.079.

(16) Shen, Y.; Tran, T.-T.; Modha, S.; Tsutsui, H.; Mulchandani, A. A Paper-Based Chemiresistive Biosensor Employing Single-Walled Carbon Nanotubes for Low-Cost, Point-of-Care Detection. *Biosensors and Bioelectronics* **2019**, *130*, 367–373. https://doi.org/10.1016/j.bios.2018.09.041.

(17) Terse-Thakoor, T.; Ramnani, P.; Villarreal, C.; Yan, D.; Tran, T.-T.; Pham, T.; Mulchandani, A. Graphene Nanogap Electrodes in Electrical Biosensing. *Biosensors and Bioelectronics* **2019**, *126*, 838–844. https://doi.org/10.1016/j.bios.2018.11.049.

(18) Li, H.; Zhang, Q.; Yap, C. C. R.; Tay, B. K.; Edwin, T. H. T.; Olivier, A.; Baillargeat, D. From Bulk to Monolayer MoS2: Evolution of Raman Scattering. *Advanced Functional Materials* **2012**, *22* (7), 1385–1390. https://doi.org/10.1002/adfm.201102111.

(19) Guo, Y.; Wei, X.; Shu, J.; Liu, B.; Yin, J.; Guan, C.; Han, Y.; Gao, S.; Chen, Q. Charge Trapping at the MoS_2-SiO_2 Interface and Its Effects on the Characteristics of MoS_2 Metal-Oxide-Semiconductor Field Effect Transistors. *Applied Physics Letters* **2015**, *106* (10), 103109. https://doi.org/10.1063/1.4914968.

(20) Illarionov, Y. Y.; Rzepa, G.; Waltl, M.; Knobloch, T.; Grill, A.; Furchi, M. M.; Mueller, T.; Grasser, T. The Role of Charge Trapping in MoS_2/SiO_2 and MoS_2/HBN Field-Effect

Transistors. *2D Materials* **2016**, *3* (3), 035004. https://doi.org/10.1088/2053-1583/3/3/035004.

(21) Hossain, M.; Sanaullah, M.; Abdul Hamid Bin Yousuf; Es-Saki, A.; Chowdhury, M. H. Analytical Analysis of the Contact Resistance (Rc) of Metal-MoS2 Interface. In *2015 IEEE 58th International Midwest Symposium on Circuits and Systems (MWSCAS)*; IEEE: Fort Collins, CO, USA, 2015; pp 1–4. https://doi.org/10.1109/MWSCAS.2015.7282027.

(22) Lee, D.-W.; Lee, J.; Sohn, I. Y.; Kim, B.-Y.; Son, Y. M.; Bark, H.; Jung, J.; Choi, M.; Kim, T. H.; Lee, C.; et al. Field-Effect Transistor with a Chemically Synthesized MoS2 Sensing Channel for Label-Free and Highly Sensitive Electrical Detection of DNA Hybridization. *Nano Research* **2015**, *8* (7), 2340–2350. https://doi.org/10.1007/s12274-015-0744-8.

(23) Sarkar, D.; Liu, W.; Xie, X.; Anselmo, A. C.; Mitragotri, S.; Banerjee, K. MoS $_2$ Field-Effect Transistor for Next-Generation Label-Free Biosensors. *ACS Nano* **2014**, *8* (4), 3992–4003. https://doi.org/10.1021/nn5009148.

(24) Shan, J.; Li, J.; Chu, X.; Xu, M.; Jin, F.; Wang, X.; Ma, L.; Fang, X.; Wei, Z.; Wang, X. High Sensitivity Glucose Detection at Extremely Low Concentrations Using a MoS $_2$ -Based Field-Effect Transistor. *RSC Adv.* **2018**, *8* (15), 7942–7948. https://doi.org/10.1039/C7RA13614E.

(25) Gurarslan, A.; Yu, Y.; Su, L.; Yu, Y.; Suarez, F.; Yao, S.; Zhu, Y.; Ozturk, M.; Zhang, Y.; Cao, L. Surface-Energy-Assisted Perfect Transfer of Centimeter-Scale Monolayer and Few-Layer MoS $_2$ Films onto Arbitrary Substrates. *ACS Nano* **2014**, *8* (11), 11522–11528. https://doi.org/10.1021/nn5057673.

(26) Jia, H.; Yang, R.; Nguyen, A. E.; Alvillar, S. N.; Empante, T.; Bartels, L.; Feng, P. X.-L. Large-Scale Arrays of Single- and Few-Layer MoS $_2$ Nanomechanical Resonators. *Nanoscale* **2016**, *8* (20), 10677–10685. https://doi.org/10.1039/C6NR01118G.

(27) Cao, W.; Pankratov, V.; Huttula, M.; Shi, X.; Saukko, S.; Huang, Z.; Zhang, M. Gold Nanoparticles on MoS2 Layered Crystal Flakes. *Materials Chemistry and Physics* **2015**, *158*, 89–95. https://doi.org/10.1016/j.matchemphys.2015.03.041.

(28) Sun, L.; Zheng, J. Optical Visualization of MoS2 Grain Boundaries by Gold Deposition. *Science China Materials* **2018**, *61* (9), 1154–1158. https://doi.org/10.1007/s40843-018-9233-9.

(29) Zuo, P.; Jiang, L.; Li, X.; Li, B.; Xu, Y.; Shi, X.; Ran, P.; Ma, T.; Li, D.; Qu, L.; et al. Shape-Controllable Gold Nanoparticle–MoS $_2$ Hybrids Prepared by Tuning Edge-Active Sites and Surface Structures of MoS $_2$ via Temporally Shaped Femtosecond Pulses. *ACS Applied Materials & Interfaces* **2017**, *9* (8), 7447–7455. https://doi.org/10.1021/acsami.6b14805.

(30) Li, L.; Long, R.; Bertolini, T.; Prezhdo, O. V. Sulfur Adatom and Vacancy Accelerate Charge Recombination in MoS $_2$ but by Different Mechanisms: Time-Domain Ab Initio Analysis. *Nano Lett.* **2017**, *17* (12), 7962–7967. https://doi.org/10.1021/acs.nanolett.7b04374.

(31) Ma, D.; Wang, Q.; Li, T.; He, C.; Ma, B.; Tang, Y.; Lu, Z.; Yang, Z. Repairing Sulfur Vacancies in the MoS_2 Monolayer by Using CO, NO and NO_2 Molecules. *J. Mater. Chem. C* **2016**, *4* (29), 7093–7101. https://doi.org/10.1039/C6TC01746K.

(32) Lu, H.; Kummel, A.; Robertson, J. Passivating the Sulfur Vacancy in Monolayer MoS_2. *APL Materials* **2018**, *6* (6), 066104. https://doi.org/10.1063/1.5030737.

CHAPTER 5

Flexible MoS_2-graphene based Wearable Gas Sensors

5.1 Introduction

Public health is always one of major society's concerns, and the emergence of many diseases has been causing human's significant unease. One of the most effective way to mitigate the anxiety about sudden illness is frequent medical monitoring. Nowadays, diagnosis work can be achieved accurately at medical centers and, hence, proper treatments can be provided during early stages of diseases. However, healthcare services are limited and are mainly not available for homecare. Furthermore, diagnosis often requires lengthy and costly processes. As a result, patients, especially ones in developing areas, may suffer from ineffective and delayed treatments. In addition, the costly medical instrument and its maintenance services become one of the main challenges to both medical facilities and patients, which further delays the diagnosis and the treatment of diseases. For example, chronic wound, defined as any wounds that do not heal within several (~ 4) weeks, is globally prevalent. In the United State alone, approximately 6.5 million patients are afflicted by the disease, which includes traumatic wounds, pressure ulcers, and most commonly, diabetic ulcers.[1] The treatment of chronic wounds requires daily monitoring and drug administration, imposing significant healthcare costs. Current treatments typically use qualitative measures by healthcare practitioners, leading to an incorrect assessment of the disease status. Topical drug administration with wound dressing is often used to treat chronic open wounds, but the efficacy of such a treatment is very low due to the insufficiently accurate wound monitoring. Thus, this recommends another automated and low-cost method of monitoring.

Traditional chemical (gas) sensors are abundantly fabricated on rigid and brittle substrate materials, in which silicon-based substrate is the most common one.[2–5] Even though these types of

sensors have been widely used, they are not compatible with curvilinear and soft human bodies, making the sensors not available for wearable applications to measure human physiology. In the recent years, emerging Internet of Things (IoTs) have developed various configurations for wearable sensors to monitor human's conditions including heart and breath rate, wrist pulse, facial expression and vocalization etc.[6–9] These sensors are miniaturized and fabricated on different flexible substrates which are readily attached on human's skin for continual detection. Current flexible electronic technology usually suffers from the device's short lifetime due to continuous physical bending and/or stretching processes.[10–12] Despite the current challenges, wearable electronics exhibit superior advantages and have tremendous potential in the state-of-the art sensing technology.

In this work, we investigated the potential application of 2D graphene/MoS_2 heterostructure based flexible device for nitrogen dioxide and nitric oxide detection. The devices were fabricated on a commercial flexible polyimide (PI) Kapton film using graphene as electrodes and MoS_2 as a conducting/sensing channel. Due to the absence of dangling bonds at the surface, graphene provides a pristine flat 2D contact with MoS_2 channel and, thus, mitigates the contact resistance.[13–15] In addition, the tunability of work function in graphene reduces the Schottky barrier at the channel/contact interface and results in an increase in the sensing signal.[3,16] A red light with photon energy matching the bandgap in single-layer (SL) MoS_2 was employed to further enhance the sensitivity of the sensors.[16] Nitrogen dioxide and nitric oxide were chosen as the analyte gases due to their negative impacts on human health.[5,17] Additionally, NO, in medical field, plays an important role in different stages of wound healing including angiogenesis, collagen deposition, and keratinocyte proliferation.[18,19] Therefore, the ability to detect NO at low concentration using flexible electronic sensors demonstrates a great potential of the devices in efficient diagnosis of wound healing process.

5.2 Experimental Details

5.2.1 MoS_2 growth

MoS_2 films were chemical vapor deposition (CVD) grown on SiO_2/Si substrate. Sulfur and molybdenum trioxide (MoO_3) powders were the precursors. Sulfur contained in a ceramic boat was located in the upstream where the temperature was controlled by a heating jacket while MoO_3 was located inside the furnace. The tube was pre-saturated by sulfur vapor at 170 °C, then MoS_2 growth took place in the furnace at 650 °C for 10 minutes. After the growth was complete, the system was naturally cooled to room temperature by removing the tube from the furnace.

5.2.2 Graphene growth

In brief, CVD graphene was grown on a 2x5 cm^2 piece of polycrystalline copper foil. The copper foil was annealed 1030 °C in presence of H_2 (10 sccm) and argon (300 sccm) for 2 hours in order to create a smooth homogenous surface. Diluted CH_4 in argon (90 ppm) was introduced for 1 hour at a flowrate of 375 sccm while H_2 flow remained unchanged. After the growth was complete, the furnace was turned off and the entire system was cooled to room temperature under H_2 (10 sccm) and argon (300 sccm).

5.2.3 Device preparation

Gold contact were fabricated on Kapton wafer using a conventional photolithography. A 5 nm/50 nm thin Cr/Au film was deposited using electron-beam metal evaporator and the metal lift-off was done in acetone at room temperature. PMMA/graphene film was transferred on the patterned gold contacts and PMMA was sufficiently removed in acetone at 60 °C for 2 hours. Due to an unavailable shadow mask, another step of photolithography was employed to pattern graphene film into electrode geometry using a reversal image technique. Photoresist was then removed in acetone with aid of 5 times one-second pulse of ultrasonication. After the photoresist was lifted off

completely, PS/MoS_2 film was transferred on the graphene electrodes. The polymeric layer was removed in polystyrene at room temperature.

5.2.4 Material and device characterization

Raman and PL spectra were collected on Horiba LabRam system using a green laser with wavelength of 532 nm and 100x objective (NA=0.9). The power of the laser beam was fixed at 5 mW to avoid local damage to the materials. Optical image was taken with Hirox KH-7700 digital microscope.

5.2.5 Electrical measurements, and gas sensing experiments

The current-voltage (I-V) measurement was conducted utilizing a Keithley 236 source-measure unit. The instruments control and data acquisition for all the measurements were conducted utilizing Labview hardware and software. For gas sensing measurements the red LED (model L10762, Hamamatsu Photonics) with the central wavelength of 660 nm was integrated with the gas sensing PDMS chamber. The LED was powered by applied a constant DC bias of 5 V.

For gas sensing experiments, the concentrations of NO_2 and NO gases were regulated by two Alicat Scientific mass flow controllers: one to control a flow of 99.99% pure N_2 gas and the other to control a flow of 10 ppm NO_2 or 500 ppb NO in N_2. The total flowrate to the sensing chamber remained constant at 400 sccm.

In the experiment of interference of humidity, a bubbler was used to create a relative humidity environment (RH). Different RH levels was obtained by mixing a 100% RH from the bubbler with another incoming N_2 stream. The total flowrate was fixed at 400 sccm.

5.3 Results and Discussion

In this work, MoS_2 and graphene films were characterized using the same method that was reported in the previous chapters. However, graphene growth was prolonged to one hour, instead of 20-30 minutes, to ensure a continuous large-area film for the fabrication of graphene electrodes.

Polyimide (PI), or so-called Kapton film, was chosen as the flexible substrate due to its relatively high transparency, excellent properties under physical stresses, high resistance and good compatibility to chemicals (**Table 5.1**).[20]

Kapton films are commercialized in different thickness ranging from 25, 50, 75 and 125 μm categorized as 1, 2, 3, 5 MIL, respectively. Due to the necessity of device's transparency for optoelectronic applications, 1MIL (25 μm thin) and 2 MIL (50 μm thin) films were selected as our experimental flexible substrates. In addition, thinner films offer a higher flexibility for on-skin device applications. Due to commercial-grade Kapton film's poor roughness and high insulating properties, all spectroscopic characterization of MoS_2 and graphene including Raman, PL were done on SiO_2/Si prior than using the same-quality materials on Kapton substrates.

Table 5.1 Physical properties of different Kapton films [20]

	Tensile strength Carbon steel (AISI 1018) : 370 MPA				
PROPERTY	1 MIL	2 MIL	3 MIL	5 MIL	TEST METHOD
Ultimate Tensile Strength at 73°F, Mpa	231	231	231	231	ASTM D-882-91, Method A*
Ultimate Tensile Strength at 392°F, Mpa	139	139	139	139	ASTM D-882-91, Method A*
Ultimate Elongation at 73°F, %	72	82	82	82	ASTM D-882-91, Method A
Ultimate Elongation at 392°F, %	83	83	83	83	ASTM D-882-91, Method A
Density, g/cc	1.42	1.42	1.42	1.42	ASTM D-1505-90
Tensile Modulus at 73°F, GPa	2.5	2.5	2.5	2.5	ASTM D-882-91, Method A
Tensile Modulus at 392°F, GPa	2.0	2.0	2.0	2.0	ASTM D-882-91, Method A

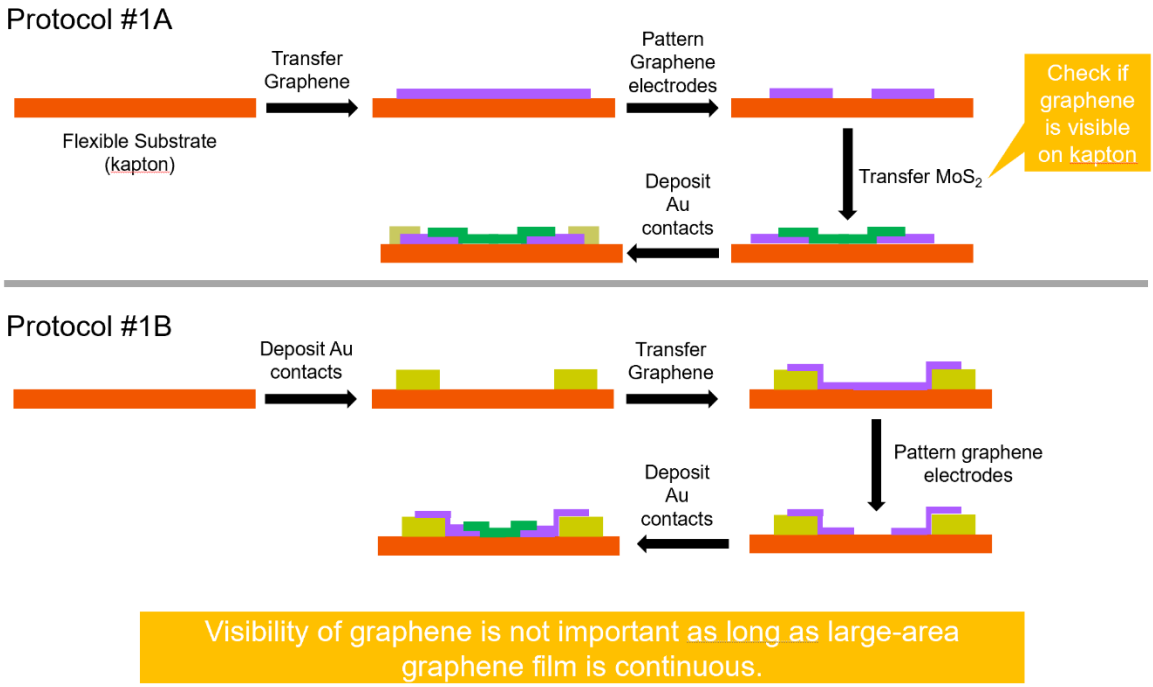

Figure 5.1 Two Fabrication Protocols of MoS_2/graphene heterostructure on Kapton.

Two device fabrication protocols (Protocol 1A and Protocol 1B) were proposed in **Figure 5.1** based on the optimal process's complication, material's contrast and transparency on Kapton substrates.

Protocol 1A and Protocol 1B are conceptually similar; however, Protocol 1A is more explicit but vitally replies on the high contrast of graphene on Kapton substrate, which is not essential in Protocol B. As seen in **Figure 5.2**, graphene has extremely low contrast on Kapton substrate and, hence, confirms that Protocol #1B is more feasible. Kapton substrate was tested for compatibility with conventional lithographical processes using baking, UV exposure, photoresist, developer, and metal deposition. **Figure**

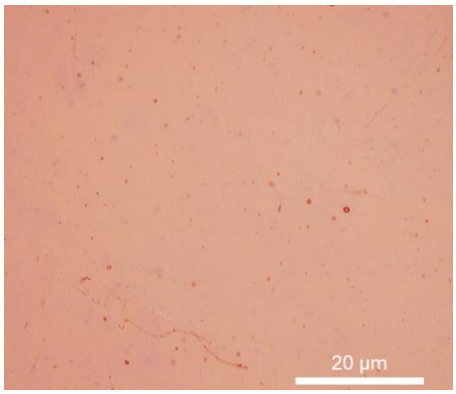

Figure 5.2 Low contrast of graphene film on Kapton.

5.3 (inset) of a fully fabricated device shows that Kapton films withstand the lithographic processes, provide excellent adhesion with metals and are compatible for scaling up.

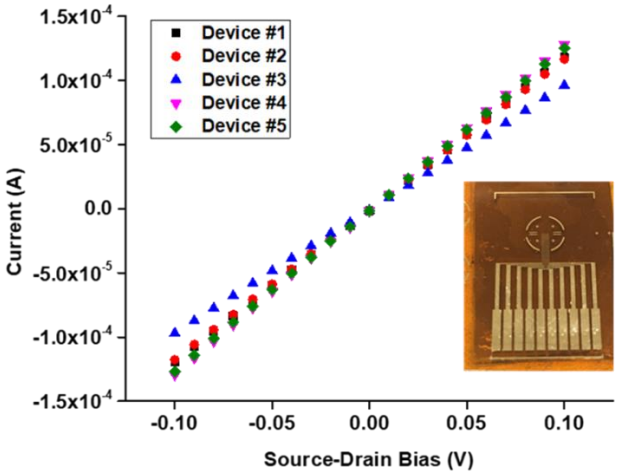

Figure 5.3 Low contrast of graphene film on Kapton.

Firstly, graphene film was transferred onto pre-patterned gold contacts. The linearity of I-V curves in **Figure 5.3** shows that graphene film had an Ohmic contact with the source-drain terminals. Due to the semimetallic properties, graphene film, as conducting channel, exhibits low resistance and, hence, high current in electrical devices.

Graphene film was then patterned in graphene electrode using the reversal image photolithographic technique. The excess area of graphene was removed using a reactive ion etching, in which O_2 plasma was used as the main etchant. After patterning, graphene was no longer

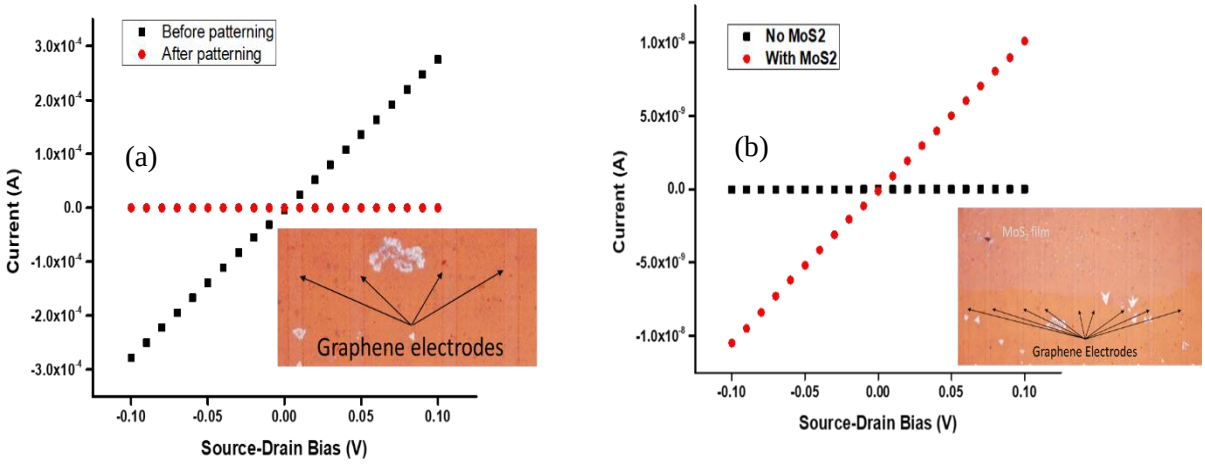

Figure 5.4 I-V measurement of (a) Graphene before and after etching (b) Before and after MoS_2 transfer.

the conducting channel and, hence, no current was observed under the applied bias of 5 V (**Figure 5.4(a)**). This was to confirm the lithography of making graphene into electrodes was successful.

MoS_2 films, after isolated from its growth substrate, were transferred on graphene electrodes to complete the sensing device. It is noticed that SL MoS_2 films of 7-9 Å thick, which are 3 times thicker than SL graphene layers, make the films distinguishable on Kapton substrates (**Figure 5.4(b) (inset)**). Due to its high contrast, the fabrication process became more straightforward.

Due the nature of semiconducting MoS_2, the device experienced a high resistance, which can be attributed to the low charge mobility in MoS_2 and the Schottky barrier at the contact/channel interface. However, the device showed an evident current under an applied source-drain bias (**Figure 5.4(b)**).

In light of fabricating on-skin flexible electronic devices to detect NO_2 and NO, we created a flexible polydimethylsiloxane (PDMS) gas chamber, where the gas can be. Due to the transparency

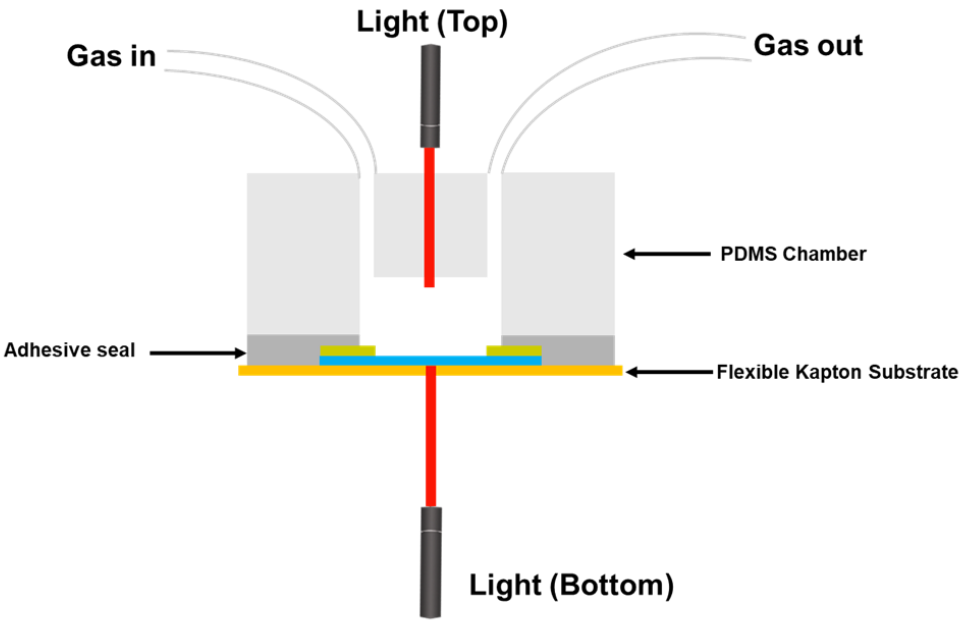

Figure 5.5 Schematics of flexible gas sensor with a flexible PDMS gas chamber.

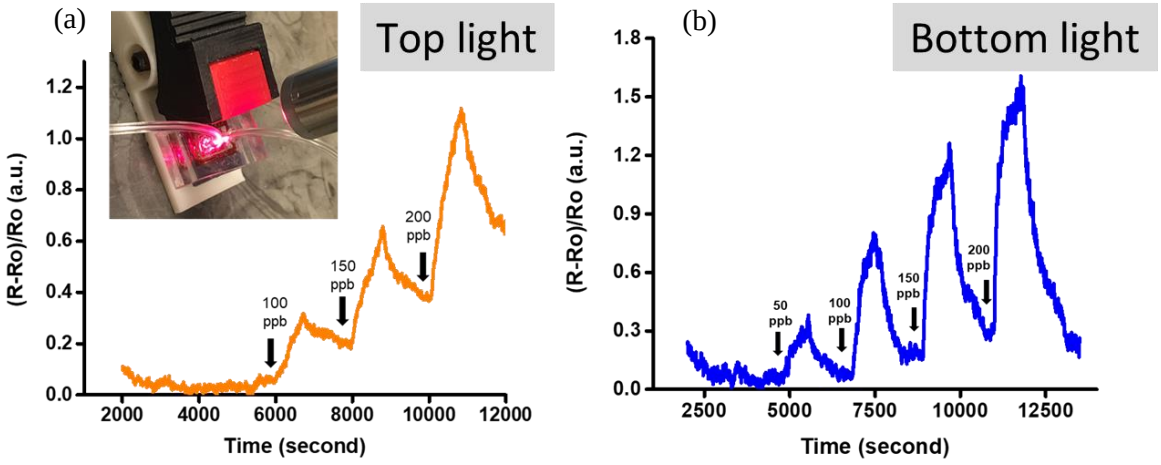

Figure 5.6 NO_2 gas sensing with red light illuminated from (a) the top, inset shows the actual experimental set up; (b) the back.

of the PDMS chamber, the optoelectronic sensors are available for both light excitation from the top and the bottom of the device, as seen in **Figure 5.5**

Figure 5.6 shows the sensing activity of the device under light excitation from top and the bottom of the device. Both configurations showed an appreciable response to different NO_2

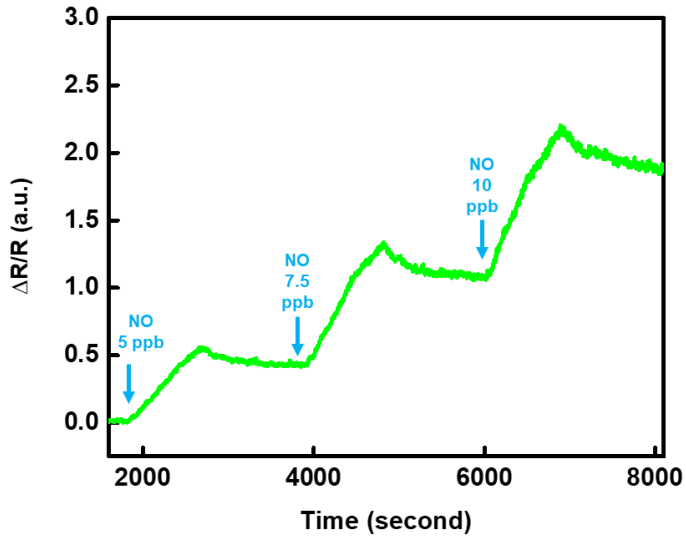

Figure 5.7 NO gas sensing at concentration of 5, 7.5, 10 ppb with red light illuminated from the top.

concentrations and confirmed our sensors exhibited an n-type behavior. NO_2 is well-recognized as an electron withdrawn molecule. Therefore, upon binding to the n-type MoS_2 sensing channel, it induces a decrease in number of electrons in MoS_2 and, in turn, decreases the current. The sensing response using the back-light excitation demonstrated a lower detection limit and better recovery than the one using the top light excitation. This can be attributed to the fact that due to the absence of the thick PMDS chamber the light had better penetration and hence inflicted more effects on the gas sensor mechanism.

Similarly, NO gas was detected at low concentrations of 5, 7.5, 10 ppb. The desired concentrations were obtained by diluting the initial concentration of 500 ppb NO in total gas flow rate of 400 sccm with balance of N_2 gas. The sensor showed a significant response to a concentration of NO as low as 5 ppb, confirming the high potential application of such sensors in detection of NO (**Figure 5.7)**.

Despite the high sensitivity of the device, the experimental results showed that the devices suffered from an incomplete recovery step and, hence, resulted in an electrical drift. Even though the drift can be recalibrated, it can complicate the electrical and logical outputs. Previously, use of

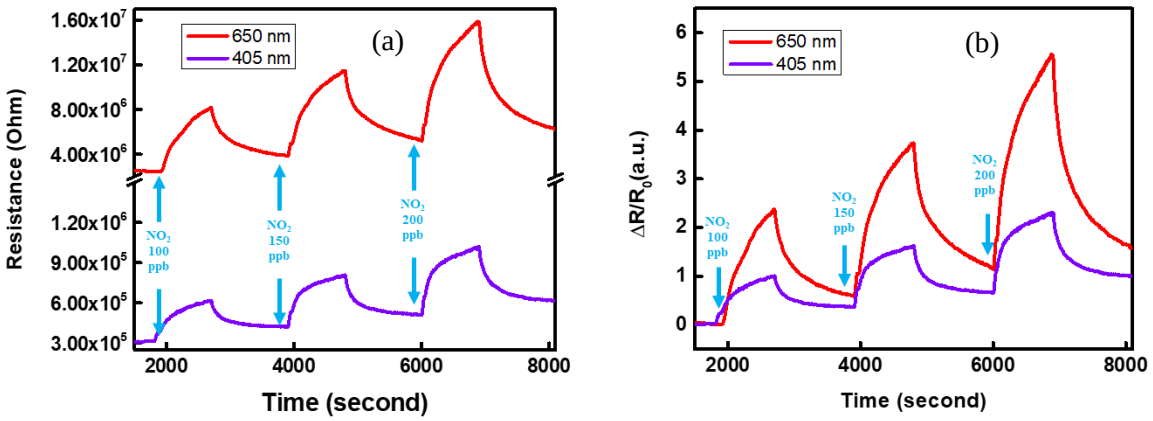

Figure 5.8 NO_2 gas detection (a) linear scale (b) normalized scale using red (λ = 650 nm) and violet (λ = 405 nm) light illuminated from the top.

UV light was reported to improve the recovery of gas sensors.[21–24] However, due to a risk of causing mutations in human, UV light is not compatible for on-skin applications. We attempted to replace UV light with a visible violet light (λ = 405 nm) to study effects of the light wavelength in gas detection.

Figure 5.8(a) and 5.8(b) show the linear and normalized response of the device to NO_2 gas, respectively, under red and violet light excitation. Violet light exhibits a wavelength of 405 nm and, thus, possesses higher photon energy than red light (λ = 650 nm). This higher photon energy results in more photogenerated electrons in the MoS_2's conduction band, i.e. higher current (lower resistance). Indeed, the device under violet light illumination experienced a lower resistance, in range of $10^5\,\Omega$ as compared to $10^6\,\Omega$ under red light. However, the normalized plot confirms there was no significant advantage of using violet light due the persistent presence of incomplete recovery and low sensitivity towards NO_2.

The insignificant difference in sensing signal by using different wavelengths of light was more profound when the gas concentration was in a lower range of few ppb of NO, as seen in **Figure 5.9**. This can be understood that low gas concentrations result in significantly lower number of gas

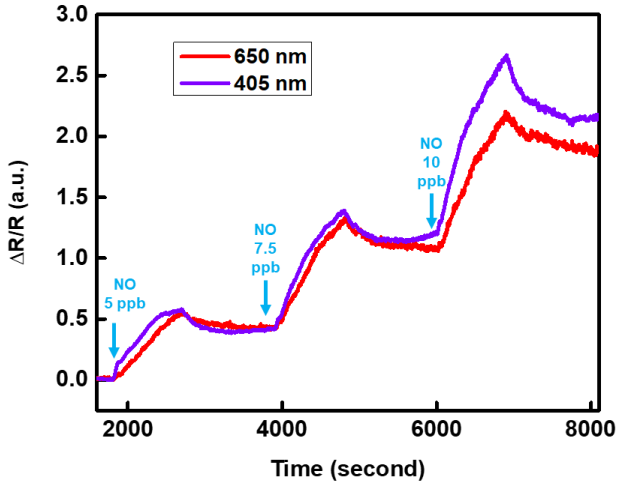

Figure 5.9 No significant difference in NO gas detection using red (λ = 650 nm) and violet (λ = 405 nm) light illuminated from the top.

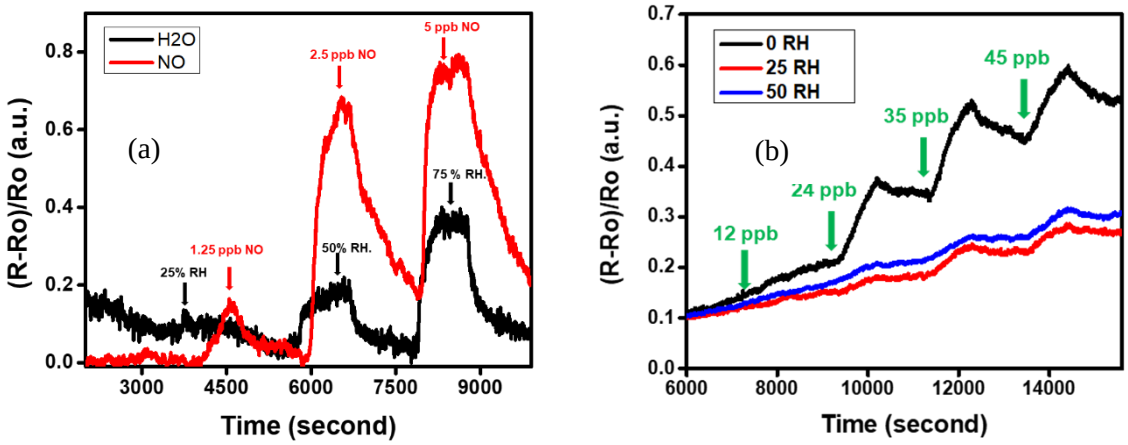

Figure 5.10 Humidity interference studies (a) response to humidity as compared to NO; (b) response to NO in different RH levels.

molecules than the available electrons in the MoS_2 channel. Even though the higher-energy violet light produced additional electrons into MoS_2's conduction band than the red light, the excess electrons became futile during the interaction with the gas molecules. As a result, there was no significant difference in detection at low gas concentrations.

One of the major concerns in chemical sensing is humidity interference.[25,26] While rigid gas sensors suffer from the competing response of humidity from water vapor in the ambient, flexible and on-skin device's performance diminishes due to the presence of humidity exhausted from human body via sweat, breath etc. A systematic experiments were done to study the effect of humidity to our devices, including observing the response of different relative humidity levels and the response of the analyte gases under these humidity conditions.

Figure 5.10 shows that humidity inflicted a similar effect on the device, as compared to NO_2 and NO. However, the magnitude of the response was 2-3 times lower than the response by the analytes (50% RH vs 2.5 ppb NO and 75 % RH vs 5 ppb NO). Additionally, when the analytes were detected in presence of humidity, the response of the device to the analytes decreased as RH levels increased. We conclude that the response of the device to the analytes and humidity is not

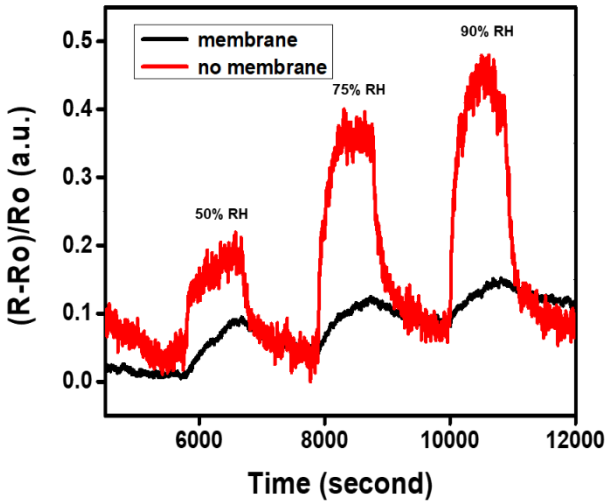

Figure 5.11 Humidity interference study with an incorporated hydrophobic membrane.

additive but, instead, involves a complicated mechanism, in which the analyte gas molecules competes against water molecules to migrate onto the surface of the sensing material. As a result, we attempted to integrate a hydrophobic membrane on the device to alleviate the effect of humidity. **Figure 5.11** confirms the membrane, in fact, mitigated the effect of water molecules on the sensing performance; however, the sensitivity was diminished due to the limited transport mechanism of the analyte gases to the sensing surface caused by the membrane. This renders the device's performance can further be optimized by choosing the membrane's different pore sizes or using another approach, in which the incoming gas can be dehumidified before detection.

Another major concern in wearable applications is that the wearable sensors unavoidably suffer from constant stresses under movements. In our work, the device's performance was investigated after multiple bending cycles. **Figure 5.12(a)** illustrates the resistance remained in a similar range within 250 bending cycles and started increasing after 250 -1000 cycles, confirming the devices suffered from a physical degradation due to wear and tear. **Figure 5.12(b)** indicates the device's sensing performance**,** in fact, experienced a gradual decrease after 500 and 1000 bending cycles. However, a profound response was observed even after 1000 cycles of bending, proving the device

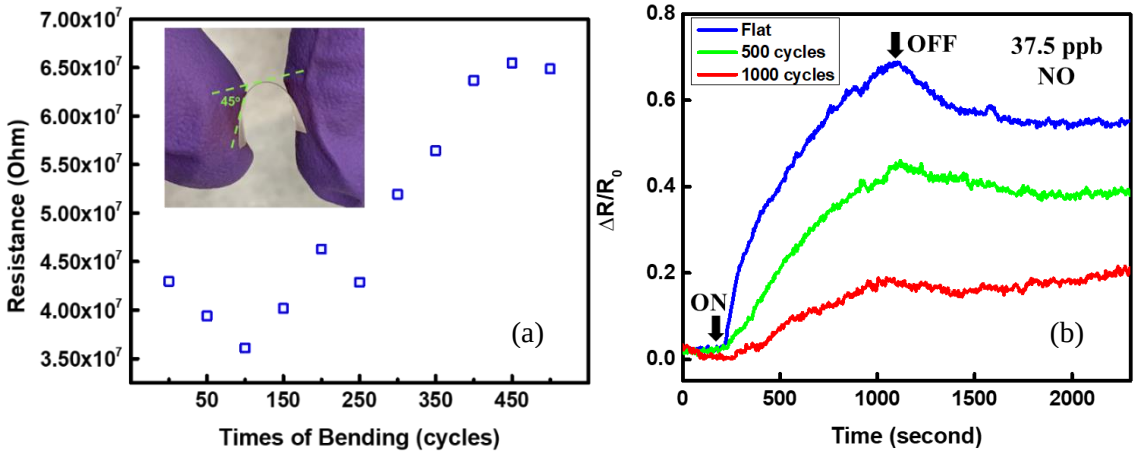

Figure 5.12 Sensing Performance with bending test (a) Change of resistance upon different numbers of bending cycles (b) NO detection of pristine, 500, 1000 cycles.

has excellent potentials for flexible applications. In addition, the same device was tested, after being stored 7 days in ambient condition and pre-treated with an annealing process for 2 hours, showing the similar response as the pristine device (data not shown). This is to confirm that the device has a high stability in ambient conditions.

5.4 Conclusion

In this work, flexible devices using graphene as electrodes and MoS_2 as sensing material were investigated for NO_2 and NO detection. The device showed a good sensitivity at concentration as low as 5 ppb (for NO). The device also demonstrated a good stability in ambient condition and high resistance to wear and tear under physical bending stresses. In addition, the fabrication process is highly compatible with the current nano/microfabrication technology and available for large-scale production. Even though the device cannot completely alleviate the effect of humidity, the issue can be simply addressed by a pre-treatment process of dehumidification. These results confirm that our device has high potentials for on-skin device applications and, especially, for wound monitoring. The sensitivity of the device can be further enhanced by additional functionalization using metal nanoparticles or other bio/chemical molecules on the sensing MoS_2 channel.

5.5 References

(1) Järbrink, K.; Ni, G.; Sönnergren, H.; Schmidtchen, A.; Pang, C.; Bajpai, R.; Car, J. Prevalence and Incidence of Chronic Wounds and Related Complications: A Protocol for a Systematic Review. *Syst Rev* **2016**, *5* (1). https://doi.org/10.1186/s13643-016-0329-y.

(2) Mubeen, S.; Lai, M.; Zhang, T.; Lim, J.-H.; Mulchandani, A.; Deshusses, M. A.; Myung, N. V. Hybrid Tin Oxide-SWNT Nanostructures Based Gas Sensor. *Electrochimica Acta* **2013**, *92*, 484–490. https://doi.org/10.1016/j.electacta.2013.01.029.

(3) Pham, T.; Ramnani, P.; Villarreal, C. C.; Lopez, J.; Das, P.; Lee, I.; Neupane, M. R.; Rheem, Y.; Mulchandani, A. MoS2-Graphene Heterostructures as Efficient Organic Compounds Sensing 2D Materials. *Carbon* **2019**, *142*, 504–512. https://doi.org/10.1016/j.carbon.2018.10.079.

(4) Villarreal, C. C.; Pham, T.; Ramnani, P.; Mulchandani, A. Carbon Allotropes as Sensors for Environmental Monitoring. *Current Opinion in Electrochemistry* **2017**, *3* (1), 106–113. https://doi.org/10.1016/j.coelec.2017.07.004.

(5) Tran, T.-T.; Mulchandani, A. Carbon Nanotubes and Graphene Nano Field-Effect Transistor-Based Biosensors. *TrAC Trends in Analytical Chemistry* **2016**, *79*, 222–232. https://doi.org/10.1016/j.trac.2015.12.002.

(6) Khan, Y.; Ostfeld, A. E.; Lochner, C. M.; Pierre, A.; Arias, A. C. Monitoring of Vital Signs with Flexible and Wearable Medical Devices. *Adv. Mater.* **2016**, *28* (22), 4373–4395. https://doi.org/10.1002/adma.201504366.

(7) Berry, R. B.; Budhiraja, R.; Gottlieb, D. J.; Gozal, D.; Iber, C.; Kapur, V. K.; Marcus, C. L.; Mehra, R.; Parthasarathy, S.; Quan, S. F.; et al. Rules for Scoring Respiratory Events in Sleep: Update of the 2007 AASM Manual for the Scoring of Sleep and Associated Events. *J Clin Sleep Med* **2012**, *8* (5), 597–619. https://doi.org/10.5664/jcsm.2172.

(8) Abraham, W. T.; Adamson, P. B.; Bourge, R. C.; Aaron, M. F.; Costanzo, M. R.; Stevenson, L. W.; Strickland, W.; Neelagaru, S.; Raval, N.; Krueger, S.; et al. Wireless Pulmonary Artery Haemodynamic Monitoring in Chronic Heart Failure: A Randomised Controlled Trial. *The Lancet* **2011**, *377* (9766), 658–666. https://doi.org/10.1016/S0140-6736(11)60101-3.

(9) Roh, E.; Hwang, B.-U.; Kim, D.; Kim, B.-Y.; Lee, N.-E. Stretchable, Transparent, Ultrasensitive, and Patchable Strain Sensor for Human–Machine Interfaces Comprising a Nanohybrid of Carbon Nanotubes and Conductive Elastomers. *ACS Nano* **2015**, *9* (6), 6252–6261. https://doi.org/10.1021/acsnano.5b01613.

(10) Huang, S.; Liu, Y.; Zhao, Y.; Ren, Z.; Guo, C. F. Flexible Electronics: Stretchable Electrodes and Their Future. *Advanced Functional Materials* **2019**, *29* (6), 1805924. https://doi.org/10.1002/adfm.201805924.

(11) Mohan Kumar, G.; Fu, X.; Ilanchezhiyan, P.; Yuldashev, S. U.; Lee, D. J.; Cho, H. D.; Kang, T. W. Highly Sensitive Flexible Photodetectors Based on Self-Assembled Tin Monosulfide

Nanoflakes with Graphene Electrodes. *ACS Applied Materials & Interfaces* **2017**, *9* (37), 32142–32150. https://doi.org/10.1021/acsami.7b09959.

(12) Choi, M.; Park, Y. J.; Sharma, B. K.; Bae, S.-R.; Kim, S. Y.; Ahn, J.-H. Flexible Active-Matrix Organic Light-Emitting Diode Display Enabled by MoS2 Thin-Film Transistor. *SCIENCE ADVANCES* **2018**, 8.

(13) Balandin, A. A. Thermal Properties of Graphene and Nanostructured Carbon Materials. *Nature Materials* **2011**, *10* (8), 569–581. https://doi.org/10.1038/nmat3064.

(14) Balandin, A. A.; Ghosh, S.; Bao, W.; Calizo, I.; Teweldebrhan, D.; Miao, F.; Lau, C. N. Superior Thermal Conductivity of Single-Layer Graphene. *Nano Lett.* **2008**, *8* (3), 902–907. https://doi.org/10.1021/nl0731872.

(15) Mas-Ballesté, R.; Gómez-Navarro, C.; Gómez-Herrero, J.; Zamora, F. 2D Materials: To Graphene and Beyond. *Nanoscale* **2011**, *3* (1), 20–30. https://doi.org/10.1039/C0NR00323A.

(16) Pham, T.; Li, G.; Bekyarova, E.; Itkis, M. E.; Mulchandani, A. MoS_2 -Based Optoelectronic Gas Sensor with Sub-Parts-per-Billion Limit of NO_2 Gas Detection. *ACS Nano* **2019**, *13* (3), 3196–3205. https://doi.org/10.1021/acsnano.8b08778.

(17) Deokar, G.; Vancsó, P.; Arenal, R.; Ravaux, F.; Casanova-Cháfer, J.; Llobet, E.; Makarova, A.; Vyalikh, D.; Struzzi, C.; Lambin, P.; et al. MoS2–Carbon Nanotube Hybrid Material Growth and Gas Sensing. *Advanced Materials Interfaces* **2017**, *4* (24), 1700801. https://doi.org/10.1002/admi.201700801.

(18) Luo, J.; Chen, A. F. Nitric Oxide: A Newly Discovered Function on Wound Healing. *Acta Pharmacologica Sinica* **2005**, *26* (3), 259–264. https://doi.org/10.1111/j.1745-7254.2005.00058.x.

(19) Witte, M. B.; Barbul, A. Role of Nitric Oxide in Wound Repair. *The American Journal of Surgery* **2002**, *183* (4), 406–412. https://doi.org/10.1016/S0002-9610(02)00815-2.

(20) DEC-Kapton-HN-Datasheet.Pdf.

(21) Kumar, R.; Goel, N.; Kumar, M. UV-Activated MoS_2 Based Fast and Reversible NO_2 Sensor at Room Temperature. *ACS Sensors* **2017**, *2* (11), 1744–1752. https://doi.org/10.1021/acssensors.7b00731.

(22) Park, S.; An, S.; Mun, Y.; Lee, C. UV-Enhanced NO_2 Gas Sensing Properties of SnO_2 -Core/ZnO-Shell Nanowires at Room Temperature. *ACS Applied Materials & Interfaces* **2013**, *5* (10), 4285–4292. https://doi.org/10.1021/am400500a.

(23) Fan, S.-W.; Srivastava, A. K.; Dravid, V. P. UV-Activated Room-Temperature Gas Sensing Mechanism of Polycrystalline ZnO. *Applied Physics Letters* **2009**, *95* (14), 142106. https://doi.org/10.1063/1.3243458.

(24) Li, G.; Suja, M.; Chen, M.; Bekyarova, E.; Haddon, R. C.; Liu, J.; Itkis, M. E. Visible-Blind UV Photodetector Based on Single-Walled Carbon Nanotube Thin Film/ZnO Vertical Heterostructures. *ACS Applied Materials & Interfaces* **2017**, *9* (42), 37094–37104. https://doi.org/10.1021/acsami.7b07765.

(25) Wei, P.; Ning, Z.; Ye, S.; Sun, L.; Yang, F.; Wong, K.; Westerdahl, D.; Louie, P. Impact Analysis of Temperature and Humidity Conditions on Electrochemical Sensor Response in Ambient Air Quality Monitoring. *Sensors* **2018**, *18* (2), 59. https://doi.org/10.3390/s18020059.

(26) Gwiżdż, P.; Brudnik, A.; Zakrzewska, K. Temperature Modulated Response of Gas Sensors Array - Humidity Interference. *Procedia Engineering* **2012**, *47*, 1045–1048. https://doi.org/10.1016/j.proeng.2012.09.329.

CHAPTER 6

Conclusions

6.1 Summary

In order to mitigate the issues of low charge mobility and high Schottky barriers in MoS_2 based devices, one of the approaches is to employ a vertical MoS_2/graphene heterostructure, in which graphene is the conductive channel and MoS_2 behaves as a protecting layer. The n-doping effect was observed in PL spectra, field effect transfer characteristics measurement and theoretically investigated, confirming a strong interaction between the two materials. The top MoS_2 layer in the heterostructure behaves as a passive layer on graphene to alleviate the electrical drift and provides a higher sensitivity to toluene, suggesting that it is a novel material with good sensitivity and stability for gas detection.

Another approach to lower the Schottky barrier at MoS_2/contact metal is to employ graphene as the metal contacts. The pristine 2D-2D contact between graphene and MoS_2 and the tunability of graphene's work function result in an increase in the device's current. Red light LED illumination with photon energy matching the direct bandgap of the single layer MoS_2 further induces photocurrent in the sensors and, as a result, enhances the sensors' sensitivity towards NO_2 detection.

CVD grown MoS_2, due to its high hydrophobicity, is susceptible to delamination from its growth substrate. An Al_2O_3 layer grown by ALD proves to prevent the issue and, in turn, stops the degradation of the sensors in aqueous solutions. A significant n-doping effect by the metal oxide layer further promotes the current in the sensor and allows an additional method of detection without aid of an applied gate potential. In addition, the device using the metal oxide-MoS_2 heterostructure shows high sensitivity and selectivity for DNA detection.

Finally, the 2D MoS_2-graphene heterostructure proves high potentials in flexible device applications. The device shows a good sensitivity at concentration as low as 5 ppb (for NO), demonstrates a good stability in ambient, high resistance to wear and tear and available for large-scale production. As a result, this structure can be developed into on-skin/wearable devices for monitoring human physiology.

6.2 Future work

Due to a wide range of 2D materials that can be synthesized via similar CVD methods, heterostructure origami is limitless. A study on other combinations of heterostructures can provide additional understanding about the materials.

Metal nanoparticles and chemical functionalization have been reported to enhance device's sensitivity. The difference between MoS_2's work function and reduction potential of Au ions allows an ambient reducing-agent-free route to synthesize gold nanoparticles. Thus, it is expected that MoS_2 based sensors' sensitivity can be further improved by using a gold nanoparticle decorated MoS_2 sensing channel.

As proven, 2D nanomaterial-based heterostructures have high potentials for flexible devices. On-skin electronics require wireless interfacing and a radio-frequency identification (RFID) circuit can be integrated to the sensing device. The ultimate focus includes fabricating a low-power consumption device that has good flexibility and stability, is compatible with the human body, exhibits high sensitivity and good selectivity.

APPENDIX A

Vertical MoS_2-Graphene Heterostructure: Theoretical Modeling and Spectroscopic Spectra of MoS_2 in the heterostructure

Our calculations are based on first-principles density functional theory (DFT) using the projector augmented wave method and the Perdew-Burke-Ernzerhof (PBE) type generalized gradient approximation [1,2] as implemented in the software package VASP [3]. Spin-orbit coupling (SOC) is included self-consistently in all calculations. Prior to forming heterostructures, single layer lattice properties of the constituent systems (graphene and MoS_2) were calculated using the kinetic energy cut-off of 500 eV for electronic wave functions. A Γ-centered Monkhorst-Pack Brillouin zone (BZ) integration scheme was adopted to integrate over the BZ [4]. To include van-der-Waals (vdW) type interaction in in the Kohn–Sham energies during structure and energy minimizations, the semi-empirical DFT-D2 dispersion correction of Grimme was used [5]. The forces were calculated using the Hellmann-Feynman procedure and geometries were optimized using a conjugated gradient (CG) scheme with a convergence criterion of 0.001 eV $Å^{-1}$ for the atomic forces. The optimized lattice constants for ML-MoS_2 and graphene are a = b = 3.187 Å and a = b = 2.46 Å, respectively, consistent with Ref. (6) and Ref. (7). To compensate the strain between graphene and 1L-MoS_2, we need to create a commensurate graphene/MoS_2 heterostructures. The graphene/MoS_2 heterostructure is created using CellMatch tool[8] by maintaining the interlayer strain below 5%. A Γ-centered Monkhorst-Pack Brillouin zone (BZ) integration scheme was adopted to integrate over the BZ with k-mesh of 8 × 8 × 1. A plane-wave basis cutoff of 550 eV was used. Structures were relaxed until the interatomic forces are below 0.01 eV $Å^{-1}$. A vacuum distance of 20 Å is used to avoid interactions between the periodically repeated slabs. To circumvent the issue of PBE predicted bandgap, we also carried out calculations using the Heyd-Scuseria-Ernzerhof (HSE)

hybrid functional[9]. The HSE calculations incorporate 25% short-range Hartree-Fock exchange and the screening parameter is set to 0.2 $Å^{-1}$.

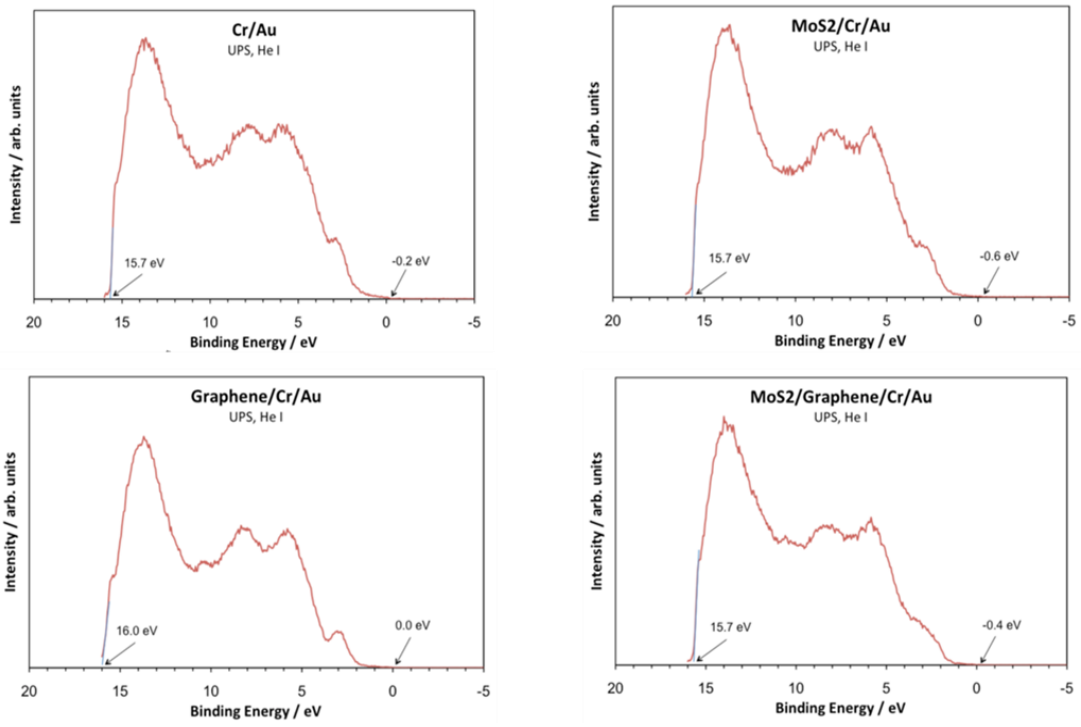

Figure A1. Ultraviolet photoelectron spectroscopic measurement of the substrate (Cr/Au), MoS_2, graphene and MoS_2/graphene heterostructure.

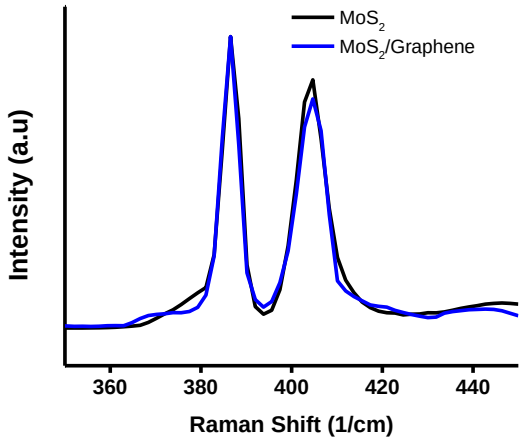

Figure A2. Observed E_{2g} and A_{1g} peaks of single layer MoS_2 and MoS_2/graphene heterostructure from Raman measurement.

References

(1) Perdew, J. P.; Burke, K.; Ernzerhof, M. Generalized Gradient Approximation Made Simple. *Phys. Rev. Lett.* **1996,** *77,* 3865.

(2) Ernzerhof, M.; Scuseria, G. Assessment of the Perdew-Burke-Ernzerhof Exchange-Correlation Functional. *J. Chem. Phys.* **1999**, *110,* 5029.

(3) Kresse, G.; Hafner, J. Ab Initio Molecular Dynamics for Liquid Metals. *Phys. Rev. B.* **1993**, *47*, 558.

(4) Monkhorst, H. J.; Pack, J. D. Special Points for Brillouin-Zone Integrations. *Phys. Rev. B.* **1976**, *13*, 5188.

(5) Grimme, S. Semiempirical GGA-Type Density Functional Constructed with a Long-Range Dispersion Correction. *J. Comput. Chem*. **2006**, *27*, 1787.

(6) Huang, Y. L.; Chen. Y.; Zhang, W.; Quek S. Y.; Chen C. H.; Li, L. J.; Hsu, W. T.; Chang, W. H.; Zheng, Y. J.; Chen, W.; Wee, A. T. Bandgap Tunability at Single-Layer Molybdenum Disulphide Grain Boundaries. *Nature Comm.* **2015**, *6*, 6298.

(7) Pozzo, M.; Alfe, D.; Lacovig, P.; Hofmann, P.; Lizzit, S.; Baraldi, A. Thermal Expansion of Supported and Freestanding Graphene: Lattice Constant versus Interatomic Distance. *Phys. Rev. Lett.* **2011**, *106,* 135501.

(8) Lazic, P. CellMatch: Combining Two Unit Cells into a Common Supercell with Minimal Strain. *Comput. Phys. Comm*. **2015**, 197, 324.

(9) Heyd, J.; Scuseria, G. E.; Ernzerhof, M. Hybrid Functionals Based on a Screened Coulomb Potential. *J. Chem. Phys.* **2003**, 118, 8207.

APPENDIX B

Additional electrical measurement and NO_2 detection using MoS_2 based optoelectronic sensor

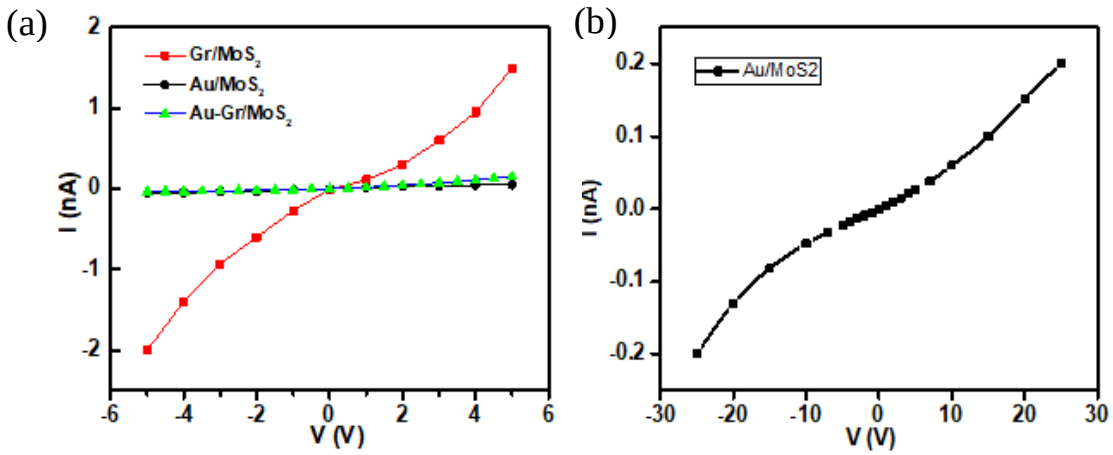

Figure B1. (a) I-V curves in dark for MoS_2 devices with different types of electrodes in the range of low bias voltages below 5 V; (b) I-V curve in dark for the device with Au electrodes in the expanded range of bias voltages up to 25 V showing developing of the non-linearity associated with reverse breakdown of the Au/MoS_2 Schottky diode.

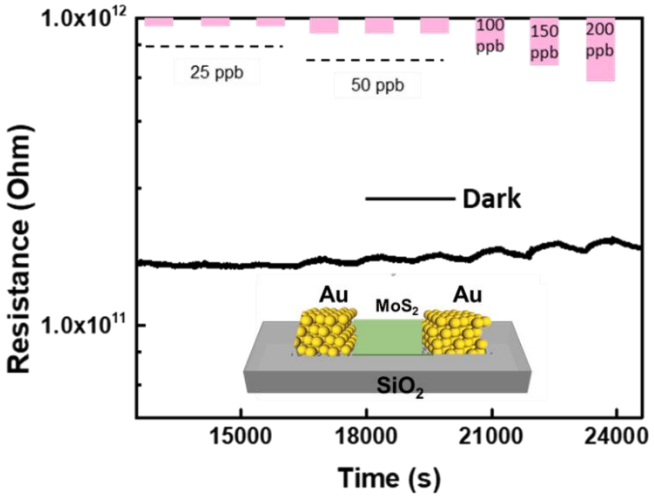

Figure B2. Real-time/dynamic resistance of a single Au-MoS_2-Au sensor to 25 to 200 ppb NO_2 in dark.

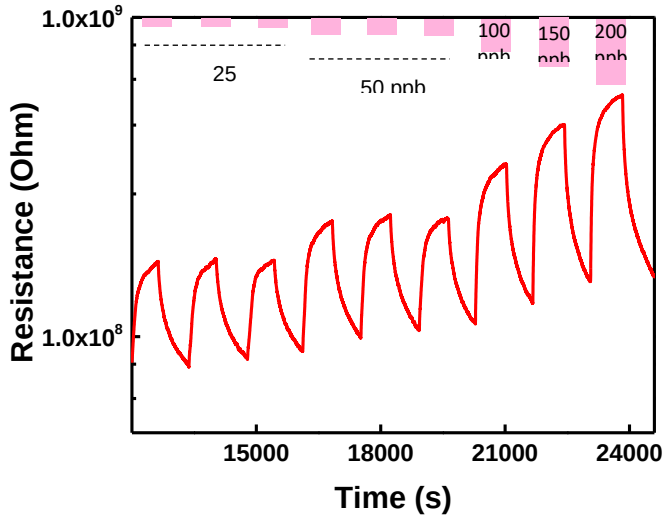

Figure B3. Real-time/dynamic resistance of a single Au-MoS_2-Au sensor to 25 to 200 ppb NO_2 under red LED illumination of incident power of 60.9 nW (light intensity of 60.9 mW/cm^2).

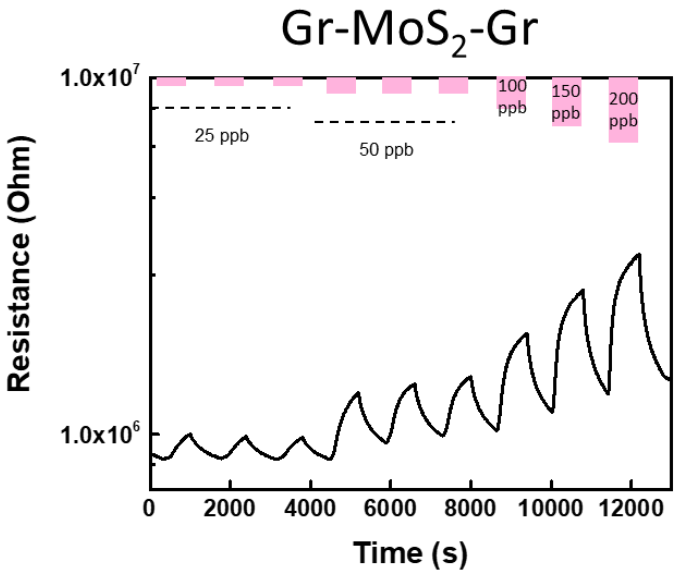

Figure B4. Real-time/dynamic resistance of a single Gr-MoS_2-Gr sensor to 25 to 200 ppb NO_2 under red LED illumination of incident power of 60.9 nW (light intensity of 60.9 mW/cm^2).

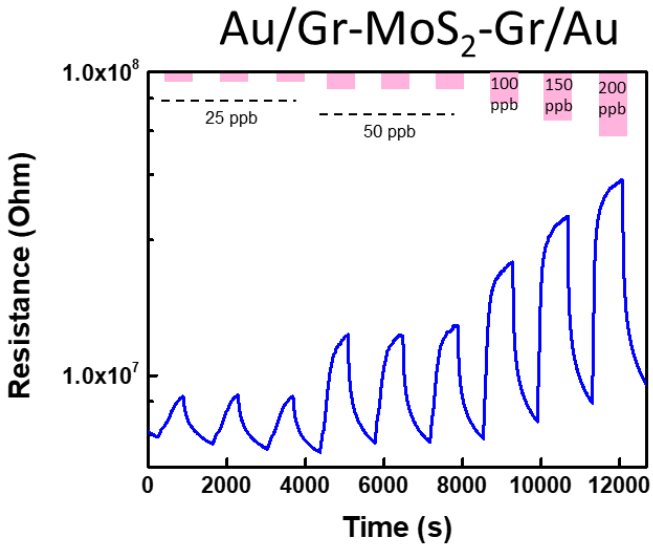

Figure B5. Real-time/dynamic resistance of a single Au/Gr-MoS_2-Gr/Au sensor to 25 to 200 ppb NO_2 under red LED illumination of incident power of 60.9 nW (light intensity of 60.9 mW/cm^2).

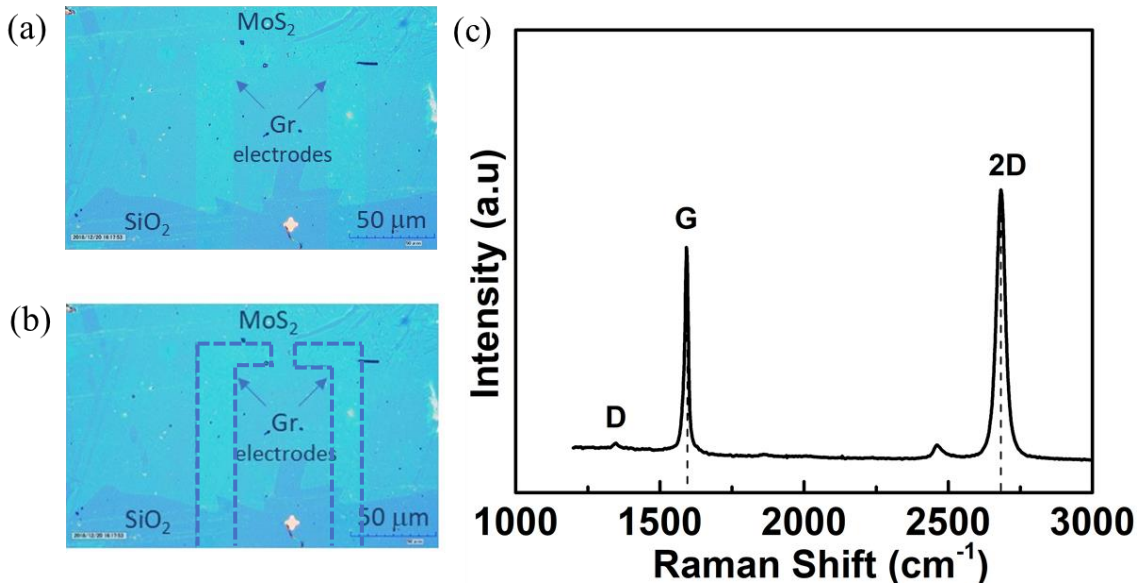

Figure B6. (a) Optical image of MoS_2 device using graphene as electrodes; (b) The same image with dashed lines showing the contours of the patterned graphene electrodes; (c) Raman spectra of graphene.

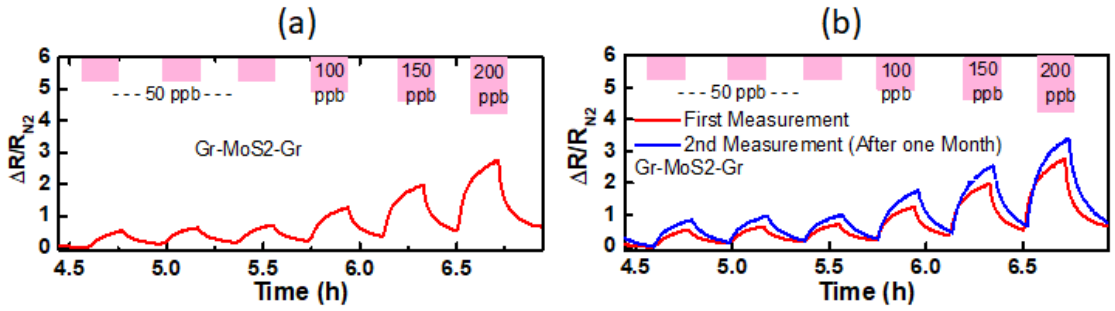

Figure B7. Long term stability of MoS2-based sensor under red LED illumination, exposure to ambient environment, testing and storage: (a) Gr-MoS2-Gr was exposed for 4.5 hours to red LED illumination before NO_2 exposure but showed reproducible resistance modulation during NO_2 on-off cycling during 2.5 hours of testing. (b) The same Gr-MoS2-Gr based sensor maintained high sensitivity to NO2 after one month of testing and storage.

APPENDIX C

Additional spectroscopic measurement, optical image and electrical characterization of MoS_2-metal oxide heterostructure

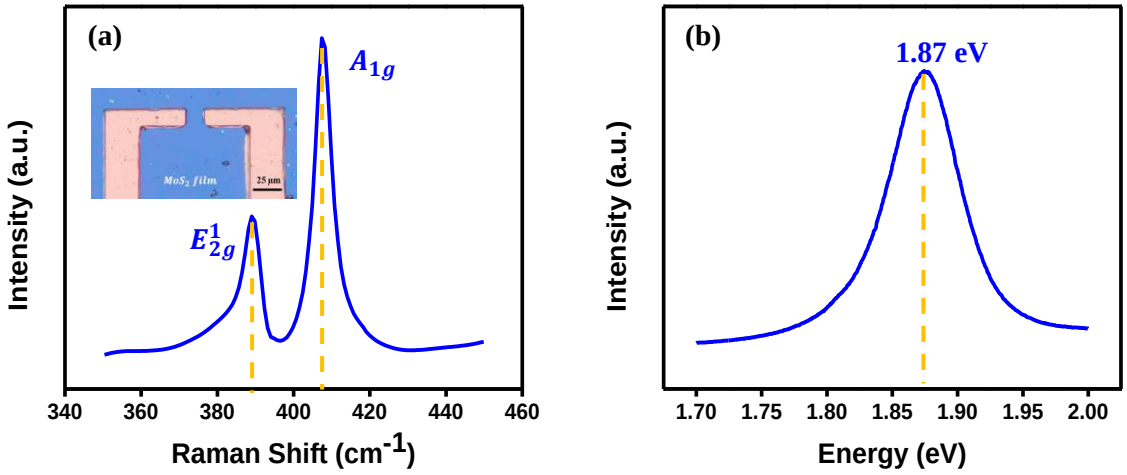

Figure C1. Spectroscopic properties of CVD- MoS_2 (a) Raman Spectrum and optical image of MoS_2 device (inset). (b) Photoluminescence of CVD- MoS_2 showing a direct band gap of 1.87eV.

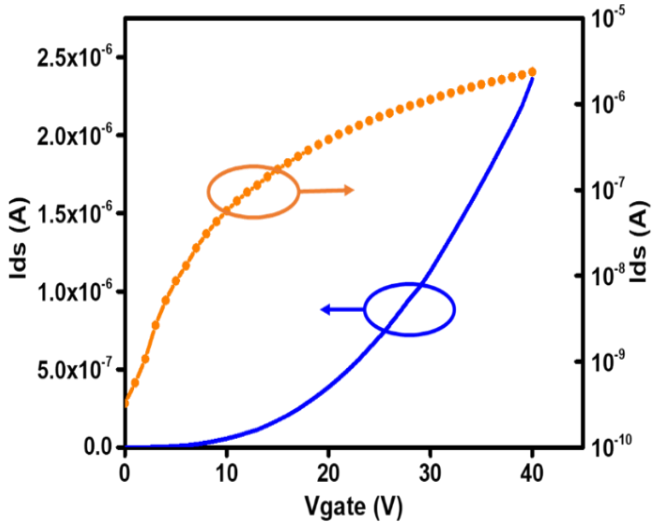

Figure C2. Field Effect Transistor characteristics curve using MoS_2 as the conducting channel (V_{DS} = 5 V).

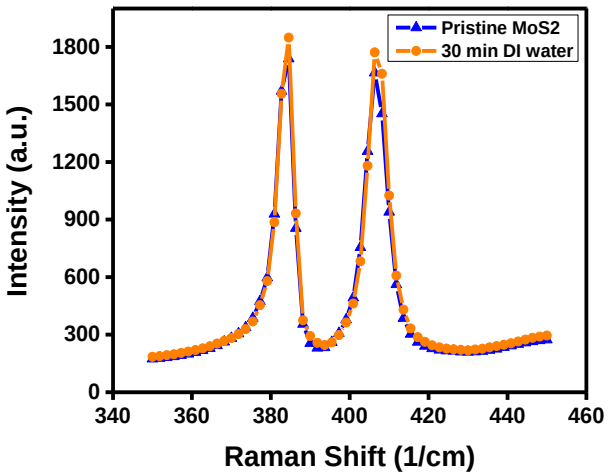

Figure C3. Raman Spectra of MoS_2 before and after 30-minute incubation in DI water.

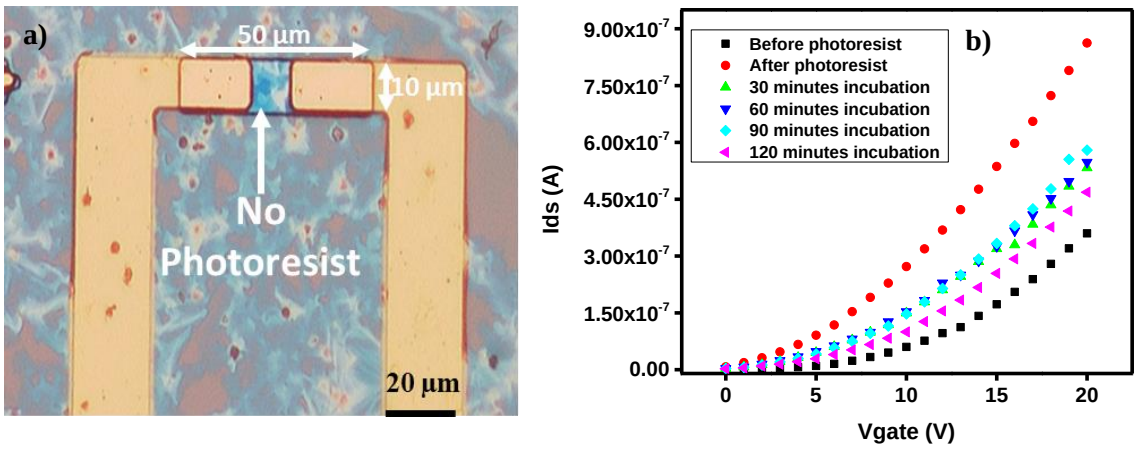

Figure C4. S1813-MoS_2 based device (a) Optical image and (b) Field Effect Transistor characteristics after in DI water (pH=7).

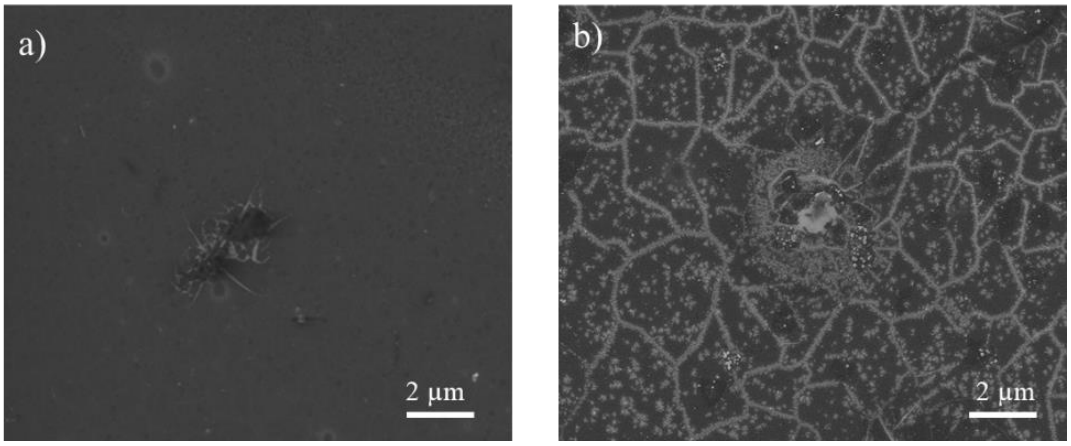

Figure C5. SEM image of same location a) before; b) after 10 mins incubation in 5 mM $AuCl_3$

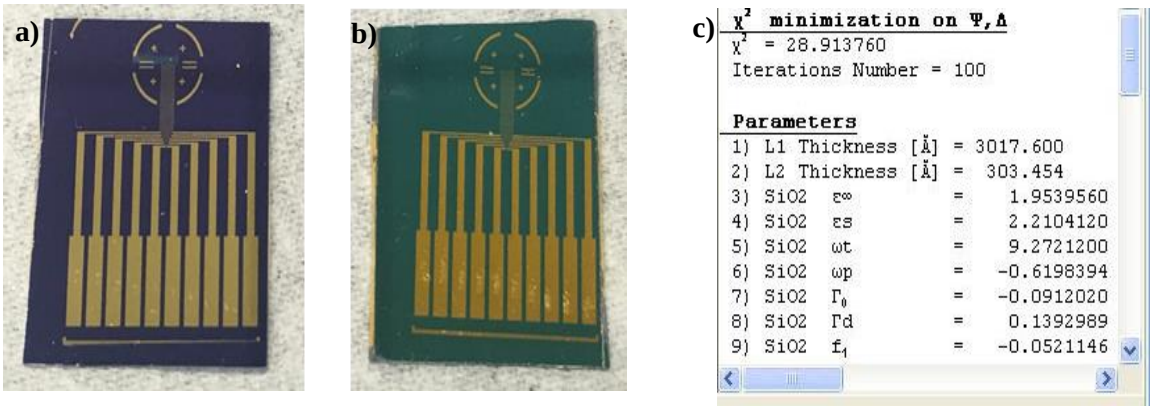

Figure C6. Optical image of the sensor (a) before and (b) after Al_2O_3 deposition (c) L1: SiO_2 and L2: Al_2O_3 thickness measured by ellipsometer.